Studies in Positron and Gamma Ray Production for Future Facilities

Thesis submitted in accordance with the requirements of the Lancaster University for the degree of Doctor in Philosophy by

Ayash Alrashdi

May 19, 2015

Abstract

The next generation of particle colliders after the LHC (Large Hadron Collider) at CERN are likely to be high-precision electron positron colliders such as the ILC (International Linear Collider) or CLIC (Compact Linear Collider). This next generation of colliders will give new scope to explore particle interactions in more detail than in current accelerators. However, producing a sufficient numbers of positrons is a significant challenge. One of the most difficult problems associated with the production of positrons is designing a production target that will survive in an intense photon beam while rotating at high speeds to spread out the energy from the beam. In the first part of this thesis I present a solution to a torque problem affecting the positron production target of high-energy electron-positrons colliders. Typically, the target experiences a braking force due to immersing the wheel inside a strong magnetic field to improve the capture efficiency for positrons. Using OPERA 3D software, a large number of simulations were performed to explore the movement of the target wheel inside the field. I developed a new magnet design which could help to reduce the torque effects. I show that a decrease in the torque parallel to the drive shaft from 500 Nm to 20 Nm is possible in principle, while a torque of 10 Nm perpendicular to the drive shaft is predicted.

Also, the baseline design of the ILC (International Linear Collider) positron source requires the production of an intense flux of gamma rays. In the second part of this thesis I present an investigation of different magnetic field maps and the trajectories of electrons passing through the undulator. I present an investigation of using the spent gamma ray beam of the ILC for additional applications, including nuclear physics. As a result of changing the collimator shape, as well as the parameters of the undulator magnets, I obtain spectra from numerical simulations

using the HUSR/GSR software package. I show that a narrow bandwidth energy spectrum of 5% and photon flux of 10^{13} photon/s is possible in principle.

Acknowledgements

In the first place, I would like to record my gratitude to Dr. Ian Bailey for his supervision, advice, and guidance from the very early stage of this research. I would like to thank him for giving me the opportunity to do my PhD work in the field of accelerator physics. It has been a honor to be one of his PhD student. He did a wonderful job to teach me how good theoretical and experimental physics are done. Ian's professional explanations were there when I needed them to ease unfamiliar materials. Ian's red pen remarks on several draft of this thesis were beneficial. Ian's was more than just a best supervisor, he was a friend and a mentor. Thanks Dr. Ian.

This PhD thesis would not have been possible without the support of many people. Special thanks to all my graduate colleagues in our group for their support and their good wishes. Thanks to the author of HUSR/GSR software Dr. David Newton for giving me the access to use this powerful tool. Thanks to Mike for his help with setting up HUSR/GSR software in the early stage of this work. Thanks to Nathan for your support and your valuable discussion. Thanks to Dr. Nick Grant for his time reading some of this thesis and giving some excellent comments.

Thanks to my wife and my children; it was really difficult time for them for missing me most of the time. It was their sacrifice to assist me to succeed. Thanks to my wife Segiah, for your help in innumerable ways. Many thanks for your help, constant patience, support, and looking after me and my children.

Thanks to my family in Saudi Arabia. Thanks to my father, brothers, and sisters. Thanks for their support and constant encouragement. Thanks for King Abdul-Aziz City for Science and Technology (KACST) for giving me this chance to do my PhD.

Finally, to the remembrance of my mother who passed away 21 years ago. I will never forget you.

To the remembrance of my mother, who passed away in 1994

To my father

To all my family members

To my wife Seigah and my children Ghaida, Ghada, Yasser, and the new coming baby!

Contents

List of Figures

List of Tables

Chapter 1

Introduction

1.1 International Linear Collider (ILC)

If it is built then the future International Linear Collider (ILC) will make a major contribution to particle physics as a 'higgs factory' and search for new physics. The future International Linear Collider (ILC) will have a 200-500 GeV centre of mass energy [1]. The ILC will be working with the Large Hadron Collider LHC [2] (proton-proton collider) at (CERN) in Geneva, Switzerland in a complementary way to explore the deepest puzzles in this world. The planned design for ILC is shown in Fig. 1.1.

As shown in Fig.1.1, there will be two linear accelerators facing each other with a small crossing angle. The ILC will collide electron and positron beams each carrying 10^{14} particles per second with a peak luminosity of $2 \times 10^{34}\text{cm}^{-2}\text{s}^{-1}$. The beams will gain energy from superconducting RF accelerator cavities, which work at a very low temperature of $\sim$ 2 K, before they collide with each other at the centre of the ILC. The RF cavities' nominal accelerating gradient is 31.5 MV/m. For each linac, 15 km of accelerating structures are required to accelerate the particles to 250 GeV. The beams will have a width of 640 nm and a height of 5.7 nm at the collision point [3].

The electron linac contains a helical undulator insertion at the 150 GeV point for positron production as described in more detail is section 1.5. After the electron beam passes through the undulator, it will be accelerated again up to the beam collision energy. For beam collision energies less than 150 GeV the electron beam energy is alternated between 150 GeV for positron production and lower value for collision. Then the electrons will pass through the beam delivery system (BDS), which is a process of collimation and focussing of the beam to the small size need at the interaction point(IP). The positrons from the positron source pass through a transfer line to the start of the the positron linac to be accelerated.

The proposed parameters for the ILC are shown in table 1.1. The ILC should be sensitive to 'new physics' processes from supersymmetry or other extensions to the Standard Model [1].

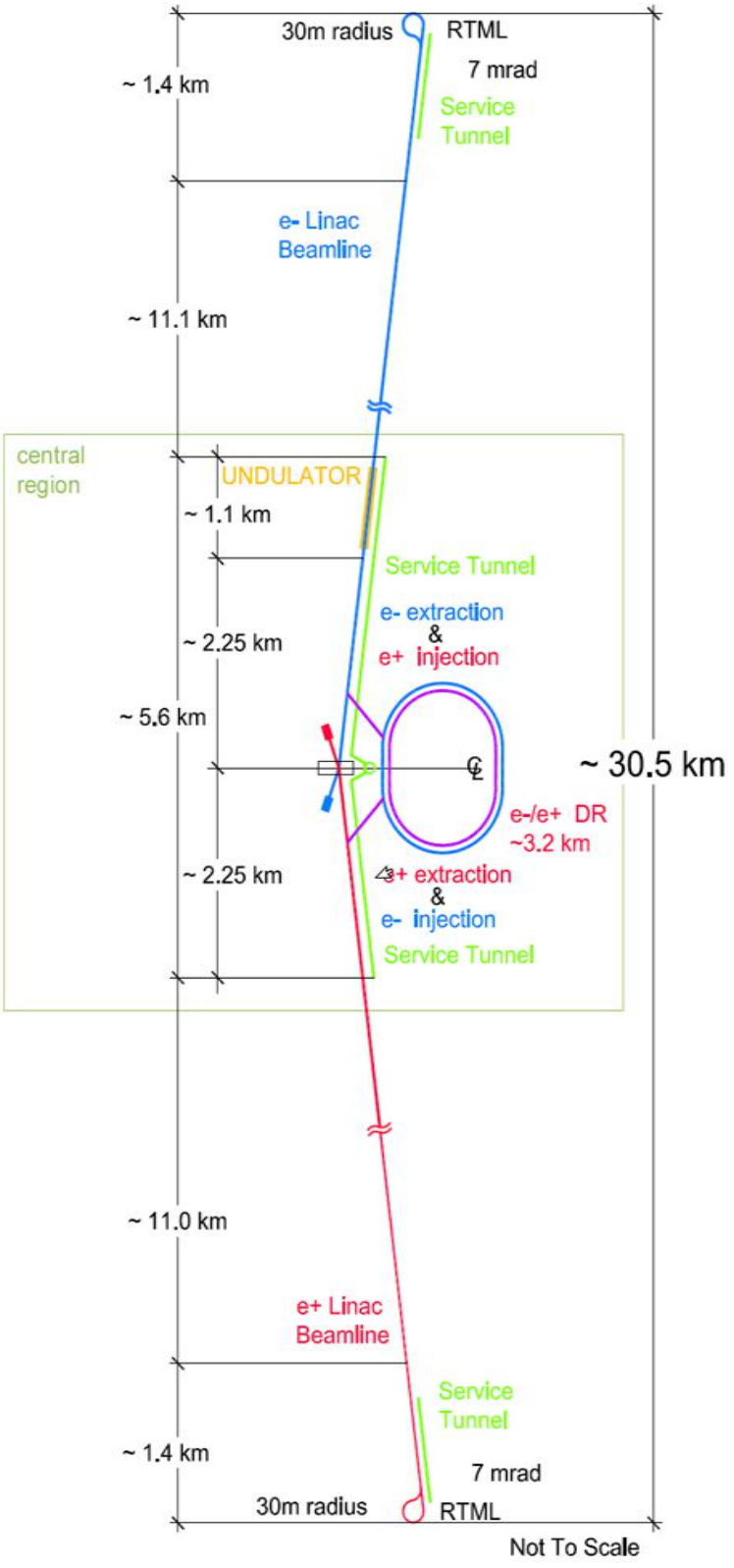

FIGURE 1.1: Planned layout for ILC [1].

TABLE 1.1: ILC proposed parameters [3].

Parameters	Values
Centre-of-mass energy	200 - 500 GeV
Peak luminosity	$2 \times 10^{34}\text{cm}^{-2}\text{s}^{-1}$
Average beam current in pulse	9.0 mA
Pulse rate	5.0 Hz
Pulse length	$\sim$ 1 ms
Number of bunches per pulse	1000 - 5400
Charge per bunch	1.6 - 3.2 nC
Accelerating gradient	31.5 MVm^{-1}
RF pulse length	1.6 ms
Beam power	10.8 MW
Typical beam size at IP ($h \times v$)	640 nm $\times$ 5.7 nm
Total AC Power consumption	230 MW

1.2 Gamma-Ray Sources

1.2.1 Introduction

Dedicated gamma-ray sources play an important role in nuclear physics and low-energy particle physics experiments. Gamma-rays were discovered in 1900 when Paul Villard investigated the radiation emitted from radium [4]. Gamma rays are high-energy photons. Gamma decay from radioisotopes is a natural source of gamma rays which also come from cosmic rays.

Man-made sources of gamma rays are widely used in many applications around the world. The two most common sources will be explained briefly in the following sections with a focus on the gamma-ray source based on undulators; current gamma-ray sources will also be discussed in terms of photon flux and energy bandwidth and I compare them later to the gamma rays which would be produced from the ILC source.

1.2.2 Type of Gamma-Ray Sources

1.2.2.1 Synchrotron Radiation Sources

When charged particles go through a periodically varying magnetic field (undulator) synchrotron radiation is emitted. This type of source is commonly used in x-ray sources and there are several facilities around the world where this technique is used to produce an x-ray beam such as at the Diamond Light Source [5]. However, there has also been a demonstration of high-energy (gamma-ray) photon production in a crystalline undulator [6]. The ILC, will use the first source of gamma-rays produced directly by an undulator.

On the other hand, undulators already play an important role in current gamma-ray sources such as the SPring-8 (Japan) gamma-ray source where they use an undulator to produce x-rays. These x-rays are reflected back by a single crystal and are scattered from an 8 GeV electron beam to produce the gamma rays. This technique is called Backward Compton Scattering (BCS) [7]. Also, an undulator is used in the HIγS facility (USA) where the undulator is used to produce x-rays from a Free Electron Laser (FEL); this is used later in Compton Scattering [8].

1.2.2.2 Compton Scattering Source

Gamma rays can be produced due to the interaction between an electron beam and a laser at a certain angle. The first observation of Compton Scattering was by Arthur H. Compton [9]. In 1963 inverse Compton Scattering was proposed by Milburn [10]. The first experimental demonstration of inverse Compton Scattering was accomplished one year later by O.F. Kulikov [11].

Since that time different Compton scattering sources using either x-rays or gamma-rays have been designed and operated around the world. The most powerful

Compton source up to now is the High Intensity Gamma-ray Source HIγS at Duke University, USA. HIγS has a total photon flux of 3×10^9 photon/s with energy bandwidth ($\Delta E\gamma/E\gamma$) 5% [12].

A new Compton scattering gamma-ray source called Extreme Light Infrastructure - Nuclear Physics (ELI-NP) is being designed by an international collaboration based in Romania. ELI-NP will have a narrow bandwidth $\lesssim 0.5\%$ with a total photon flux of 8.3×10^8 photon/s [13].

1.3 Positron Sources

1.3.1 Introduction

Positrons can be produced by different sources naturally or experimentally. Naturally-occurring positrons are produced in (β^+) decay, for example, the decay of magnesium-23 into sodium-23,

$$^{23}_{12}\mathrm{Mg} \rightarrow {}^{23}_{11}\mathrm{Na} + e^+ + \nu_e. \tag{1.1}$$

Another natural source is cosmic rays, which can produce positrons with very high energy, but the flux is too low to be used in high energy physics experiments [14, 15]. For example, the flux of electrons and positrons with 10 MeV is approximately $30\,\mathrm{m^{-2}s^{-1}sr^{-1}}$ [16].

Experimentally, in 1928 there was an article published by Paul Dirac [17] which suggested that electrons have a positively charged partner. This led to the Bethe-Heitler pair-production theory in which a photon converts to a e^+/e^- pair [18].

The photon must have sufficient energy to produce the mass of the electron and positron which have masses of $0.511\,\mathrm{MeV/c^2}$ each. Therefore, the photon must

have an energy higher than 1.022 MeV/c^2 to produce a e^+/e^- pair. Fig. 1.2 shows the cross sections of a photon interacting in carbon and lead as a function of energy [19]. This interaction takes place in the positron production process which will be described in more detail in section 1.4.

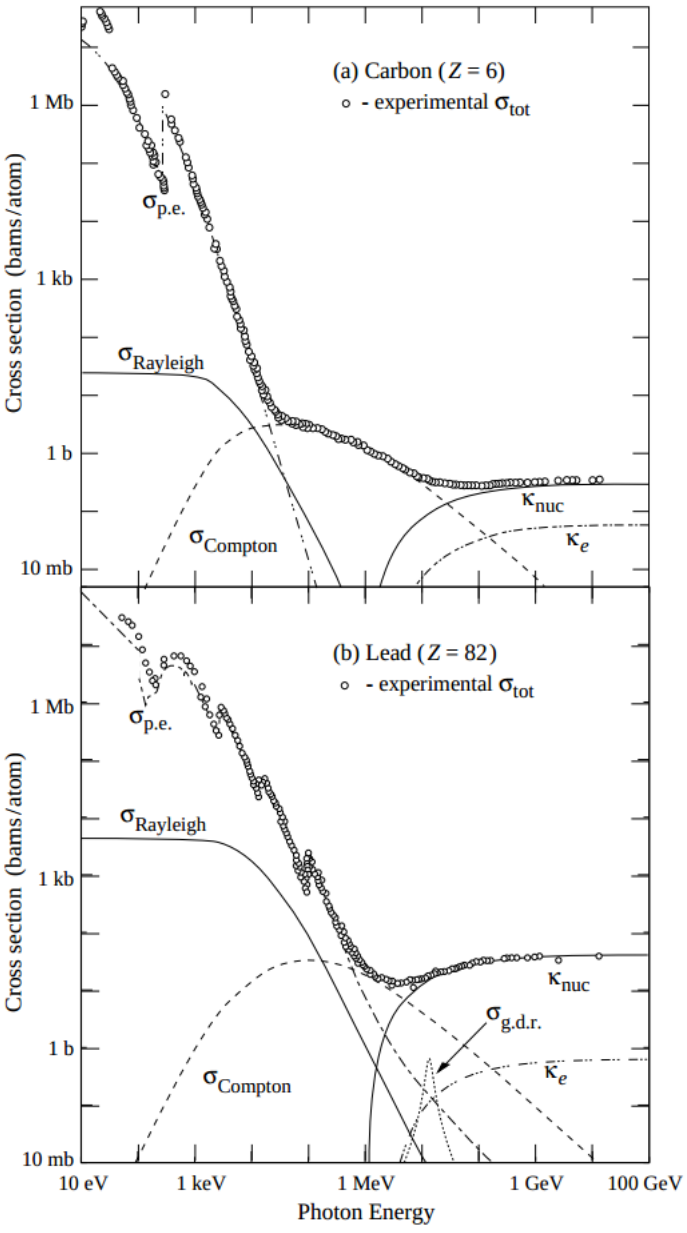

FIGURE 1.2: The total cross sections of photon in carbon and lead as a function of energy. The diagrams have been reproduced from [19].

1.4 Methods for Positron Production

1.4.1 Conventional Method

In these types of sources, an electron beam strikes a large Z target such as tungsten. A bremsstrahlung photon is emitted by the electron. The photon converts to a e^+/e^- pair. Positrons are separated from electrons using a magnetic field. The lifetime of the materials used in the target is limited by the injected amount of energy. In 1998, the target of the Stanford Linear Collider (SLC) failed due to the large amount of energy which caused thermal stresses [20]. However, there has been a recent study which may make this design feasible for the ILC by changing the pulse rate of the electron beam striking on the target and with the addition of an advanced cooling system for the target [21]. However, this method only fulfils the requirement of an unpolarized positron source for the ILC, and more investigations are needed into this method, including experimental work. I have carried out a case study of the torque affecting the target of this method which is described in appendix B.

1.4.2 Laser-Compton sources Method

In this method, a polarized positron is produced from a polarized photon. The polarized photon is produced by the Compton scattering of an electron beam with an energy of 1-3 GeV with a circularly polarized laser beam at a certain angle [22]. Then, this photon interacts with the target to undergo pair-production to produce the positrons. A simple schematic representation of the Compton scattering for the ILC is shown in Fig 1.3 [22].

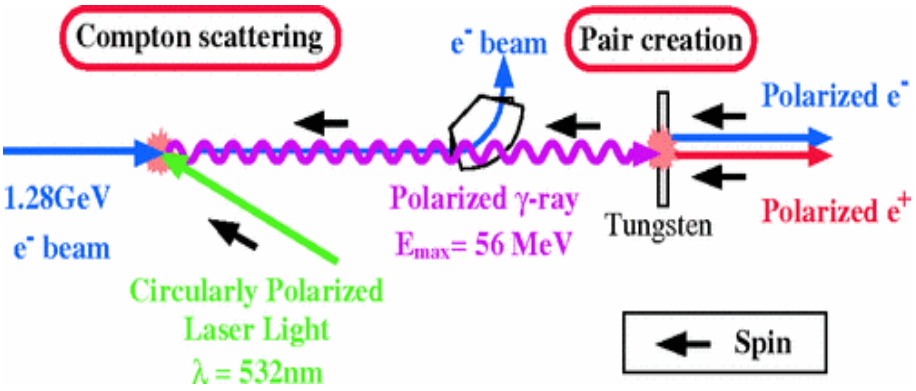

FIGURE 1.3: Compton Scattering source planned design for ILC positron source. This figure has been reproduced from [22].

1.4.3 Undulator Based Source Method

In this method, charged particles e.g electrons with high energy, go through an undulator insertion device to produce high energy photons with high intensity [23]. In order to obtain a polarized photon beam to produce a polarized positron, a helical undulator is used [24]. This type of source was presented and explained in 1977 [25]. The undulator based source was selected and investigated in more detail for the TeV-Energy Super-conducting Linear Accelerator (TESLA) collider project [26, 27]. A simple schematic diagram of this method is shown in Fig. 1.4 [28].

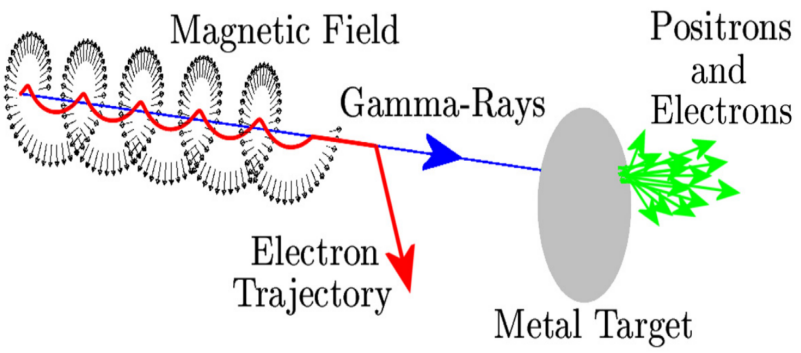

FIGURE 1.4: Layout of the method of producing polarised positrons from high-energy electrons passing through helical undulator. This figure has been reproduced from [28].

A proof of principle experiment Experiment-166 [29] was performed in 2009 at SLAC, where they used a 1 m long helical undulator to produce polarized positrons. An electron beam with an energy of 50 GeV went through the helical undulator, which produced circular polarized photons. Electrons and positrons are produced, when the photons impinge on a metal target. This type of positron source is used to produce polarized positrons and is planned to be used at the ILC [1].

1.5 The International Linear Collider Positron Source

In conventional positron sources, such as the positron source of the Stanford Linear Collider (SLC) at the Stanford Linear Accelerator Centre (SLAC) [30], they used an electron beam striking on a thick high Z target as described in the previous section. In 2005 [31], there was a study comparing the required flux for the ILC and SLC positron sources, which found that the SLC positron flux is less than what is required for the ILC positron source by a factor of 60, and the pulse intensity is less than what is required for the ILC positron source by a factor of

1500 [31]. The required positron flux for the ILC is $\approx 3 \times 10^{14}$ and the produced positron flux at the SLC is $\approx 5 \times 10^{12}$.

The lifetime of the target wheel is limited in conventional positron sources by the heating caused by the large amount of injected energy into the target from the beam. In addition to this beam-induced heating, there is eddy current heating caused by the rotation of the target wheel in the magnetic field of the capture optics [32]. The target wheel needs to be rotated to reduce thermal and radiation damage. The use of this technology in the ILC positron may be possible by changing the beam timing structure as mentioned in section 1.3, but this is potentially expensive and still leads to an unpolarised positron beam. Therefore, it is generally believed that designing a new positron source is required. The planned design for the ILC positron source is shown in Fig. 1.5. The aim of the ILC positron source is to:

- Produce a photon beam with a high power from a helical undulator
- Create the necessary positron bunches in the Ti-6%Al-4%V target
- Guide and accelerate the beam up to 5 GeV
- Inject the beam into the damping ring. Try to minimize beam loss, decrease the energy spread, and spin rotation before injection [33]

In Fig. 1.5, an electron beam with an energy of 150 GeV coming from the main Linac is used in the positron source. This beam is sent through a helical undulator. A helical undulator of 147 m length produces photons with energies of order MeV when an electron beam with energy of 150 GeV passed though it; the average energy of the gamma rays is approximately 10 MeV [3]. These photons hit a rotating titanium target wheel. This produces positrons, electrons, and photons, which go through a magnetic field; this is described as OMD (Optical Matching Device) in Fig. 1.5 to focus the beam. This beam enters the capture rf (rf cavity in a solenoid magnetic field). Later, positrons are accelerated, and detached from

the beam, while the photons and electrons are dumped. Finally, the positrons are injected into the damping ring. A benefit of this design is producing a positron beam with a polarization of 30%, as the ILC specification only needs unpolarized positrons, but polarized beams increase the effective luminosity of the machine. One of the difficult parts in the ILC positron source is the titanium target wheel, which will be described in more detail in Chapters 3 and 4.

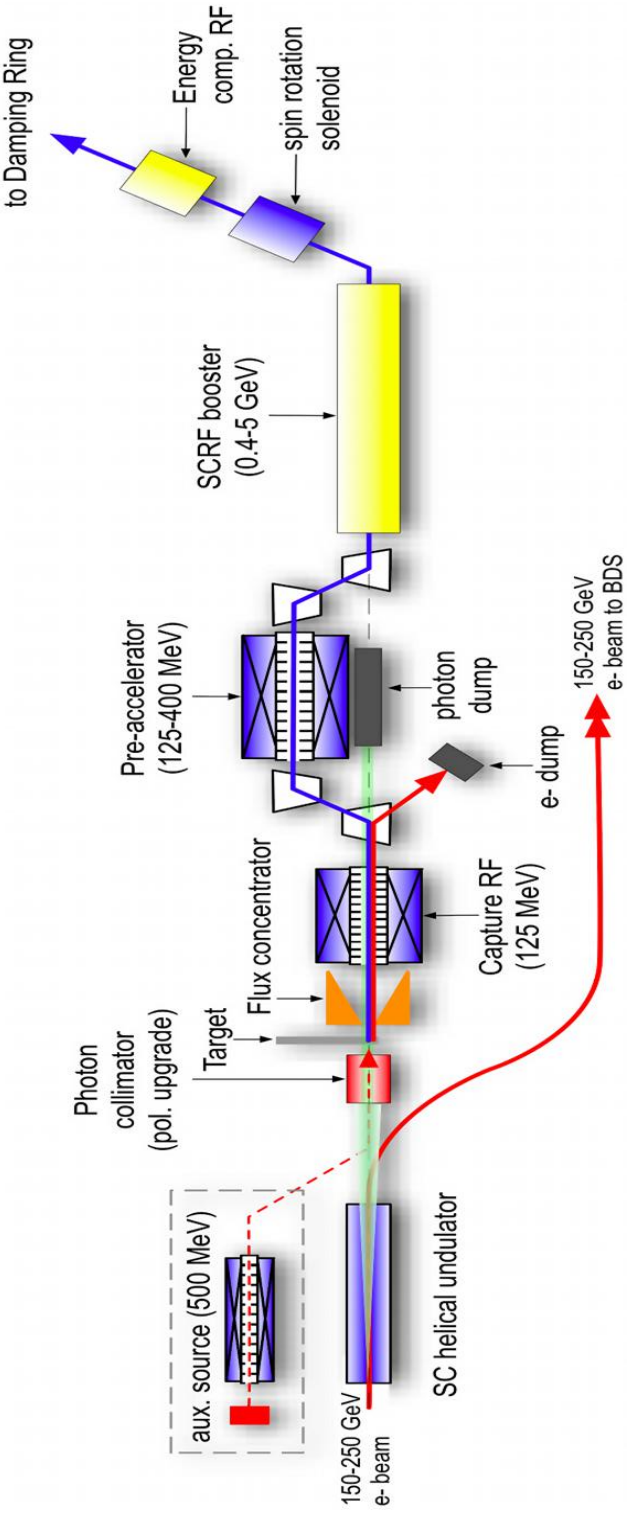

FIGURE 1.5: Baseline design for ILC positron source [3].

1.6 Thesis Outline

There are two main topics in this thesis; in the first part, the eddy current affecting the movement of the ILC positron target wheel is investigated in more detail. In the second part, the possibility of using the ILC gamma ray beam for additional applications is investigated by studying the specification and characteristics of the helical undulator magnetic field.

In chapter 2, the theoretical background of the eddy current brake is described starting from Maxwell's equations, as well as synchrotron radiation from an undulator.

In Chapter 3 experimental validation work is presented which explores the generation of eddy currents in rotating discs and benchmarks the OPERA 3D simulation.

Chapter 4 covers the investigations of a new magnet design for the ILC positron target wheel, which will help to reduce the torque affecting the movement of the current design.

In Chapter 5, realistic simulations of the errors of the magnetic field of the ILC helical undulator are presented. Also, their effects on the electron trajectory inside the helical undulator and the resulting photon energy spectrum are discussed.

Chapter 6 covers the investigations of using the ILC gamma-ray beam for additional applications, including nuclear physics applications. This study involved two different techniques to select useful energy spectra for different applications.

Finally, Chapter 7 gives the conclusions of this work and summarises possible future work.

Chapter 2

Background Theory

In this chapter, I present an introduction to the theoretical background of two main components of the ILC undulator-based positron source. Section 2.1 will describe the physics behind a problem for the current baseline design of the ILC positron source which is eddy current breaking. Section 2.2 will describe the background physics behind the undulator.

2.1 Maxwell's Equations

Maxwell proposed equations can be used for calculating electric and magnetic field distributions. Maxwell's equations are [34]:

$$\vec{\nabla} \cdot \vec{E} = \frac{\rho}{\varepsilon_0} \text{ Gauss's law for electric field} \tag{2.1}$$

$$\vec{\nabla} \cdot \vec{B} = 0 \text{ Gauss's law for magnetic field} \tag{2.2}$$

$$\vec{\nabla} \times \vec{E} = -\frac{\partial \vec{B}}{\partial t} \text{ Faraday's law} \tag{2.3}$$

$$\vec{\nabla} \times \vec{B} = \mu_0 \left(\vec{J} + \varepsilon_0 \frac{\partial \vec{E}}{\partial t} \right) \text{ Ampere's law} \tag{2.4}$$

Where, $\vec{E}$ is the electric field in volts/metre, $\vec{B}$ is the magnetic flux density, ε_0= free space permittivity =$8.85 \times 10^{-12}\,\mathrm{Fm}^{-1}$, and μ_0= free space permeability = $4\pi \times 10^{-7}\,\mathrm{NA}^2$.

2.2 Eddy Current

In my work, I am most interested in Faraday's law which says : "A changing magnetic field induces an electric field" [35]. According to Faraday's Law, if any conducting metal experiences any change of a magnetic field a voltage (emf) will be induced in the conductor. There is no difference if the magnetic field is changing or if the conductor is moving; the voltage will be induced generating 'eddy currents'. Also, there is a connection between Faraday's law and Ampere's law as an induced eddy current loop will itself produce a magnetic field which will oppose the original magnetic field and have effects towards reducing the torque when the conductor is moving at higher speed as observed in [36]. This was confirmed in the simulation which will be discussed in Chapter 4.

2.2.1 Eddy Current and Lorentz force

Here, we will derive the force due to changing the magnetic field. If we have a conductor experiencing a change of a magnetic field, the voltage (emf) induced in the conductor given by:

$$\mathcal{E} = -\frac{\mathrm{d}\Phi_B}{\mathrm{d}t}, \tag{2.5}$$

where

$$\Phi_B = \iint_{\Sigma(t)} \mathrm{d}\vec{A} \cdot \vec{B}(\vec{r}, t).$$

is the flux of the magnetic field through the conductor, $\vec{B}$ is the magnetic flux density, Σ is the total area and $\mathrm{d}\vec{A}$ is the differential area vector of the loop.

Faraday's law showed that, when magnetic flux changes with time, an induced current starts to flow. Now, how did the charge move? The answer is due to the induced (emf) which is defined as the work done per unit charge. We know that work cannot be done by a magnetic field [35], so the work done must be due to the electric field and as the electric field cannot be conservative in this case there is a non-conservative electric field linked with an induced (emf) and given by:

$$\vec{E} = \oint_{\partial\Sigma(t)} \mathrm{d}\ell \cdot \vec{F}/q, \tag{2.6}$$

where

$$\vec{E} = \vec{F}/q$$

is the electric field and the $d\ell$ is a differential length element.

Now, we can compare Equation (2.5) and (2.6) to Equation (2.3).

The force is then given by the Lorentz force law:

$$\vec{F} = q\vec{E}(\vec{r},\ t) + q\vec{v} \times \vec{B}(\vec{r},\ t). \tag{2.7}$$

In Fig. 2.1 and Fig. 2.2 I show examples of the eddy currents produced on the current ILC positron source design due to immersing the target rim in a magnetic field while the target is moving. This is discussed in more details in Chapter 3 and 4.

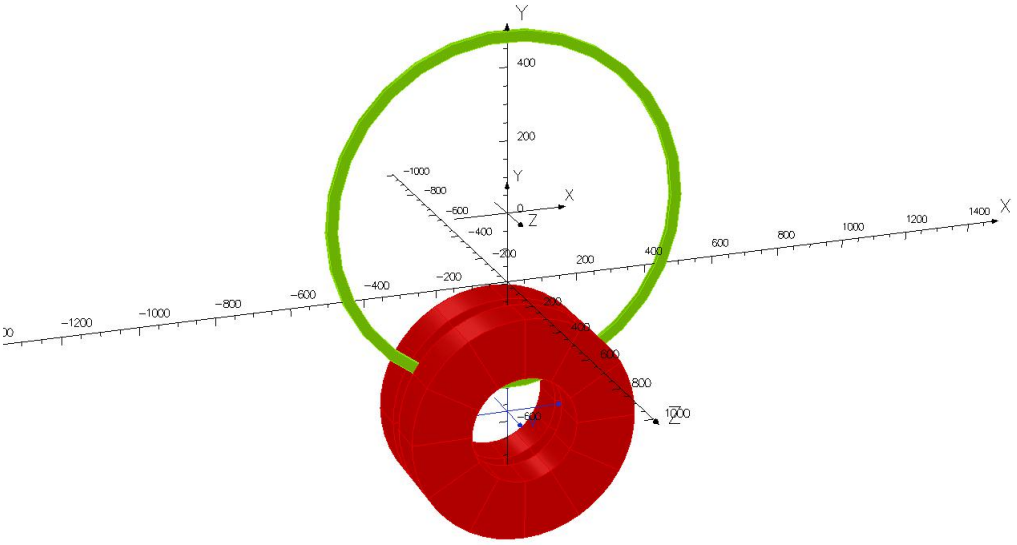

FIGURE 2.1: The OPERA 3D model that I used for investigating the eddy current problem. The solenoid magnet is shown in red, and the target is shown in green.

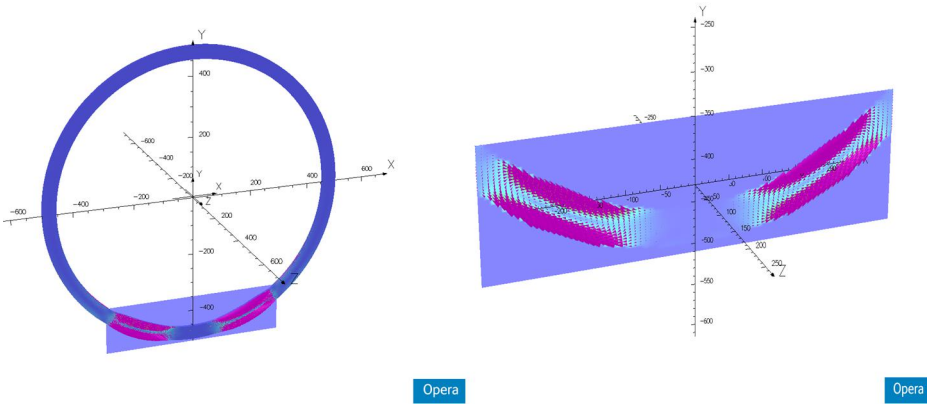

FIGURE 2.2: The OPERA 3D simulation showing eddy current loops (in purple) generated by movement of the target wheel (in blue) inside a constant solenoidal magnetic field.

In the case of the eddy current brake the force is provided by the Lorentz force which supplies a torque. The torque for a rotating solid disc experiencing a magnetic field parallel to the angular velocity vector has been derived in the literature and is given by [37, 36]:

$$\tau = \omega\gamma\Phi^2 D, \tag{2.8}$$

where ω is the angular speed, γ is conductivity, Φ is the magnetic field total flux, and D describes the affected area of the disc. A full treatment of this derivation can be found in [36].

2.3 Undulator

The undulator is one of the main parts of the current design of the ILC positron source. An undulator by definition produces a magnetic field which varies periodically. There are different types of undulator such as a planar undulator or helical undulator. In a planar undulator the magnetic field is acting perpendicular to the direction of the particle beam and forces the beam to oscillate in the plane perpendicular to the magnetic field, which then radiates synchrotron radiation. In a helical undulator there is a rotating dipole magnetic field. The strength of the magnetic field is fixed. The motion of particles passing through the undulator is also helical. The synchrotron radiation emitted is circularly polarised.

In this section, we will describe the radiation from the undulator, especially from helical undulators. The physics behind classical electromagnetism and synchrotron radiation can be found in [34, 38]. Full derivations of undulator synchrotron radiation can be found in [23, 39, 40].

2.3.1 Synchrotron Radiation

From basic laws of classic electrodynamics, when relativistic charged particles undergo acceleration they will emit electromagnetic radiation [34, 38]. Also, when

the path of a relativistic charged particle is bent in a magnetic field synchrotron radiation will be produced.

Charged particles lose power due to synchrotron radiation and this varies as:

$$P \propto \frac{1}{\rho^2 m_0^4}. \tag{2.9}$$

Here, m_0 the particle's rest mass, and ρ is the radius of the particle's trajectory.

Let's consider a relativistic charged particle passing through an undulator with period λ_u. In the case of the co-moving frame, the electron will see the magnet period as λ_u/γ because of Lorentz contraction where γ is the relativistic Lorentz factor given by:

$$\gamma = \frac{E}{E_0}, \tag{2.10}$$

$$\beta = \sqrt{1 - \frac{1}{\gamma^2}}, \qquad \beta = v/c \tag{2.11}$$

here, c is the speed of light, v is the speed of the electron, β is the electron's relative velocity, E is the electron energy, and E_0 is the electron rest energy.

The Doppler shift effect will change the frequency of light seen by an observer at an angle θ to the beam direction to:

$$f = \gamma f^{'} \left(1 + \beta \cos\theta^{'}\right). \tag{2.12}$$

Here the observer is seeing the radiation at frequency f and $f^{'}$ is the frequency emitted by the source. Converting f to wavelength λ, we have:

$$\lambda = \frac{\lambda^{'}}{\gamma\,(1+\beta)} \approx \frac{\lambda^{'}}{2\gamma}. \tag{2.13}$$

The observed wavelength of radiation in the rest frame of the undulator is $\frac{\lambda^{'}}{2\gamma}$. Energy of a few GeV is achievable nowadays, therefore, the relativistic factor γ for electrons will reach a few thousands. For example, the wavelength of a few nanometers can be achieved if an undulator with a period of 0.1 m was used. Another feature of synchrotron radiation is that when γ is of the order of few thousands, the radiation will be emitted into a very narrow cone. When undulator is used, additional narrowing of the cone will be added by a factor $\sqrt{N}$, where N is the undulator's period numbers and this is due to interference effects. This implies that intense radiation with very short wavelength (few nanometers) can be produced when an undulator is used in high energy accelerators.

2.3.2 Electric and Magnetic Fields Calculations

The Lienard-Wiechert potentials ϕ and $\vec{A}$ for moving charges are: given by the Lienard-Wiechert potentials:

$$\phi\,(t) = \frac{q}{4\pi\varepsilon_0}\frac{1}{r\left(1-\vec{\beta}\cdot\vec{n}\right)}, \tag{2.14}$$

$$\vec{A}\,(t) = \frac{\mu_0 c q}{4\pi}\frac{\vec{\beta}}{r\left(1-\vec{\beta}\cdot\vec{n}\right)}. \tag{2.15}$$

Where:

q is the particle's charge

r is the distance between the observation point and particle's position

$\vec{n}$ is the unit vector between the observation point and particle's position

$\vec{\beta}$ is the particle's velocity: $\vec{\beta}\,(t') = \frac{R(t')}{c}$

t' is the retarded time where: $t = t' + \frac{r(t')}{c}$

To obtain the correct values of the potentials at time t, we need to evaluate the particle's velocity at a retarded time t'. The electromagnetic potentials will increase when a particle is traveling straight towards an observer, and is reduced when the particle is traveling away from an observer.

Now, from Maxwell's equations (2.2) and (2.3) we have:

$$\vec{B} = \nabla \times \vec{A}, \tag{2.16}$$

$$\vec{E} = -\nabla\phi - \frac{\partial \vec{A}}{\partial t}. \tag{2.17}$$

where equations (2.16) and (2.17) represent the electric and magnetic fields in terms of the potentials.

The derivations required to determine the electric field and magnetic field for a particle moving along an arbitrary trajectory require manipulation of the formula and standard algebra steps which can be found in [23, 39, 40]. The electric field result is:

$$\vec{E} = \frac{q}{4\pi\varepsilon_0}\left[\frac{(1-\beta^2)\left(\vec{n}-\vec{\beta}\right)}{r^2\left(1-\vec{n}\cdot\vec{\beta}\right)^3} + \frac{\vec{n}\times\left(\left(\vec{n}-\vec{\beta}\right)\times\dot{\vec{\beta}}\right)}{cr\left(1-\vec{n}\cdot\vec{\beta}\right)^3}\right], \tag{2.18}$$

and the magnetic field result is:

$$\vec{B} = \frac{1}{c}\vec{n}\times\vec{E}. \tag{2.19}$$

In Equation (2.18), in the case of no acceleration the second term will be zero, and the contribution will be from the first term only. This is called the velocity field and varies with the distance from the source as r^{-2}. The second term is called the far field and varies with the distance from the source as r^{-1}. In the case of accelerating particles, far from the particles, the second term will dominate over the first term.

2.3.2.1 Poynting Vector

The rate of energy transferred per unit area by an electromagnetic field travelling through space is given by the Poynting vector $\vec{S}$:

$$\vec{S} = \varepsilon_0 c^2 \left(\vec{E} \times \vec{B}\right). \tag{2.20}$$

Now, by using (2.19), we can express the Poynting vector in term of the electric field:

$$\vec{S} = \frac{\vec{E} \times \left(\vec{n} \times \vec{E}\right)}{\mu_0 c}, \tag{2.21}$$

or

$$\vec{S} = \frac{1}{\mu_0 c}\left(\vec{E}^2\vec{n} - \left(\vec{E} \cdot \vec{n}\right)\vec{E}\right). \tag{2.22}$$

As described earlier, in Equation (2.18), in the case of accelerating particles, far from the particles, the second term will dominate over the first term. The far-field is:

$$\vec{E} = \frac{q}{4\pi\varepsilon_0}\left[\frac{\vec{n}\times\left(\left(\vec{n}-\vec{\beta}\right)\times\dot{\vec{\beta}}\right)}{cr\left(1-\vec{n}\cdot\vec{\beta}\right)^3}\right]. \tag{2.23}$$

By considering the far-field, we can rewrite the Poynting vector as:

$$\vec{S}(t) = \frac{1}{\mu_0 c}\left|\vec{E}(t)\right|^2\vec{n}. \tag{2.24}$$

because $\vec{E}$ is always perpendicular to $\vec{n}$ for the acceleration field:

$$E \propto \vec{n}\times\left[\left(\vec{n}-\vec{\beta}\right)\times\dot{\vec{\beta}}\right] \tag{2.25}$$

and therefore $\vec{E}\cdot\vec{n} = 0$.

2.3.2.2 Radiated Energy Spectrum

The Poynting vector for the power flux is given by:

$$S = \frac{1}{r^2}\frac{d^2U}{d\Omega dt}. \tag{2.26}$$

Using Parseval's theorem [41] to solve for energy U radiated into unit solid angle:

$$\frac{d^2U}{d\Omega} = r^2\int_{-\infty}^{\infty} S dt = \frac{r^2}{\mu_0 c}\int_{-\infty}^{\infty}|E(t)|^2 dt = \frac{r^2}{\mu_0 c}\int_{-\infty}^{\infty}|E(\omega)|^2 d\omega. \tag{2.27}$$

With respect to ω, we can differentiate (2.27) to find the angular spectral energy distribution:

$$\frac{d^2U}{d\Omega d\omega} = \frac{2r^2}{\mu_0 c}|E(\omega)|^2. \tag{2.28}$$

The factor of two comes from only considering positive frequencies.

The spectrum (frequency spectrum) of radiation can be calculated from the Fourier transform of the electric field in the time domain. The frequency spectrum of the $\vec{E(t)}$ is therefore given by:

$$\tilde{E}(\omega) = \frac{1}{\sqrt{2\pi}} \int_{-\infty}^{\infty} \vec{E}(t)\, e^{i\omega t} dt. \tag{2.29}$$

In order to find the Fourier transform of the electric field we substitute Equation (2.23) into Equation (2.29) remembering that the integration must be evaluated over dt' as the fields are produced from the charge density at retarded time we get:

$$\tilde{E}(\omega) = \frac{q}{4\pi\sqrt{2\pi\varepsilon_0}} \int_{-\infty}^{\infty} \left[\frac{\vec{n} \times \left(\left(\vec{n} - \vec{\beta} \right) \times \dot{\vec{\beta}} \right)}{\left(1 - \vec{n} \cdot \vec{\beta} \right)^3} e^{i\omega\left(t' + \frac{r}{c}\right)} \left(1 - \vec{n} \cdot \vec{\beta} \right) dt' \right]. \tag{2.30}$$

Supposing that the observer is far enough from the source, we can work in the radiation region. By integrating Equation (2.30) by parts we get:

$$\tilde{E}(\omega) = \frac{qi\omega}{4\pi c r\sqrt{2\pi\varepsilon_0}} \int_{-\infty}^{\infty} \left(\vec{n} \times \left(\vec{n} \times \vec{\beta} \right) \right) e^{i\omega\left(t' + \frac{r}{c}\right)} dt'. \tag{2.31}$$

To find the energy radiated per unit angular frequency per unit solid angle, we substitute Equation (2.31) into Equation (2.28) to get:

$$\frac{d^2U}{d\Omega d\omega} = \frac{\omega^2 q^2}{16\pi^3 c\varepsilon_0} \left| \int_{-\infty}^{\infty} \left(\vec{n} \times \left(\vec{n} \times \vec{\beta} \right) \right) e^{i\omega\left(t' + \frac{r}{c}\right)} dt' \right|^2. \tag{2.32}$$

2.3.3 Motion of electron in a helical Undulator

An electron is forced to oscillate and radiate if it passes through an undulator (which is a magnetic field varying spatially periodically). The equation of force for an electron is:

$$\frac{d\vec{p}}{dt} = -q\left(\vec{E} + \vec{v} \times \vec{B}\right), \tag{2.33}$$

where $\vec{p} = \gamma m\vec{v}$ is the momentum, γ is the relativistic factor, m is the mass of the particle, and v is the velocity of the particle. Now, the radiated electric fields are approximately weak so:

$$\frac{d\vec{p}}{dt} = -q\left(\vec{v} \times \vec{B}\right). \tag{2.34}$$

In the following we consider the magnetic field in the planes transverse to the electron's initial velocity which I take to be z which vary sinusoidally. The magnetic field in the z direction is zero, and we can define the magnetic field in the x and y planes as:

$$B_x = B_0 \cos\left(\frac{2\pi z}{\lambda_u}\right), \tag{2.35}$$

$$B_y = B_0 \sin\left(\frac{2\pi z}{\lambda_u}\right). \tag{2.36}$$

Now, for the first order $v \simeq v_z$, the Equation (2.34) for the x-direction's motion becomes:

$$m\gamma\frac{dv_x}{dt} = qv_z B_y, \tag{2.37}$$

$$m\gamma\frac{dv_x}{dt} = q\frac{dz}{dt}B_0\cos\left(\frac{2\pi z}{\lambda_u}\right), \tag{2.38}$$

$$m\gamma dv_x = qdzB_0\cos\left(\frac{2\pi z}{\lambda_u}\right). \tag{2.39}$$

Integrating both side with respect to $dz = \frac{\lambda_u}{2\pi}d(\frac{2\pi z}{\lambda_u})$:

$$m\gamma v_x = qB_0\frac{\lambda_u}{2\pi}\int\cos\left(\frac{2\pi z}{\lambda_u}\right)d\left(\frac{2\pi z}{\lambda_u}\right). \tag{2.40}$$

Therefore, the velocity of the particle is:

$$v_x = \frac{qB_0\lambda_u}{2\pi m\gamma}\sin\left(\frac{2\pi z}{\lambda_u}\right), \tag{2.41}$$

$$v_x = \frac{Kc}{\gamma}\sin\left(\frac{2\pi z}{\lambda_u}\right). \tag{2.42}$$

where K is the undulator deflection parameter and given by:

$$K = \frac{qB_0\lambda_u}{2\pi mc} = 0.9337B_0\,(T)\,\lambda_u\,(\text{cm})\,. \tag{2.43}$$

Now, to find the particle's co-coordinate we integrate Equation (2.42):

$$x = -\frac{Kc}{\gamma}\frac{\lambda_u}{2\pi}\cos\left(\frac{2\pi z}{\lambda_u}\right). \tag{2.44}$$

The velocity and coordinate of y can be derived in a similar way and the results will be:

$$v_y = -\frac{Kc}{\gamma}\sin\left(\frac{2\pi z}{\lambda_u}\right), \tag{2.45}$$

$$y = \frac{Kc}{\gamma}\frac{\lambda_u}{2\pi}\cos\left(\frac{2\pi z}{\lambda_u}\right). \tag{2.46}$$

Now, the deflection angle θ is given by:

$$\theta_x = \frac{v_x}{v_z} = \frac{v_x}{c} = \frac{K}{\gamma}\sin\left(\frac{2\pi z}{\lambda_u}\right), \tag{2.47}$$

$$\theta_y = \frac{v_y}{v_z} = \frac{v_y}{c} = -\frac{K}{\gamma}\sin\left(\frac{2\pi z}{\lambda_u}\right). \tag{2.48}$$

The motion of the electron inside a helical undulator has been derived. In the next section we combine the results from last two sections to calculate the radiation emitted by an electron travelling through a helical undulator.

2.3.4 Radiation of the Helical Undulator

Using Equation (2.32) we can calculate the distribution of spectral energy of synchrotron radiation from a given particle's trajectory. In this case we are interested in the helical undulator where the trajectory of the particles is a helix. The integration of Equation (2.32) requires more steps which have been performed in the literature [42]. The result for the helical undulator is:

$$\frac{d^2U}{d\Omega d\omega} = \frac{\omega^2 q^2 K^2}{4\pi^3 \varepsilon_0 c \omega_0^2 \gamma^2}\sum_{n=1}^{\infty}\left[J_n'^{\,2}(x) + \left(\frac{\gamma\theta}{K} - \frac{n}{x}\right)^2 J_n^2(x)\right]\frac{\sin^2\left[N\pi\left(\frac{\omega}{\omega_1} - n\right)\right]}{\left(\frac{\omega}{\omega_1} - n\right)^2}. \tag{2.49}$$

Where θ is the angle between the axis of the undulator and the observation point, γ is the relativistic factor, and N is the number of periods in the undulator. The other terms in the expression are:

$$K = \frac{\lambda_u q B}{2\pi m c^2}, \tag{2.50}$$

$$x = \frac{K\theta}{\gamma}\frac{\omega}{\omega_0}, \tag{2.51}$$

$$\omega_0 = \frac{2\pi\beta^* c}{\lambda_u}, \tag{2.52}$$

$$\omega_1 = \frac{\omega_0}{1-\beta^*\cos\theta}. \tag{2.53}$$

Here λ_u is the period of the undulator, B is the strength of the field, β^* is the particle's average velocity in the z direction divided by the speed of light and is given by [42]:

$$\beta^* = \beta\left[1-\left(\frac{\lambda_u}{2\pi\rho}\right)^2\right]^{\frac{1}{2}} \tag{2.54}$$

$$= \beta\left[1-\left(\frac{K}{\gamma}\right)^2\right]^{\frac{1}{2}}. \tag{2.55}$$

Here, ρ is the radius of the particle's helical motion inside the undulator.

An example of the ideal energy spectrum from the ILC helical undulator with 150 GeV electron beam and K=$93.36B_0\lambda_u$ is shown in Fig. 2.3.

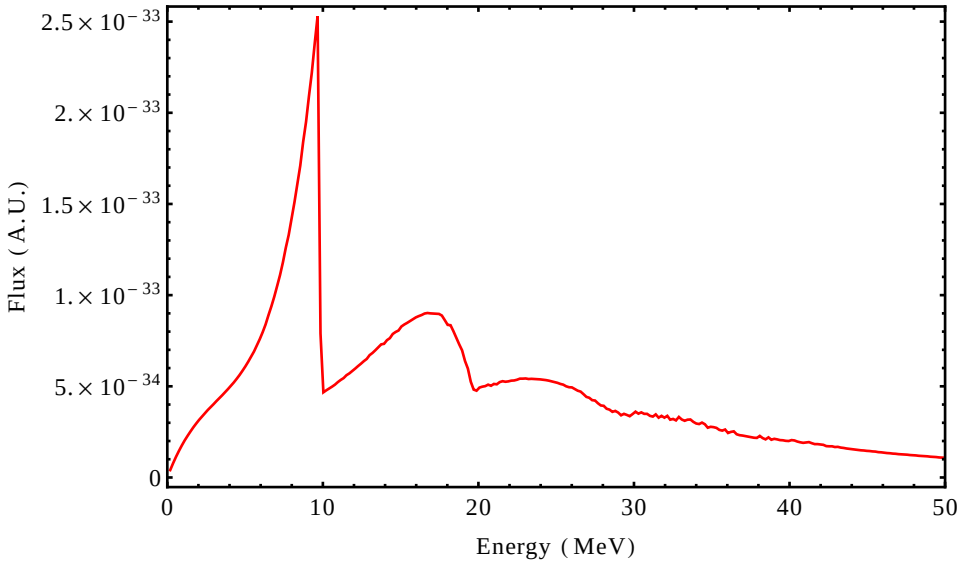

FIGURE 2.3: Calculated energy spectrum from tracking a single electron through an ideal helical undulator with N=155. The spectrum has been simulated using a 150 GeV electron beam and magnetic field strength of 0.88 T.

Equation (2.49) is the key result for the helical undulator which will be discussed in more detail in Chapter 5.

Chapter 3

Eddy Current Experiment

3.1 Introduction

In this chapter, we introduce a simple, low-cost experimental setup that can be used to study and demonstrate a principle to minimise eddy current braking, as well as validating the OPERA 3D [43] software, which is a finite element electromagnetic simulation. In this experiment I considered the motion of a conducting disc inside a magnetic field. I studied the effects of the magnetic field on the movement of the disc as a function of different physical parameters. The disc was made from aluminium.

3.1.1 Equipment

Fig. 3.1 is a photograph of the experiment setup. A list of all necessary elements follows:

- A (280 ± 1) mm diameter, (6 ± 1) mm thick, and (1.0391 ± 0.1) kg disc made of aluminium to be attached to the motor axis shown in Fig. 3.1;

- 8 permanent (NdFeB) magnets with strength of (0.20±0.01)T as shown in Fig. 3.1;
- Magnet support structures made from strong plastic ×2 as shown in Fig. 3.2;
- 5 V motor. Its angular speed is 1400 rpm at 5 V when unloaded;
- Variable 0−5 V dc power source for the motor;
- An optical tachometer (arduino-uno) to accurately measure the angular speed of the motor shown in Fig. 3.1;

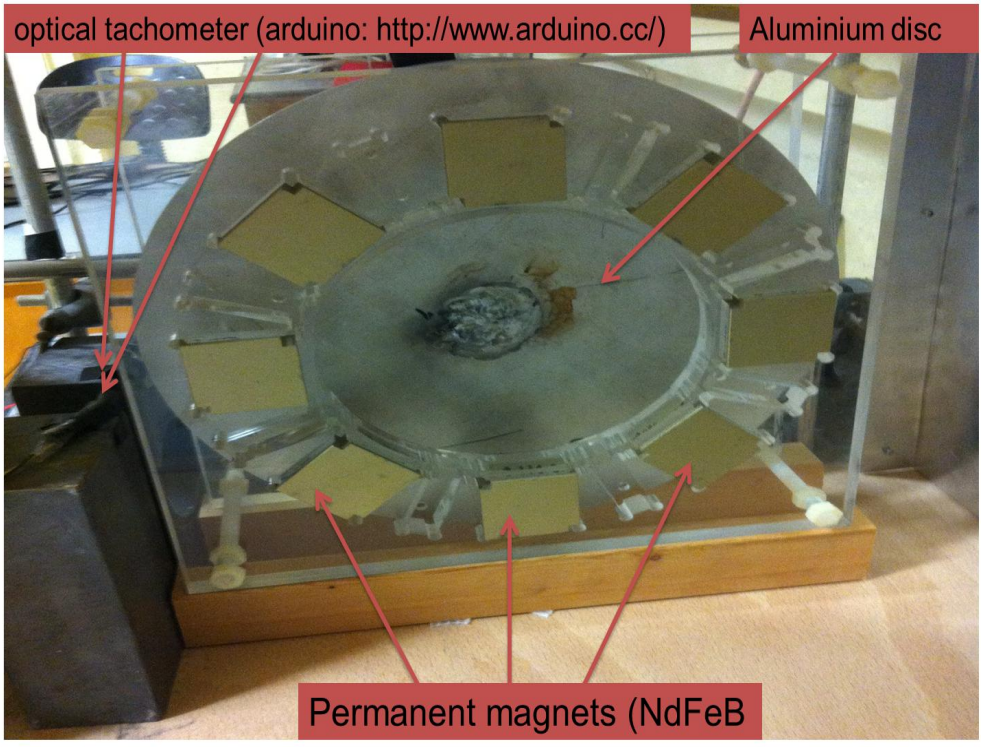

FIGURE 3.1: The image shows 8 magnets in the support structure in the foreground with aluminium disc behind it. The blocks on the left of the image act to provide more stability when wheel is running. The motor is directly behind the wheel.

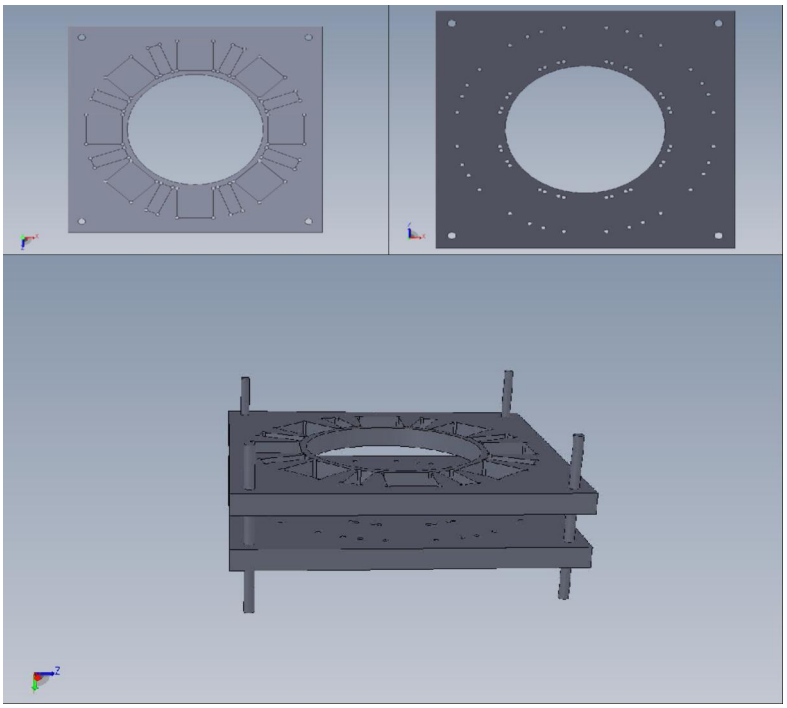

FIGURE 3.2: Magnet support structures made from strong plastic modelled in solidworks 3D software [44].

The circuit diagram of the IR detector which forms part of the optical tachometer is shown in Fig. 3.3

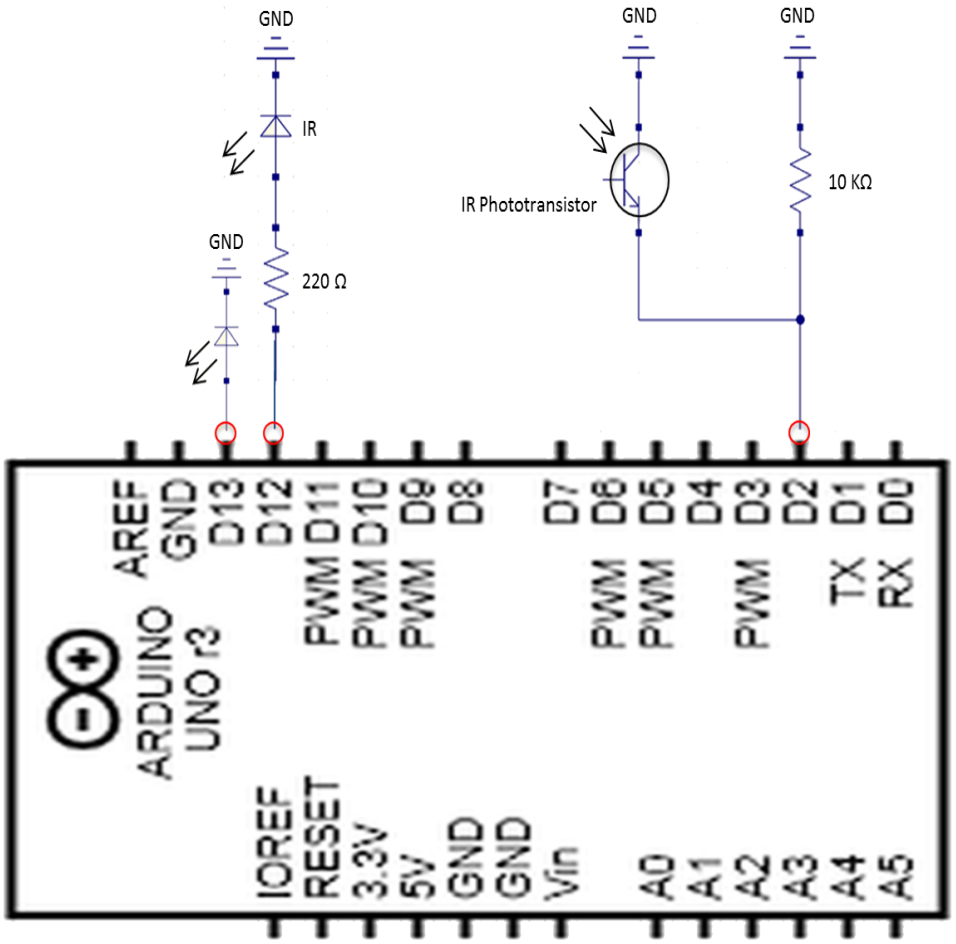

FIGURE 3.3: Circuit diagram for the IR detector. Light from the IR photodiode connected to digital I/O pin D12 is detected by the IR phototransistor connected to pin D2.

3.1.2 Experimental procedure

- The disc was attached to the motor and rotated.
- The magnetic field is mostly perpendicular to the disc movement.
- First, I powered the motor to measure the maximum speed, then we disconnected the power supply to the motor and measured the speed (the 2-second intervals are determined by the software) until the disc stopped moving.

- Then I added magnets into the magnet support structure one at a time and repeated the measurements.
- I calculated the torque from the measured moment of inertia of the disc and the measured deceleration.

3.1.3 Goals and Expectations

In order to find the torque produced by friction in the motor and air resistance, I calculated the moment of inertia using:

$$I = \frac{1}{2}MR^2, \tag{3.1}$$

where, I is the moment of inertia, M is the mass of the disc, and R is the radius of the disc. Then, we can calculate the torque using:

$$\tau = I\alpha, \tag{3.2}$$

where α is the angular acceleration and estimated using

$$\alpha \approx \frac{\Delta\omega}{\Delta t}. \tag{3.3}$$

where Δt is the time between consecutive measurements and $\Delta\omega$ is the corresponding difference in the measured angular speed.

I repeated these steps when I added the magnets around the disc and then calculated the total torque τ_{total}. Later on, I subtracted the frictional component of the torque from the total torque to find the torque produced by the magnetic field.

3.1.3.1 Stopping Time

I compared the time it takes for the disc to stop after reaching the maximum speed when the motor is turned off with adding 1 magnet, 4 magnets, 5 magnets, 8 magnets, and no magnets. In Fig. 3.4, in particular we see the speed and time increase when we add the fifth magnet, as a result of the cancellation of the eddy current loops when they became close to each other.

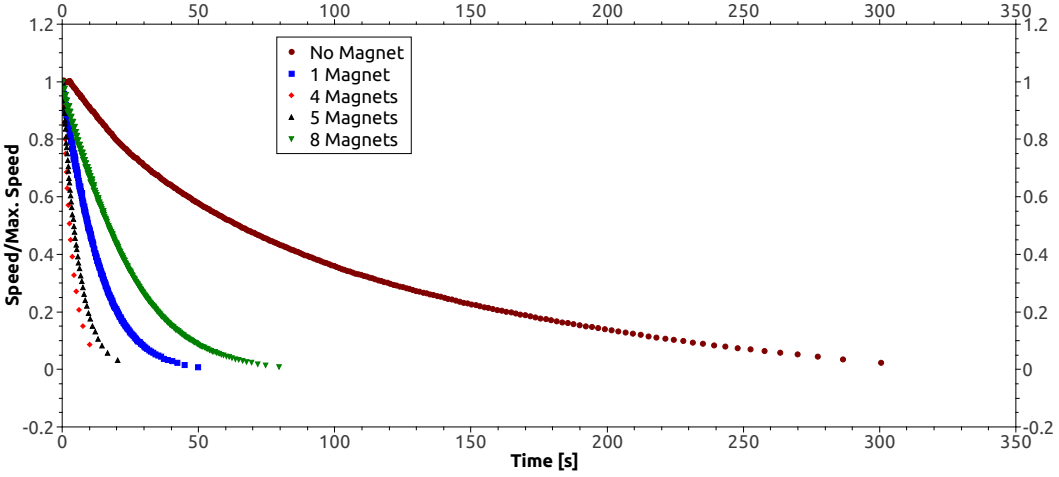

FIGURE 3.4: The speed/maximum speed changing with time with and without magnets as calculated from the rotating disc experiment.

Previous analytical studies (Smythe 1942, and Schiber 1974 [36, 45]) predict that the torque should be proportional to the angular speed of the disc. Assuming this and starting from Eq. (3.2) and Eq. (3.3) it follows that:

$$I\frac{d\omega}{dt} = b\omega, \tag{3.4}$$

from which it follows that

$$\int \frac{d\omega}{\omega} = b\int \frac{dt}{I}, \tag{3.5}$$

where b is a constant

$$\ln \omega = \frac{b}{I} \int dt, \tag{3.6}$$

$$\omega(t) = \mathrm{e}^{\frac{-b}{I}t}. \tag{3.7}$$

Rewriting Eq. (3.7) in terms of $\omega = \frac{\omega}{\omega_{max}}$ and, $t = \frac{t}{t_{st}}$

where, ω_{max} is the maximum speed of the disc and t_{st} is the 'stopping time' of the disc, I obtain

$$\frac{\omega}{\omega_{max}}(t) = \mathrm{e}^{\frac{-b}{I}\frac{t}{t_{st}}}. \tag{3.8}$$

In Fig. 3.5 we see the relation between $\log \omega = \frac{\omega}{\omega_{max}}$ and $t = \frac{t}{t_{st}}$.

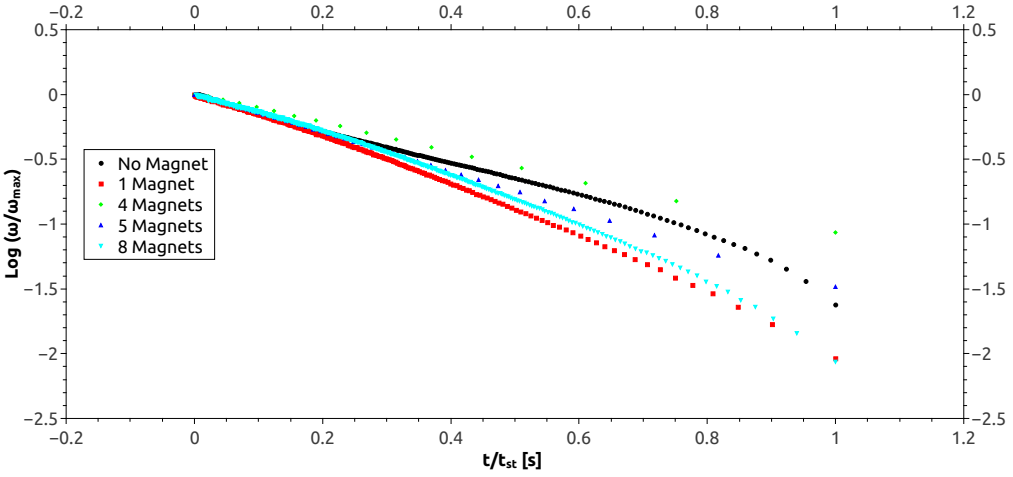

FIGURE 3.5: The log of speed/max-speed against the time/stopping time as calculated from the rotating disc experiment.

Fig. 3.5 shows good agreement with Eq. (3.8) in the case of 1, 4 and 5 magnets and the relationship is linear. The fit of a linear slope which fitted to a function

of the form $A + Bx$ shows that the ${}^{\chi^2}/_{doF}$ is close to 1. In the case of no magnets and 8 magnets when the wheel feels less torque, we can see there is less agreement with Eq. (3.8) (the ${}^{\chi^2}/_{doF}$ is approximately 1.8).

3.1.3.2 Braking Torque

Here I show the effects of the torque generated by the movement of the disc inside the magnetic field. I used Eq. 3.2 to calculate the torque, and plot it against the speed as shown in Fig. 3.6. We can see clearly how the torque increases approximately linearly as a function of speed.

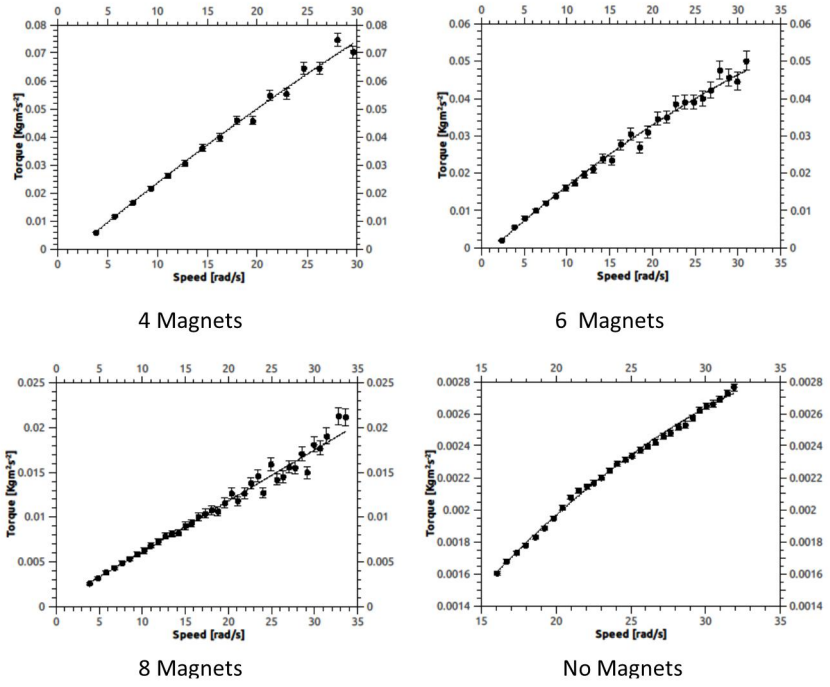

FIGURE 3.6: Torque plotted against speed for 4 magnets, 6 magnets, 8 magnets, and no magnets as calculated from the rotating disc experiment. The error bars show the statistical uncertainty and were calculated by repeating the measurement 3 to 5 times.

Fig. 3.6 shows the best fit for the torque using this equation:

$$\tau = A\omega^2 + B\omega + C \tag{3.9}$$

where ω is the speed, and from this slope we found the parameters of A, B, and C. The parameters are shown in table 3.1.

TABLE 3.1: Parameters of the slope of the best fit for the torque using Eq. 3.9.

Magnets	A	B	C	$x^2/_{doF}$
None	-1.5e-06	1.4e-04	-3.2e-04	1.13
1	-1.5e-05	1.6e-03	-2.3e-03	1.19
2	-8.8e-06	1.8e-03	-1.8e-03	1.27
3	1.0e-05	1.7e-03	-1.9e-04	1.20
4	-1.1e-05	3.0e-03	-5.3e-03	1.21
5	-5.8e-06	1.9e-03	-2.0e-03	1.21
6	-1.4e-05	2.0e-03	-2.8e-03	1.20
7	-1.0e-05	1.4e-03	-1.4e-03	1.25
8	1.0e-07	5.6e-04	4.9e-04	1.18

Now, these parameters will help us to extrapolate the torque for different speeds as shown in Fig. 3.7. However, the maximum speed when I started adding the magnets was limited due to the eddy current effects. For example when we added four magnets the maximum speed obtainable was 29.4 rad/s. By using Eq. 3.9 for different speeds, and using the values of A, B, and C for each number of magnets I obtained the results shown in Fig. 3.7.

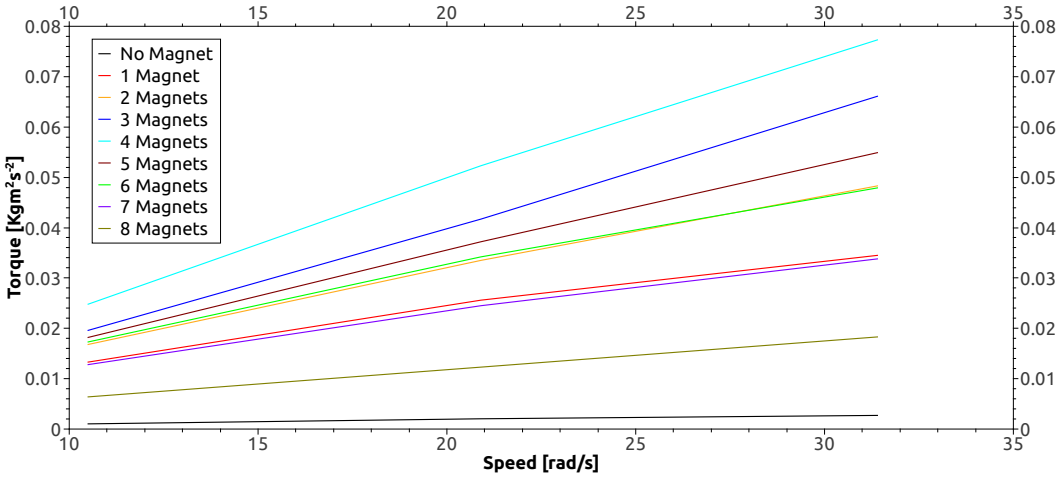

FIGURE 3.7: Torque calculated from equation 3.9 and table 3.1 plotted against the speed. Each color represent the torque from a number of magnets.

In Fig. 3.8 I show only the torque produced by the magnetic field after subtracting the value of the torque produced by the motor itself and air resistance.

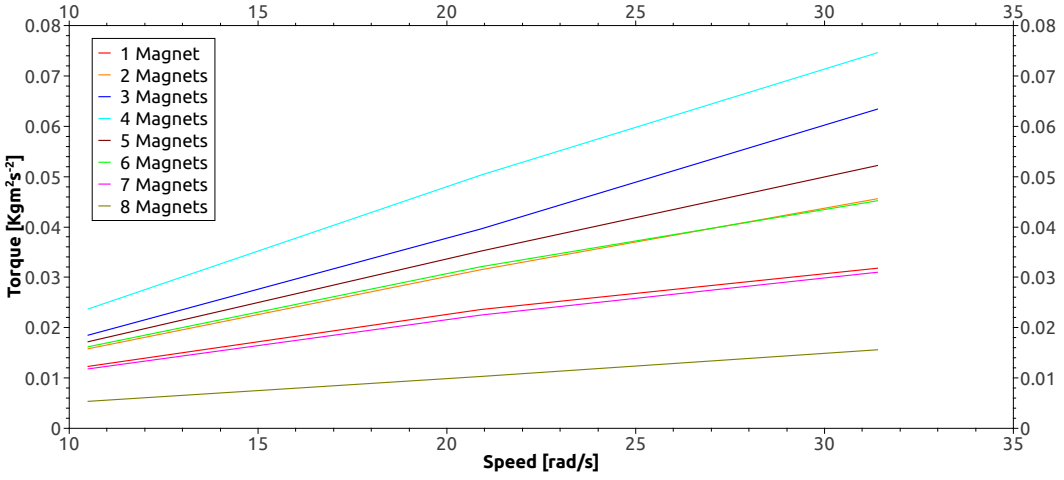

FIGURE 3.8: The measured torque from the magnets plotted against speed after subtracting the friction produced by the motor itself and air resistance. Each color represent the torque from a number of magnets.

In Fig. 3.9 shows the calculated torque from Eq. 3.9 and table 3.1 at a speed of 300 rpm and see how the torque changes experimentally while we increase the number of magnets around the disc.

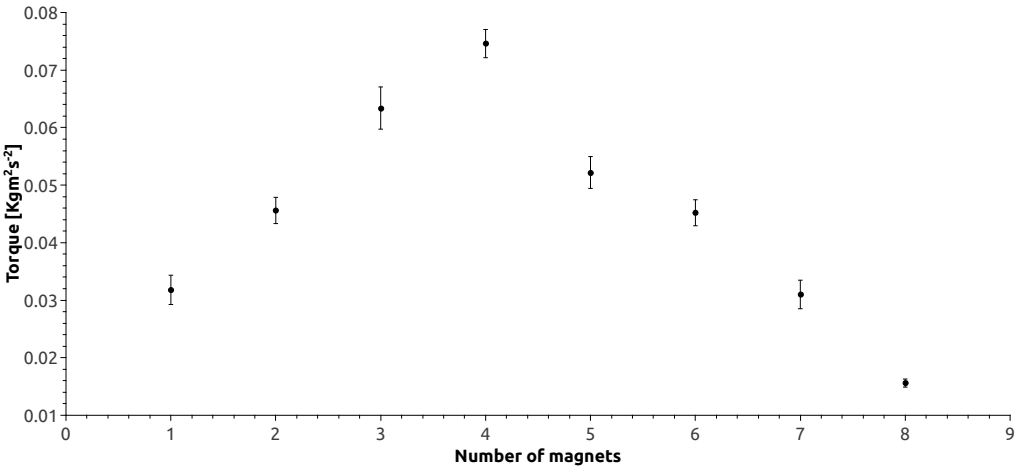

FIGURE 3.9: The measured torque as a function of number of magnets around the disc at a speed of 300 rpm. The error bars are coming from fitting to 3 data sets.

According to the results in Fig. 3.7, Fig. 3.8, and Fig. 3.9, we can clearly see that the torque reduces when we obtain a more uniform magnetic field (small magnetic field flutter). This experiment demonstrates the general principle predicted in previous theoretical studies. We can clearly see that when the magnets become close to each others, the eddy current loops start to cancel each other. That leads to a reduction in the torque acting against the movement of the disc.

3.2 Comparison between experiment results and OPERA 3D Simulations Results

3.2.1 Solid Disc

Simulations were performed using the OPERA 3D software to test the results of this experiment. An approximate model was designed to be similar to the one in

the experiment using OPERA 3D. Measurements of the magnet sizes, magnet distance from disc, magnetic field strength, etc were used in OPERA 3D model. The aim of doing these simulations was to test how good the OPERA 3D simulation is in these calculations, and up to what extent we are confident in our calculations. The OPERA 3D approximate model used to simulate the experiment is shown in Fig. 3.10. Fig. 3.11 shows the eddy current loops generated by the movement of the disc inside the magnetic field.

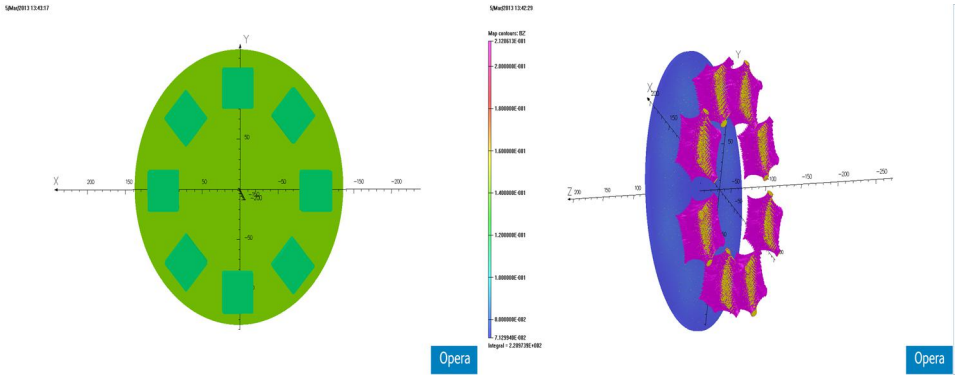

FIGURE 3.10: Approximate model from OPERA 3D and the magnetic field direction with a peak of 0.212 T. Left: the model before simulation with the disc shown in light green, and magnets shown in dark green. Right: the model after completion of the simulation, the disc in blue, and the magnetic field in purple.

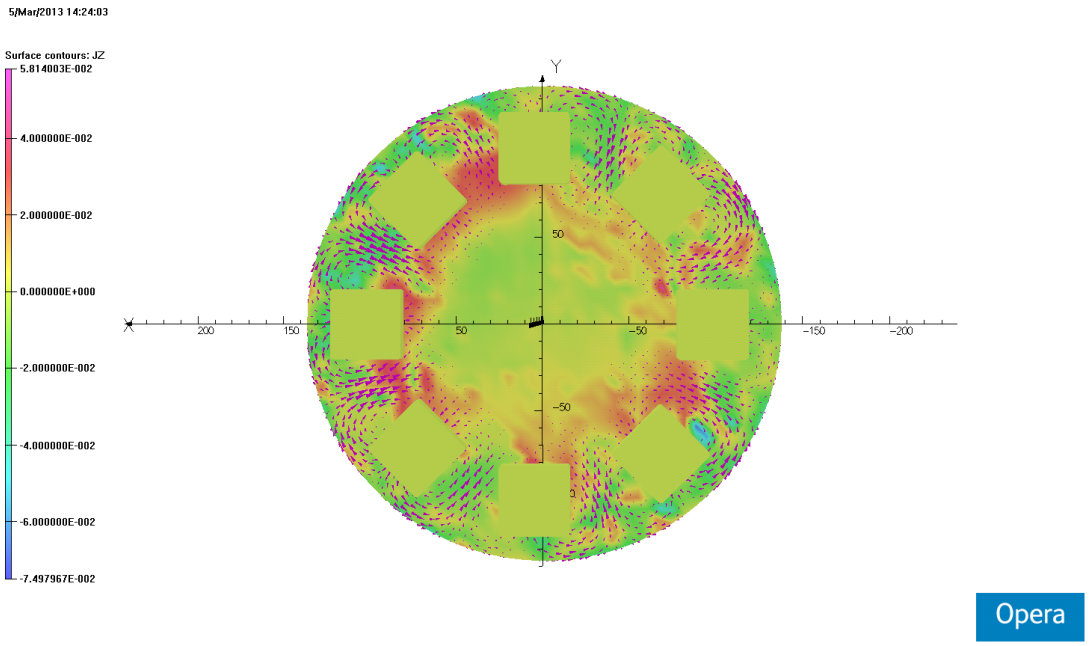

FIGURE 3.11: Eddy current loops (in purple arrows) generated by movement of the disc (in green) inside a constant magnetic field.

In the Fig. 3.12 I show the comparison between the results from the experiment and the results from the OPERA 3D software simulations. Red dots represent the simulated results and the black dots represent the experimental results. As we can see, there is good agreement in general at a level of approximately 3%. I think the small differences are mostly due to the results from the experiment as the stability of the disc is less when the disc feel more force during its movement. There is a visible vibration of the disc, especially, when the force became strong, due to the large magnetic field. From the figures, the maximum torque achieved was when we introduced the third and fourth magnet. The maximum torque was 0.0634 Nm when we introduced the third magnet and was 0.0746 Nm when the fourth magnet was introduced. The reduction of the torque starts when the fifth magnet was introduced and continues when we add more. Table 3.2 summarizes the values of the slopes in the figures.

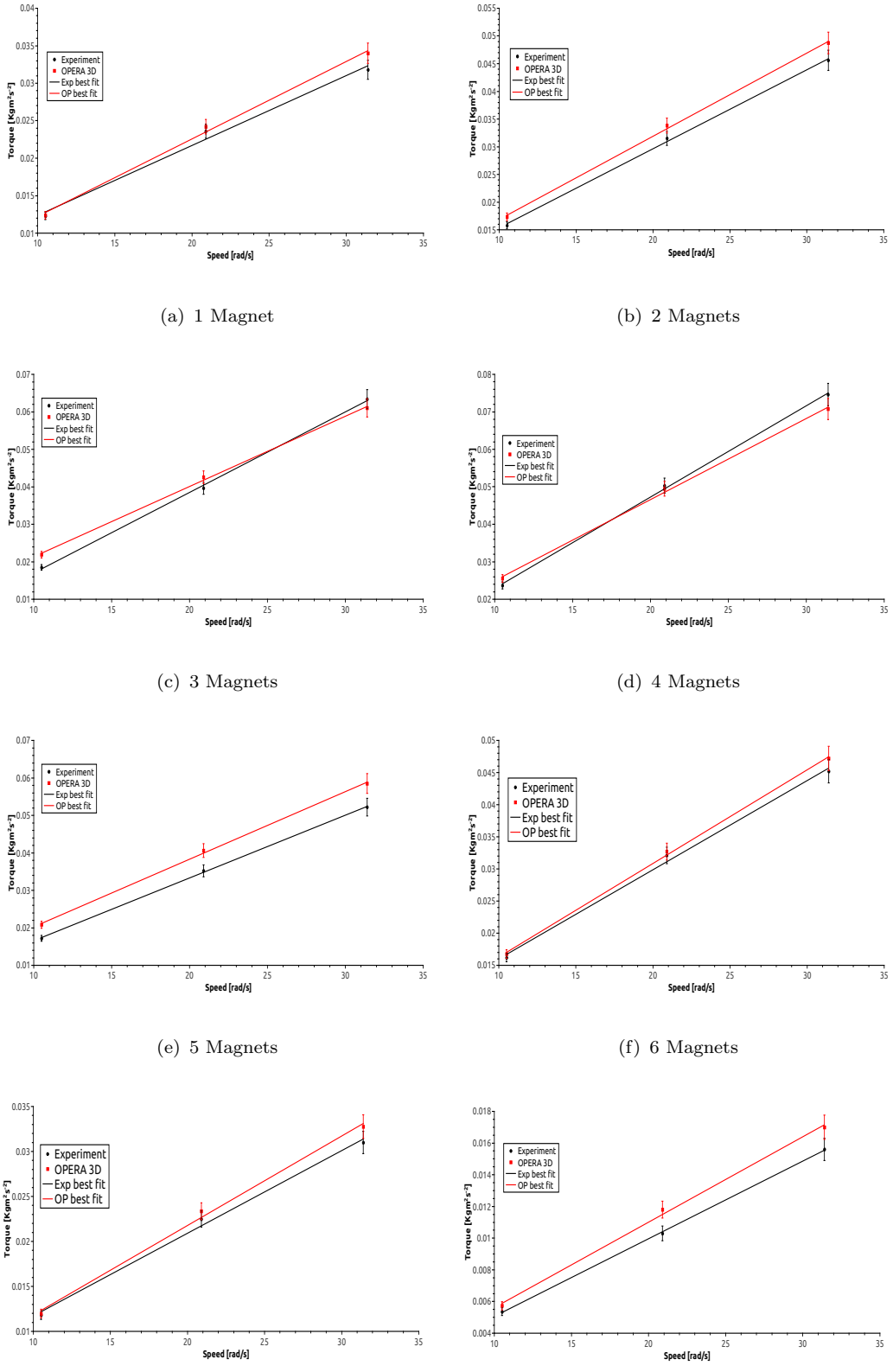

(a) 1 Magnet

(b) 2 Magnets

(c) 3 Magnets

(d) 4 Magnets

(e) 5 Magnets

(f) 6 Magnets

(g) 7 Magnets

(h) 8 Magnets

FIGURE 3.12: Comparison between experimental torque results and OPERA 3D simulations results for 1 to 8 magnets. The error bars are come from fitting to multiple data sets and the error estimated from OPERA 3D.

TABLE 3.2: Comparison of the rotating experiment and OPERA 3D simulation. The best fit slopes were obtained by fitting to a function A+Bx.

Magnets	A Exp.	A OP 3D	B Exp.	B OP 3D	ΔA	ΔB
1	3.0e-03	1.9e-03	9.3e-04	1.0e-03	2.0e-03	-7.0e-05
2	1.1e-03	1.8e-03	1.4e-03	1.5e-03	-7.0e-04	-1.0e-04
3	-4.4e-03	2.6e-03	2.1e-03	1.8e-03	-7.0e-03	3.0e-04
4	-1.4e-03	3.3e-03	2.4e-03	2.1e-03	-4.7e-03	3.0e-04
5	-1.8e-03	2.2e-03	1.6e-03	1.8e-03	-4.0e-03	-2.0e-04
6	2.1e-03	1.7e-03	1.3e-03	1.4e-03	4.0e-04	-1.0e-04
7	2.5e-03	1.8e-03	9.1e-04	9.9e-03	7.0e-04	-8.9e-03
8	1.6e-04	2.2e-04	4.8e-04	5.3e-04	-6.0e-05	-5.0e-05

The largest $\chi^2/_{doF}$ from the fits was 1.27 which shows that data was well represented by the linear function.

3.2.2 Thickness of the Target Wheel

The thickness of the target wheel is an important factor in the eddy current problem. In this study, I used the model shown in Fig. 3.10 with a fixed magnetic field with peak value ≈ 0.20 T, and fixed speed of 300 rpm. I set the thickness of the target to 6 mm, 7.5 mm, 9 mm, 10.5 mm, and 12 mm to study the effects. Fig. 3.13 shows how the torque increased as a function of thickness. The torque increased linearly as expected which again confirmed previous studies [36, 45].

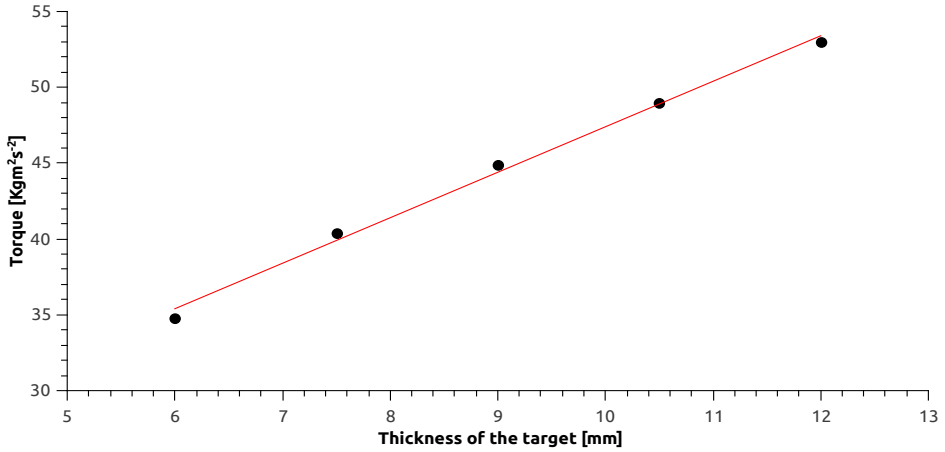

FIGURE 3.13: Simulated torque as a function of the thickness of the target wheel at a fixed speed of 300 rpm.

3.2.3 Spoked Wheel

In this section I present a small scale spoked wheel similar to the target wheel designed for the ILC which will be discussed in more detail in section 4.2. I tested the torque effects on the wheel experimentally and I compared the results to the OPERA 3d simulations. Finally I related the results to simulations of the real positron target wheel. The mini target wheel is shown in Fig. 3.14, and the corresponding OPERA 3D model is shown in Fig. 3.15.

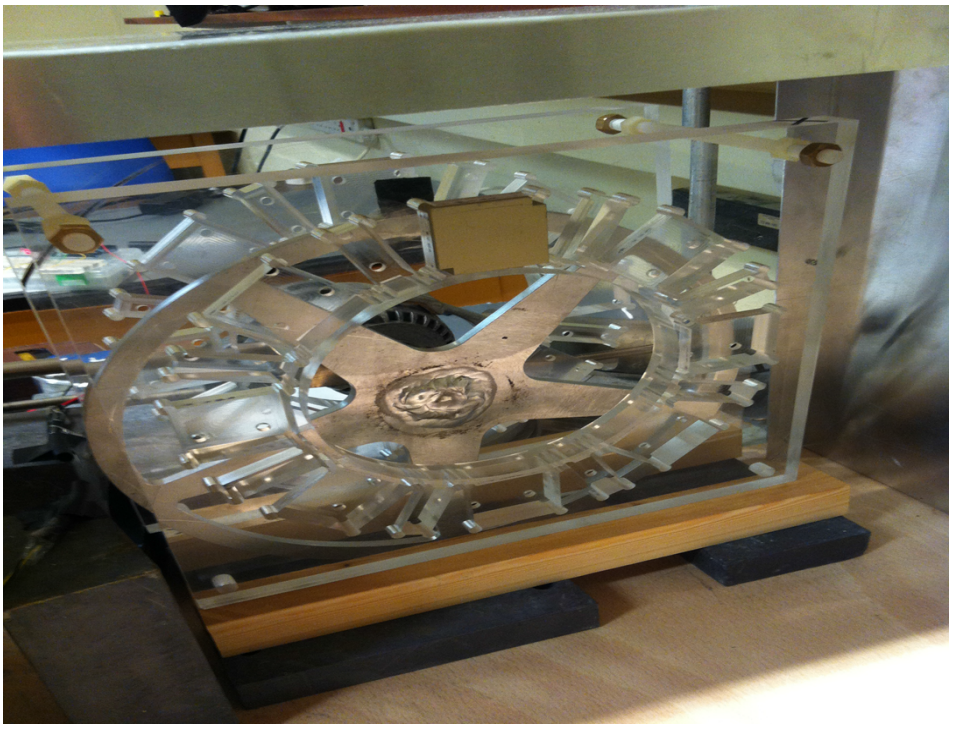

FIGURE 3.14: The image shows 1 magnet in the support structure in the foreground with the mini target wheel behind it. The blocks on the left of the image act to provide more stability when wheel is running. The motor is directly behind the wheel.

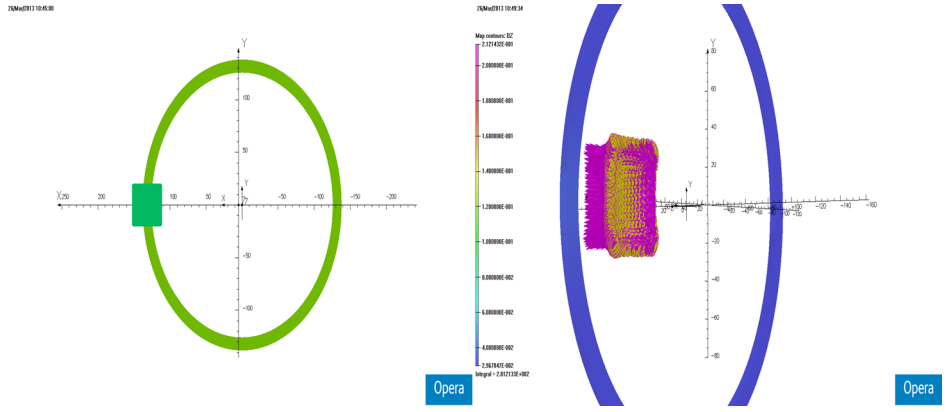

FIGURE 3.15: Approximate model for the mini target wheel from OPERA 3D and the magnetic field direction with a peak of 0.212 T. Left: the model before simulation and the rim shown in light green, and the magnet showing in dark green. Right: the model when the simulation finished, the rim is shown in dark blue, and the magnetic field is shown in purple.

In OPERA 3D software, I could not simulate the full model of the spoked wheel due to the limitation of the licence. The results from the experiment are shown in Fig. 3.16. It is clear that the rim wheel has a small torque compared to the solid disc, and this is due to the small size of the eddy current acting on the rim wheel compared with the solid disc.

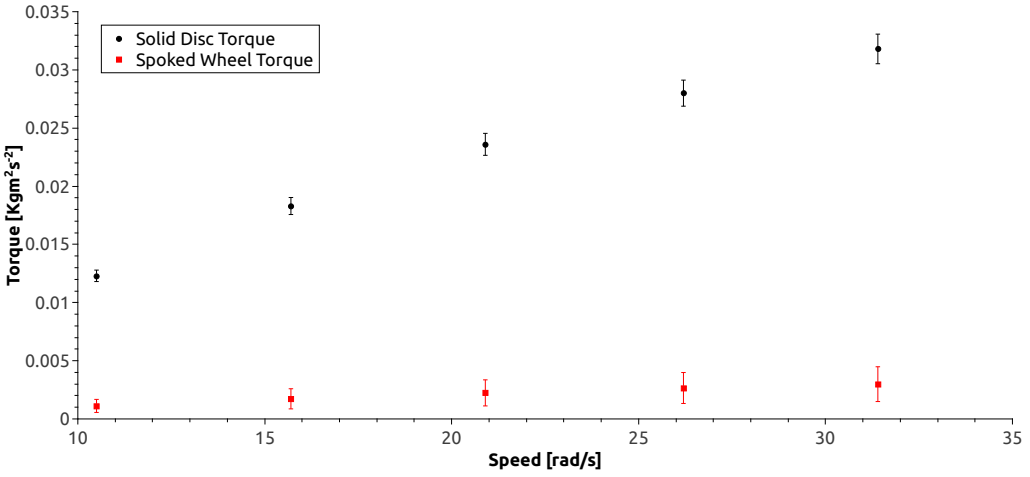

FIGURE 3.16: Comparison between the measured torque for the mini target wheel and the solid disc at ≈ 30 rad/s with a peak of 0.212 T. The error bars show the statistical uncertainty calculated by repeating the measurement 3 to 5 times.

On the other side, with no magnet, the rim wheel has a large measured friction torque compared with the solid disc and this is due to the air resistance. Results are shown in Fig. 3.17.

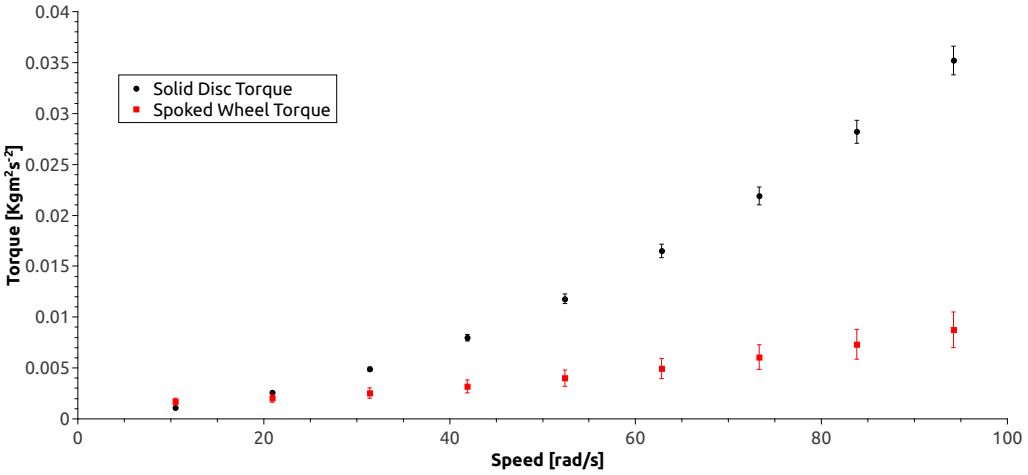

FIGURE 3.17: Comparison between the measured friction torque without magnets due to the air resistance for the mini target wheel and the solid disc. The error bars show the statistical uncertainty calculated by repeating the measurement 3 to 5 times.

Now, by comparing these results to the OPERA 3D simulations for the model in Fig. 3.15, we find large difference between them and the experimental results for the spoked wheel $\approx 80\%$. This difference is due to the effect of the five spokes in the actual experiment design, which we cannot simulate using OPERA 3D software due to the limitation in our user licence as mentioned earlier. However, I increased the rim size by 50%, 75%, and 90% to take this effect into account, and to see whether we can get better results [46]. The results are shown in Fig. 3.18.

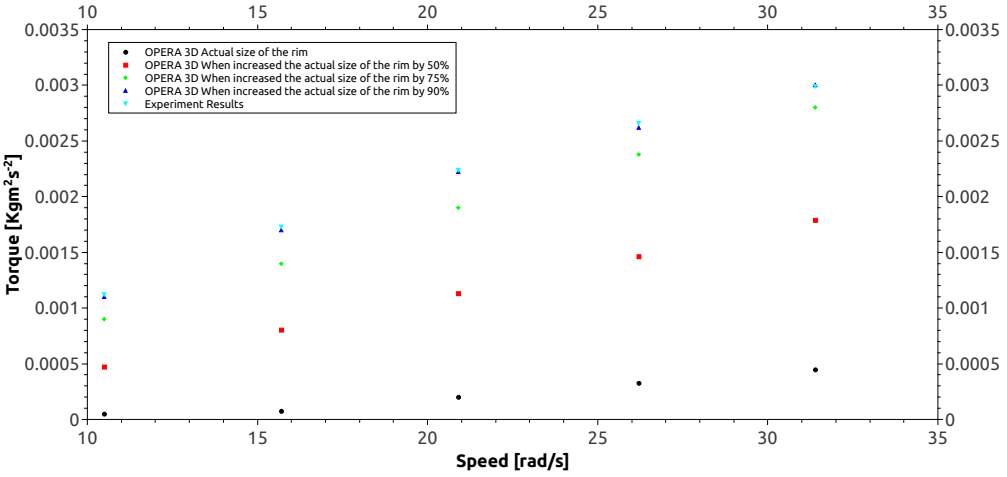

FIGURE 3.18: Comparison between torque effect for the mini target wheel experiment and OPERA 3D model simulations at 30 rad/s with a peak of 0.212 T.

I varied the rim width in the region between 80% to 100% to find the best fit of the data in steps of 5%. The best agreement is shown when I increased the rim size by 90% giving an agreement at the level of 2%.

3.3 Conclusion

In this chapter I have developed a low-cost experiment to demonstrate the principle of eddy current generation and validate the OPERA simulations. The torque acting on the movement of the disc and the level of the accuracy of OPERA 3D software are well understood. Good agreement and consistency with the previous studies and theory of the torque problem is demonstrated.

I reduced the torque experimentally by making the magnetic field more uniform as expected. When I compared the results from the experiment and the simulations, there was good agreement (approximately 3%) between the experiment results and

the OPERA 3D software simulations. This give me the ability to carry out simulations for the required parameters of the ILC target wheel with more understanding of the simulation tool and their limitations.

I have investigated the relationship between the torque and the thickness of the target, which was a linear relationship. Finally, I investigated the spoked target wheel experimentally and it is clear that the torque acting on the movement of the spoked target is very small compare to the torque acting on the movement of the solid disc. Due to the limitations of the licence, I could not simulate the full model of the spoked target wheel, but I increased the size of the rim to take into account the effect of the five spokes.

Chapter 4

ILC baseline target wheel

4.1 Introduction

In the previous chapter, I carried out a proof of principle experiment and a number of simulations to study the eddy current effect on a rotating solid disc and a spoked wheel. Experimentally, and using OPERA 3D software[43], I calculated the torque produced from a magnetic field which affects the disc and the spoked wheel movement. I added a number of magnets around the wheel to study the effect of eddy currents. As expected I found that we measured less torque when the magnetic field became uniform around the wheel. In this chapter I apply these principles to the ILC baseline target.

4.2 ILC Target Wheel

As described early in the description of the ILC positron source, there will be a rotating target wheel in which gamma rays are converted to electrons and positrons. The target wheel will be a circular rim with 1 m diameter, approximately a thickness of 0.4 radiation lengths, and 30 mm in a radial width. The target rim needs

to be rotated at a speed of 100 m/s $\sim$ (2000 rpm) to reduce the thermal effects due to the beam energy deposition, and make sure this target can survive for a long time as the target is intended to last for two years. Titanium alloy Ti-6%Al-4%V will be used to make the target wheel. The previous prototype constructed at Daresbury Laboratory for the target wheel is shown in Fig. 4.1 [47]. In Table 4.1 the proposed parameters for the ILC target wheel are shown. The target wheel will have a cooling system which will help to reduce the heating effects. This could be done by providing an internal water- cooling channel inside the target wheel [48].

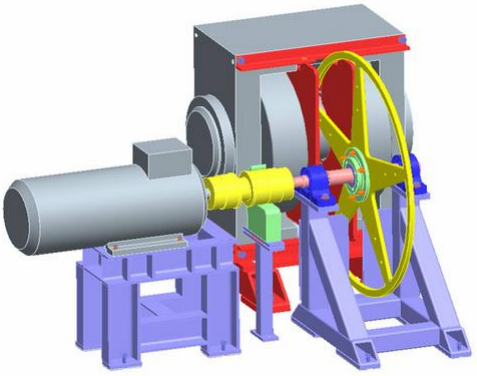

FIGURE 4.1: ILC target wheel prototype. Target rim (yellow) immersed in pole caps H-frame dipole magnet (two gray cylinders with the target wheel between them). The motor used to rotate the wheel is shown on left (gray). The yellow cylinder on the drive shaft is a torque transducer which was used to measured the torque. This figure was reproduced from [47].

Any positrons produced will need to be focused by a solenoidal magnetic field, otherwise we will end up with losing most of them, and this could lead to damage to other equipment. Therefore, we need to introduce a solenoid magnet with a high peak field approximately 6 Tesla just before the target and another one after the target to allow us to have a continuous magnetic field to guide the positrons. This

TABLE 4.1: ILC Target Wheel Parameters [48].

Parameters	Values
Target material	Ti-6%Al-4%V
Target thickness	1.4 cm
Target power adsorption	8%
Incident spot size on target	1.7mm
Wheel RPM	2000 rpm
Rim velocity	100 m/s

solenoid magnetic field should reach 0.5 Tesla after the target to match the capture section field when the beam reaches there. Introducing a solenoidal magnet will increase the efficiency of capture more than 40% [46]. However, in the current ILC TDR design [3] the solenoidal magnet has a peak field of 3.2 T which will not give better capture efficiency than what is introduced here. There are problems raised with this design due to the eddy current effects when the target wheel rotates and is partially immersed in the field of the matching device. The force acts to stop the target movement, and the corresponding heating effect can become a problem with this design. Therefore, we must find a solution to solve these problems, otherwise we have to change the entire design of the target wheel. Later in this chapter I introduce the problems and solutions in details.

4.3 Target Simulations

Back in 2009 when the prototype experiment at Daresbury Laboratory took place they used the experimental set-up shown in Fig. 4.2. We can clearly see that a part of the target is immersed in a magnetic field. The target wheel was connected to a torque transducer to calculate the torque acting on the wheel. A number of simulations using the OPERA 3D code [43] were done, and a semi-analytical model was used to calculate the estimated torque. The Opera model which was used is shown in Fig. 4.3 [46].

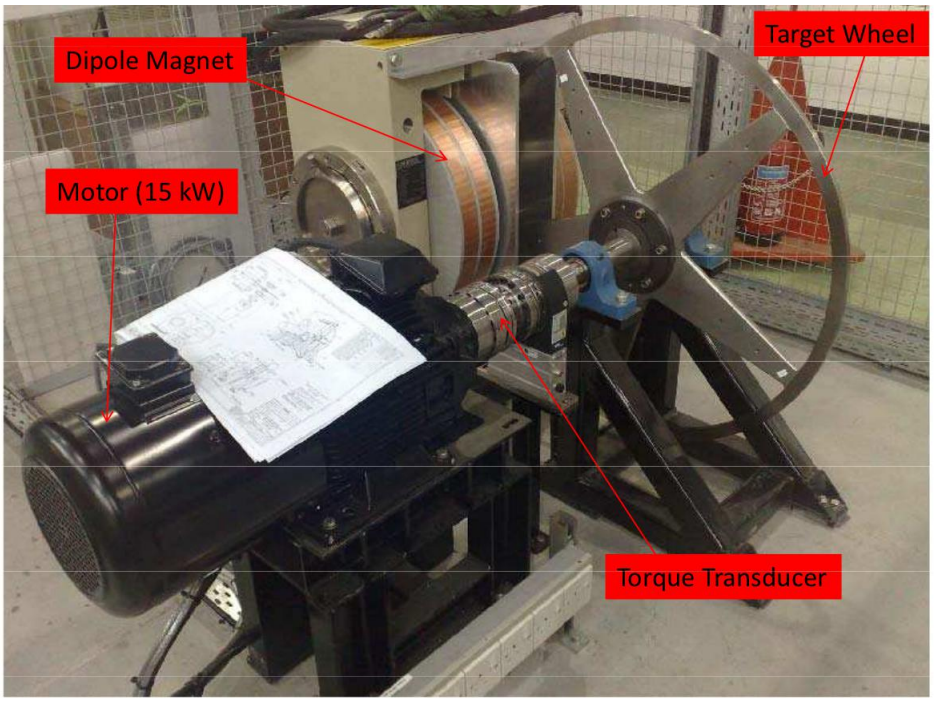

FIGURE 4.2: Target prototype setup at Daresbury Lab [46].

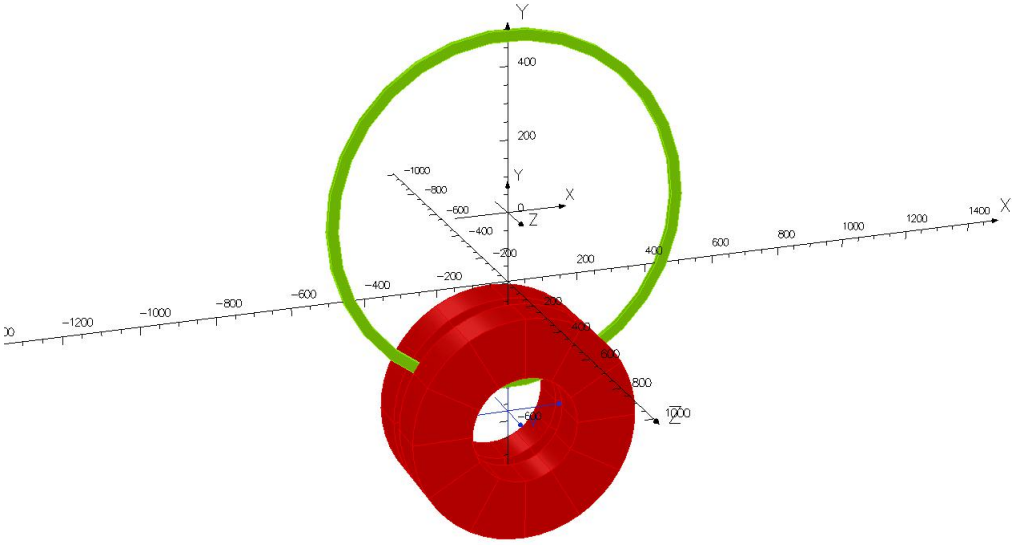

FIGURE 4.3: Opera model which used for the comparison in the Daresbury studies. The solenoid magnet is shown in red, and the rim is shown in green [46].

A 10% agreement was found between the experimental results, analytical estimate, and Opera calculations as shown in Fig. 4.4. The blue dots are the result from Opera, red dots are the result from a semi-analytical estimate described later, and the solid line is the results from experimental test (a quadratic fit to the data). The results from these studies showed that there is a torque between 5 Nm to 13 Nm effect trying to stop the wheel due to eddy currents. Also, the simulations showed the torque has a strong dependence on the radial width of the wheel. In the experimental design there are five spokes. As in the studies shown in chapter 3 of the thesis, OPERA 3D can not test the full geometry, therefore, in the semi-analytical estimate and OPERA 3D simulation, the radial width of the rim was increased by 50% to give a good approximation to take in account the five spokes which appeared in the experimental design. The target was rotated at speeds of 100 - 2000 rpm in a magnetic field with strength $\sim$ 0.485 T [46]. Also, several immersions depths were tested showing that the torque increased from 5 Nm to 13 Nm as the wheel immersed between 20.25 mm and 50.25 mm [49]. I reproduced the same model using OPERA 3D and the agreement is in a level of $\approx$ 5%. The result is shown in Fig. 4.4.

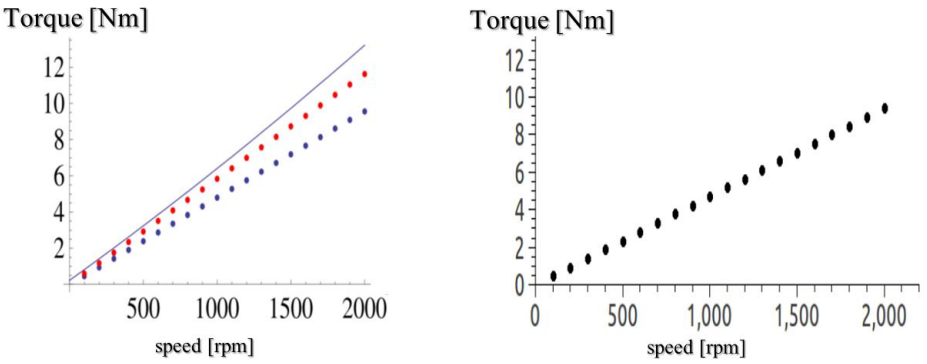

FIGURE 4.4: The figure on the left is torque data results collected from the Daresbury experiment (solid line), semi-analytical estimate (red dots), and Opera simulation (blue dots) [46].The figure on the right is torque data from my model reproducing the Daresbury work.

I ran this model using the Opera simulation for the real parameters required for the ILC target wheel. I increased the peak magnetic field up to $\sim 6\,\mathrm{T}$, let the target rotate at different speeds ($\sim 250 - 2000\,\mathrm{rpm}$), and tested the radial width of the rim for 30 mm and 45 mm. The magnetic field variation around the rim is shown in Fig. 4.5. There is a big variation of the magnetic field around the wheel, hence we will have eddy current loops. Results are shown in Fig. 4.6. According to these results, we know for sure it's not possible to have this design in ILC target wheel, unless the value of B is very low (less than 1 T) where the torque is $\approx 40\,\mathrm{Nm}$.

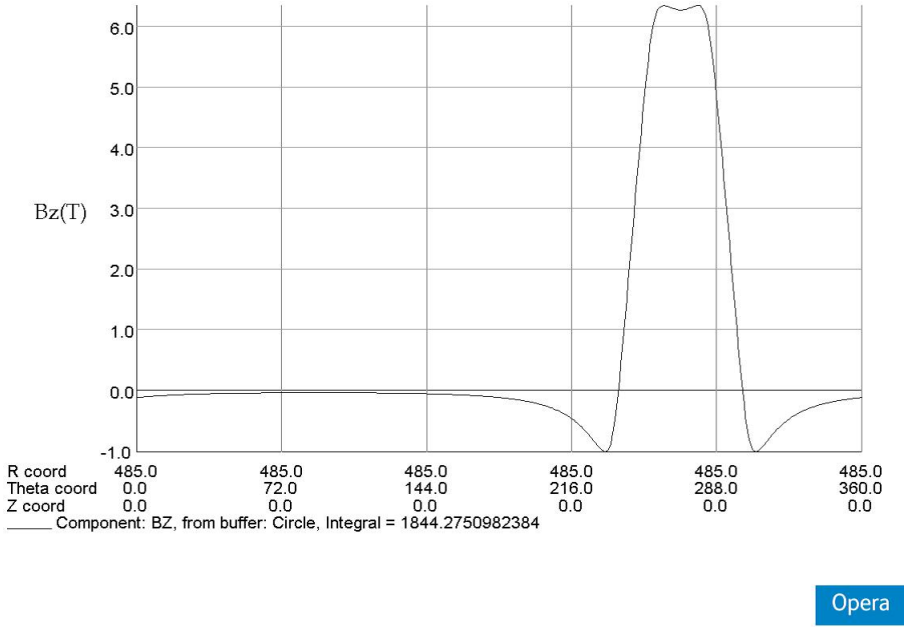

FIGURE 4.5: Z component of the magnetic flux density around the wheel rim at a fixed radius of 0.485 m, with the wheel. Where z is the direction perpendicular to the wheel movement.

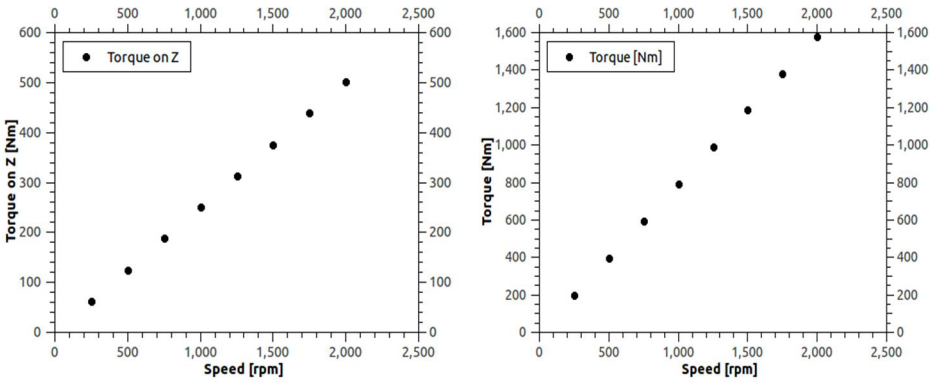

FIGURE 4.6: Torque result from Opera 3D for the target wheel immersed in a magnetic field strength $\sim 6\,\mathrm{T}$, and the radial width of the rim is 45 mm(right), 30 mm(left).

4.4 New Simulation Results

4.4.1 Comparison between C Model dipole Magnet and Solenoid Magnet

To validate my simulations, I started with a single C-magnet model. In this model the target wheel will be immersed partially as it is in the solenoid magnet model. I compared it with the previous solenoid simulations. Simulations were done for both solenoid and C-model with a peak magnetic field $\sim 1.5\,\mathrm{T}$ and different rotation speeds. The single C-magnet model and the eddy current generated from it are shown in Fig. 4.7. I found a 5% agreement applies to the torque between the result which I got from C magnet model simulation and the solenoid magnetic simulation, in terms of producing same eddy current loops and a torque of $\approx 21\,\mathrm{Nm}$ acting against the target movement. The result is shown in Fig. 4.8.

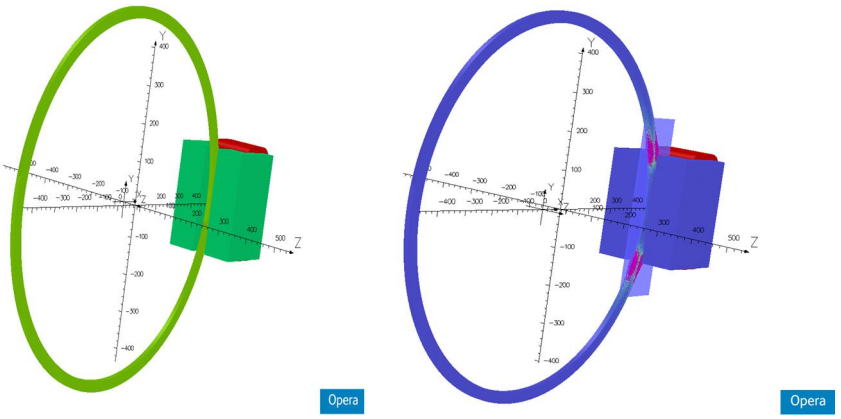

FIGURE 4.7: The single C-magnet model (in green) is shown on the left and eddy current loops generated (in purple) from it is shown on the right when the target partially immersed. The coil to produce magnetic field in C-magnet model (in red).

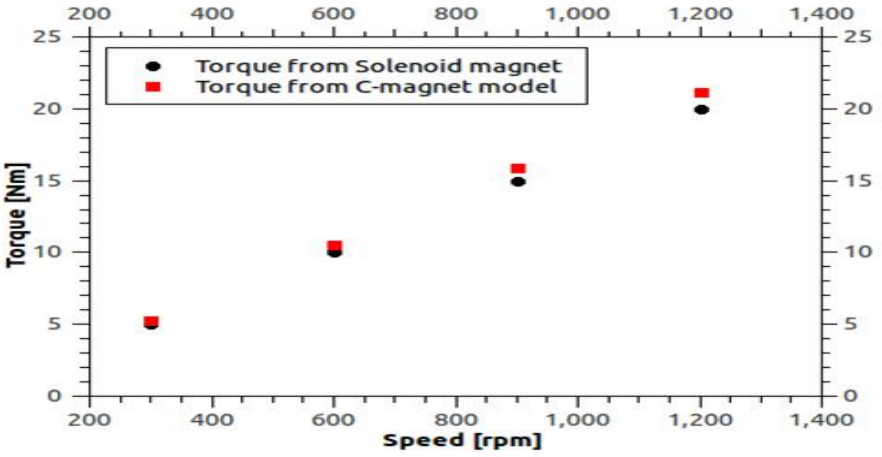

FIGURE 4.8: Results from the comparison between the C-magnet model (in red) and solenoid model (in black) at a peak magnetic field ~ 1.5 T.

4.4.2 Torque vs. Increasing The Number Of C Magnets Around The Target Wheel

From the results in chapter 3 we can see that if we make a uniform magnetic field around the wheel then that will reduce the eddy current loops. In other word,

when there are two close magnetic field parallel to each others, the eddy current loops will start to cancel each other and the net current will be zero. I did a number of simulations to test this principle. I started to add C-magnets to the model one at a time around the wheel, as shown in Fig. 4.9. Simulations were carried out for rotating the target wheel at a speed of 300 rpm and magnetic strength ~ 0.97 T. The results from these simulations are shown in Fig. 4.10.

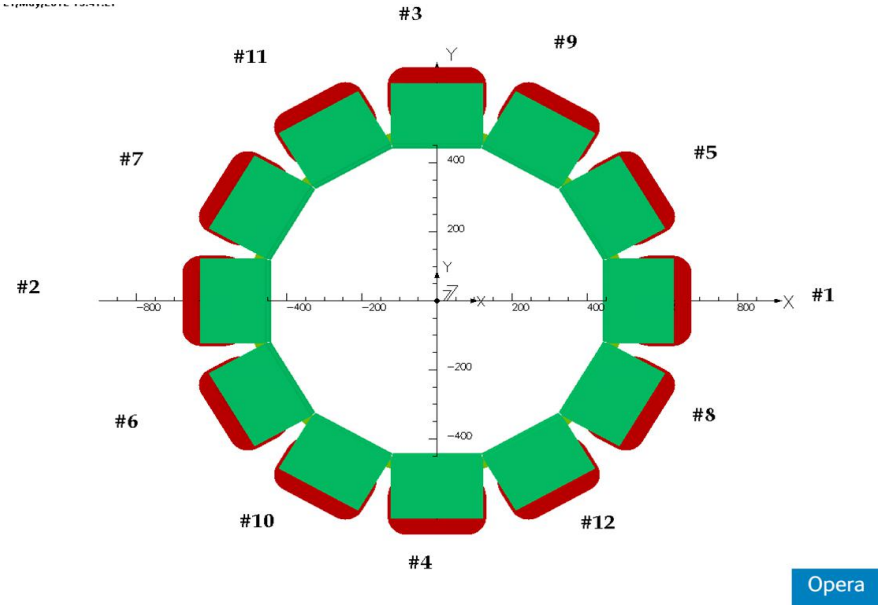

FIGURE 4.9: Target wheel immersed in 12 C-magnetic model. The numbers around the outside of the image show the order of adding the magnets in each simulation.

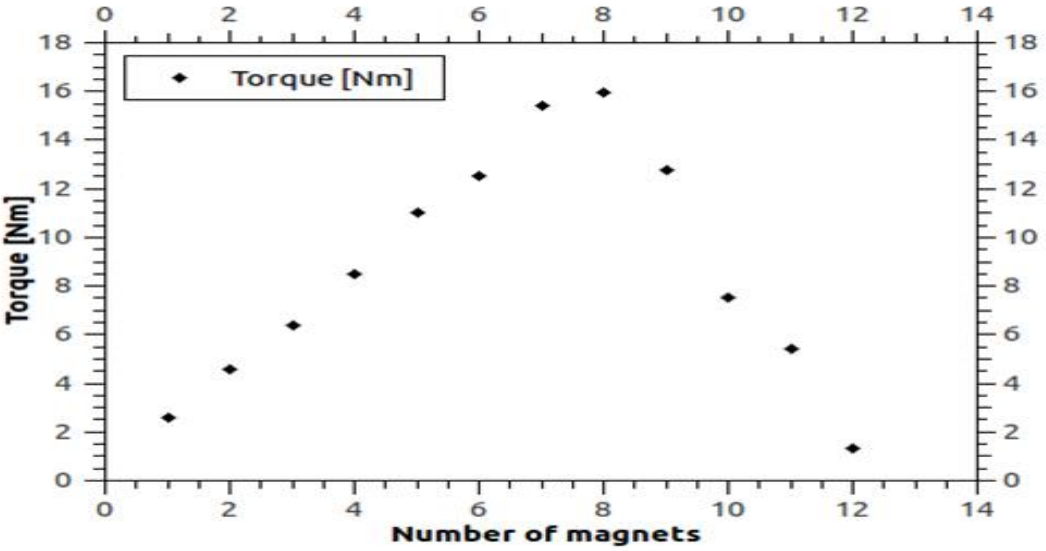

FIGURE 4.10: Torque effects, while we increase the number of C-magnet models around the target wheel. The magnetic field strength $\sim 0.97\,\mathrm{T}$, and the wheel is rotated at 300 rpm.

Now, according to these results, we can clearly see that when the magnetic field become more uniform, the torque in the z direction reduces to 1.3 Nm from a peak value of $\sim 16\,\mathrm{Nm}$.

I improved this model by connecting the C-magnets together by a thick iron ring as shown in Fig. 4.11, which is my final design. Connecting the C-magnets with each other leads to improving the magnetic field in terms of field variation. After joining the C-models together, the torque in the z direction reduced to 0.09814 Nm from a peak value of 0.99 Nm. The magnetic variation for the 12 C-magnet models before joining each other, and the magnetic field variation after joining the C-magnet models together, is shown in Fig. 4.12.

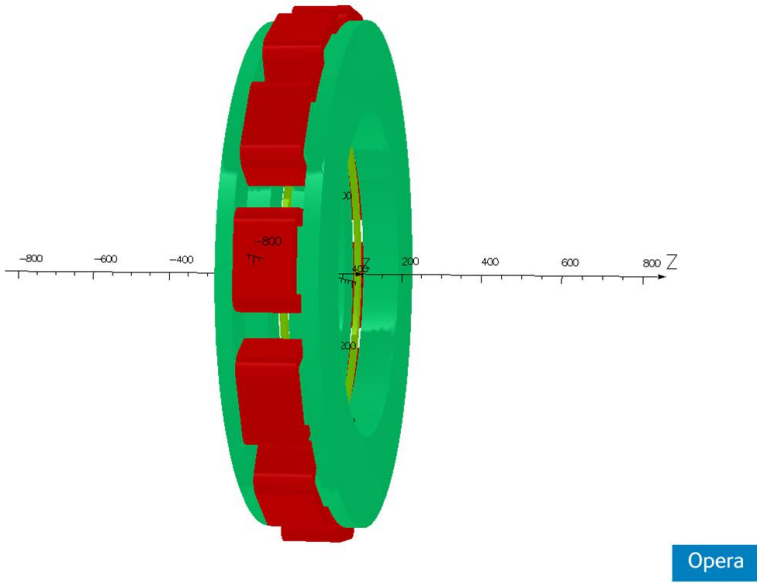

FIGURE 4.11: C-magnet model (in green) when the pole caps are connected, target rim (in light green), and a coil to produce the magnetic field in the C-magnet model (in red).

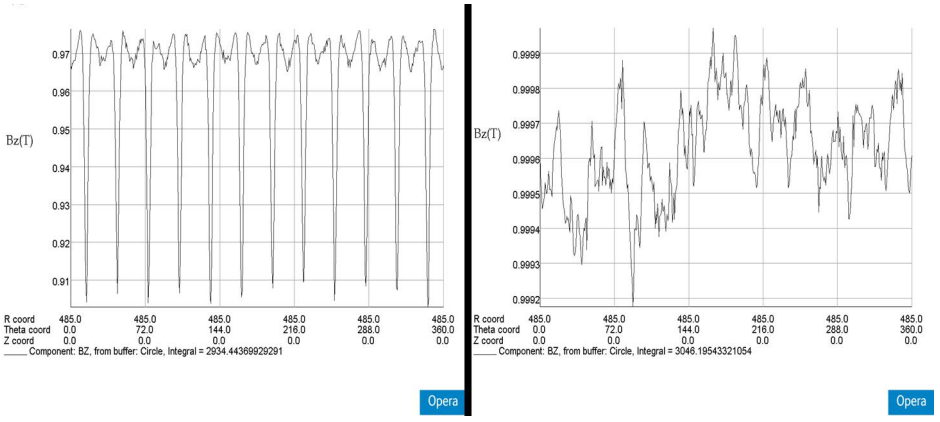

FIGURE 4.12: Z component of the magnetic flux density around the wheel rim at a fixed radius of 0.485 m, with the wheel. The figure on the left shows the magnetic flux density strength before joining the C-model, and the figure on the right after joining them together. Where z is the direction perpendicular to the wheel movement.

4.4.3 Torque vs. Velocity

I used the model shown in Fig. 4.9, in a magnetic field with peak value ~ 2.7 T, and I increased the speed each time by 300 rpm. Results are shown in Fig. 4.13.

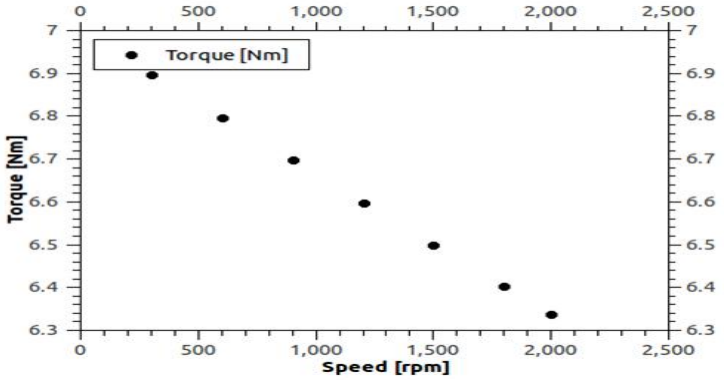

FIGURE 4.13: Torque behavior in a uniform magnetic field with peak value ~ 2.7 T, when the speed was increased by 300 rpm each time.

As we can see, if we have a more uniform magnetic field, when the target speed increased each time, the eddy currents start to produce a magnetic field against the main magnetic field. That leads to a reduction in the torque when the speed keeps increasing. In 1942, a paper discussed a disc rotating in a non-uniform magnetic field, and proved that, the torque reduced at high speeds [36]. In this case, the wheel is rotating in a magnetic field with small differences, and we can see this effect clearly.

4.4.4 Torque vs. Size of the rim

In this section, I am going to study the change of the rim size and whether this has effects on the torque or not. In this study, I used the model shown in Fig. 4.11, a fixed magnetic field with peak value ~ 1.5 T, and fixed speed 2000 rpm. I changed the radial width of the rim for a different size (30 mm, 40 mm, 50 mm, 60 mm, and 70 mm) to study the effects. Results are shown in Fig. 4.14.

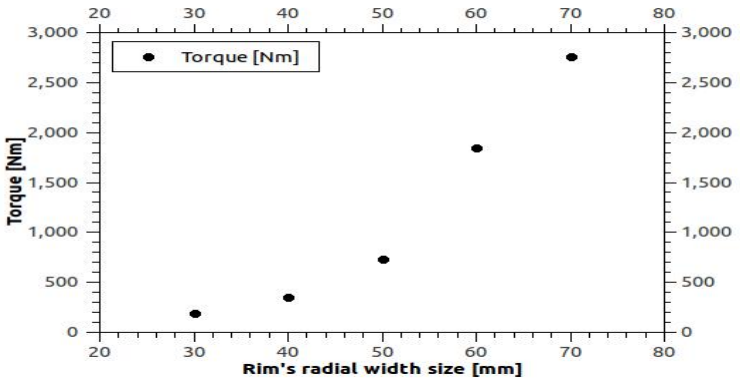

FIGURE 4.14: Torque in the z direction when the rim's radial width size change.

As we saw the torque keeps increasing when the size of the rim is increased. This agrees with the results from the previous Daresbury studies [36].

4.5 Final Model

4.5.1 Introducing The Solenoid Field To The Model

In the ILC positron design, we mentioned that there must be a magnetic field to focus the positrons when they are produced from the target. So, we need to introduce a solenoid field to our final C-magnet design to allow focusing of the positrons. An OPERA model with a solenoidal magnet and the simulated field variation after introducing the solenoidal magnet are shown in Fig. 4.15 and 4.16 respectively.

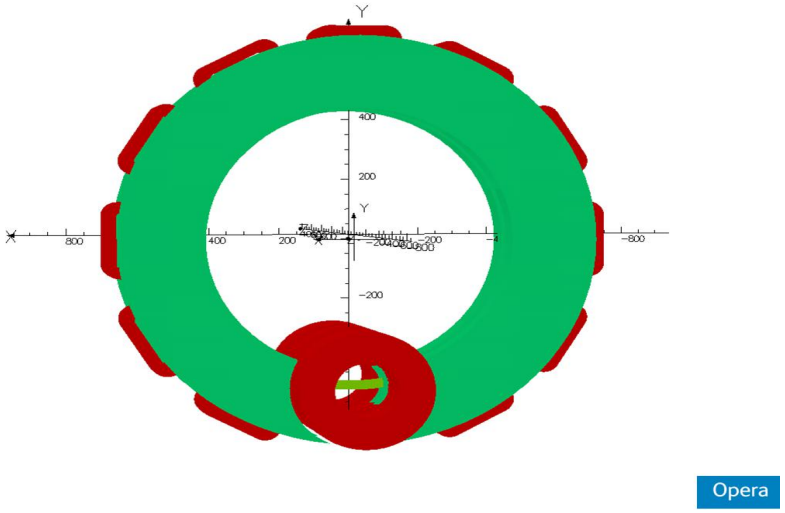

FIGURE 4.15: OPERA 3D model showing final C-magnet design when solenoid magnetic introduced. The magnets are shown (in red), target rim (in light green) and C-magnets (in green)

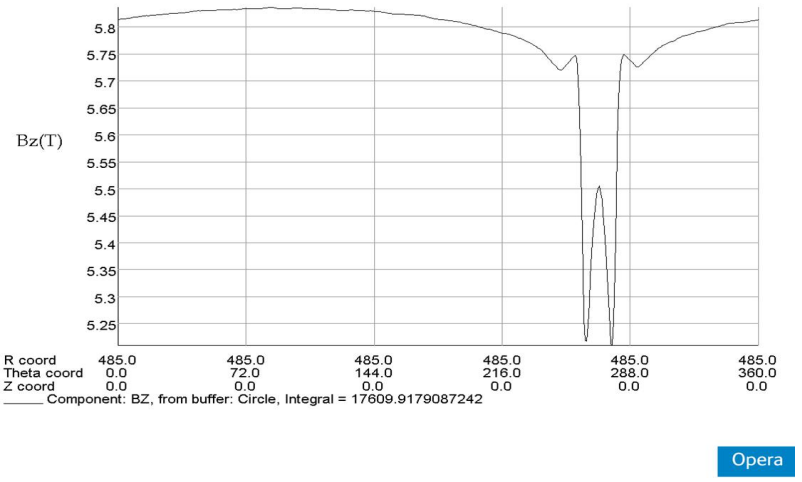

FIGURE 4.16: Z component of the magnetic flux density around the wheel rim at a fixed radius of 0.485 m, with the wheel, when solenoid magnetic introduced. Where z is the direction perpendicular to the wheel movement.

4.5.2 Semi-analytical Model

Now, I use a semi-analytical model of the target to compare it with my simulation results. The aim of this semi-analytical model is to give an understanding of the

physics and to see if the results from the simulations are correct or not. Following the same argument as used in reference [46] I assume that there is a metal bar with a cross-section immersed in a magnetic field (parallel to the z direction) and moving at constant velocity (in the x direction) as shown in Fig. 4.17. The direction of movement is parallel to the bar's length. The magnetic field strength varies as a function of position. The edges in z and y directions have lengths a_z and a_y respectively.

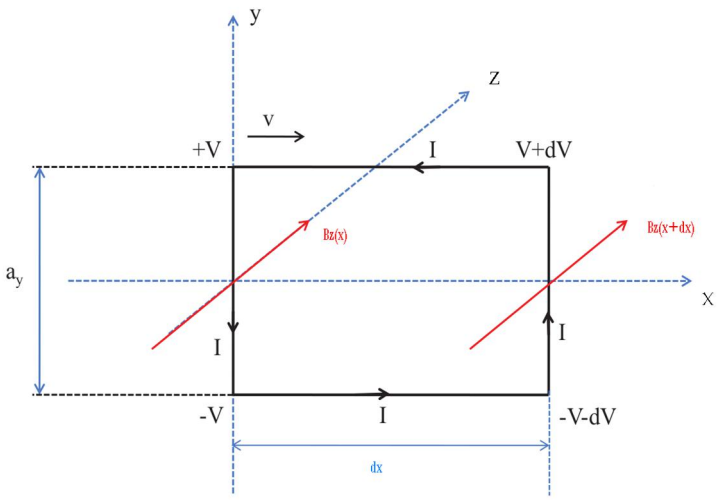

FIGURE 4.17: Target's semi-analytical model moving in a magnetic field.

The target's rim is represented by this bar. I am ignoring the circular motion in this model, as the radius of the target wheel is much larger than the dimensions of the rim's cross-section. In this model I calculate the force acting against the wheel movement, but in order to find the force, the eddy currents produced in this bar must be calculated. Because of the movement of the metal bar in a magnetic field, there will be a voltage induced in y direction as shown in Fig. 4.17. The induced voltage will vary as a function of x, because the magnetic field strength varies as a function of x. The voltages shown in Fig. 4.18 are:

$$V = \oint E.dl = -\frac{d\Phi_b}{dt} = B\frac{dA}{dt} = -\frac{Blvdt}{dt} = -Blv. \tag{4.1}$$

Just set $l = a_y$ here, and $B = B_z$.

By taking the difference between the voltage at two points in the x direction, and $y = a_y$, and a small distance dx in the x direction, we will have:

$$dV = \frac{1}{2}v\frac{dB_z}{dx}dxa_y. \tag{4.2}$$

Because the voltage varies linearly with y, we can find the current density J as a function of y through :

$$J(y) = \sigma\frac{dV}{dx}\frac{y}{a_y/2} = \sigma v\frac{dB_z}{dx}y. \tag{4.3}$$

The total current dI in a thin slice in this bar with height dy along the full width a_z of the bar is given by:

$$dI(y) = J(y)a_z dy = \sigma v\frac{dB_z}{dx}a_z y dy. \tag{4.4}$$

There will be a closed current loop. So, consider the current flowing in the y direction, and the magnetic field in the z direction acting on this current. According to the Lorentz equation, there will be a magnetic force in the x direction as a result of this, given by:

$$d^2F_x = (B_z)_x dI(y)2y - (B_z)_{x+dx}dI(y)2y = -2\frac{dB_z}{dx}dI(y)ydx. \tag{4.5}$$

Substituting from Eq. (4.4) this becomes:

$$d^2F_x = -2\sigma v\left(\frac{dB_z}{dx}\right)^2 a_z y^2 dy dx. \tag{4.6}$$

To find the total force acting on a small distance of the bar with a length of dx, I sum over the force produced by currents at all y positions of the bar:

$$dF_x = -2\sigma v\left(\frac{dB_z}{dx}\right)^2 a_z dx \int_0^{a_y/2} y^2 dy = -\frac{1}{12}\sigma v\left(\frac{dB_z}{dx}\right)^2 a_z a_y^3 dx, \tag{4.7}$$

and integrate over the remaining length of the bar to find the total force:

$$F_x = -\frac{1}{12}\sigma v a_z a_y^3 \int\left(\frac{dB_z}{dx}\right)^2 dx. \tag{4.8}$$

If there is uniform field in the z and y directions, a_z and a_y can be combined to get the volume integral:

$$F_x = -\frac{1}{12}\sigma v a_y^2 \int\left(\frac{dB_z}{dx}\right)^2 dV. \tag{4.9}$$

Finally, the torque is given by:

$$\tau = rF_x = -\frac{1}{12}\sigma\omega r^2 a_y^2 \int\left(\frac{dB_z}{dx}\right)^2 dV. \tag{4.10}$$

Where σ is the conductivity of the material, and $\omega{=}\frac{v}{r}$. Note that F_x is in an opposite direction to the target's movement [46, 50].

Now I apply in Eq. (4.10) to the model used in the OPERA 3D simulation, to see if it does give the same result. In our case the conductivity of the Ti-6%Al-4%V is $5.8 \times 10^5\,\Omega^{-1}\mathrm{m}^{-1}$ [46]. The rim has a width a_y of 30 mm, and revolution

frequency of 2000 rpm $\approx$ 100 m/s. I did the integral using the simulated magnetic field shown in Fig. 4.18, and obtained:

$$\int \left(\frac{dB_z}{dx}\right)^2 dV \approx \sum_{\theta=0^0}^{60^0} \left(\frac{dB_z}{dx}|_\theta\right)^2 \approx 0.009496\,\mathrm{T^2m}. \tag{4.11}$$

Using this result in Eq. (4.10) gives $\tau \approx 20.65\,\mathrm{Nm}$, which is within $\approx 2\%$ of the result from OPERA 3D.

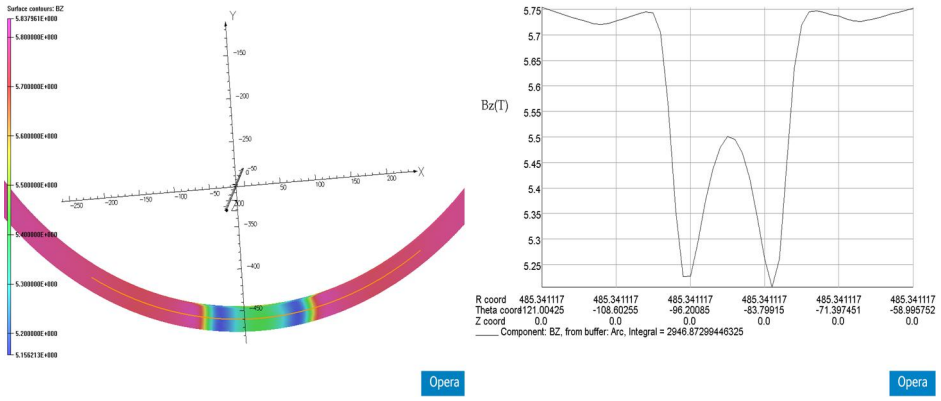

FIGURE 4.18: The simulated magnetic field variation as a function of angle around a specific area where there are differences in the field. The angular speed of the wheel was 2000 rpm.

4.5.3 Matching solenoid field

The solenoid magnetic field should reach 0.5 Tesla after the target to match the capture section field. In the proposed design, we need the magnetic field to start from the target's downstream face at approximately 5 Tesla and decrease to 0.5 Tesla at a distance around 40 cm from the target's downstream face. In this case, it is a matter of changing the distance of the solenoid magnet from the target wheel and changing the strength of the magnetic field. The dependence of the magnetic flux density in the z direction is shown in Fig. 4.19.

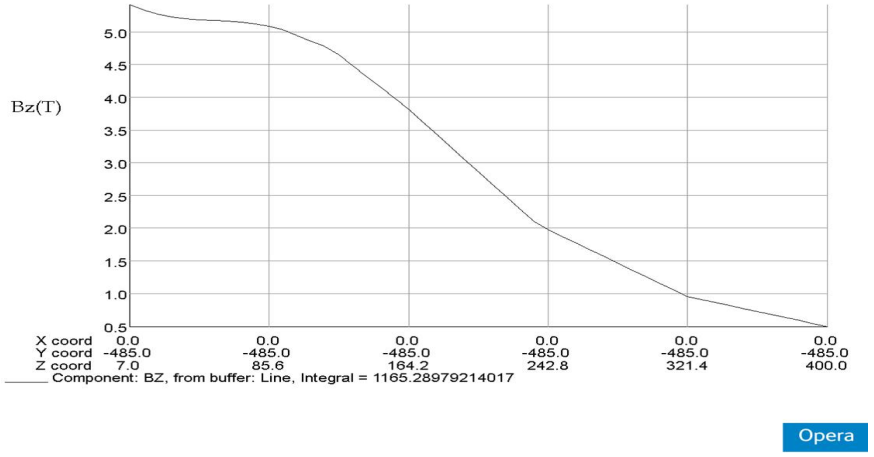

FIGURE 4.19: Magnetic flux density curve in the z direction in the region between the target rim, and capture rf cavity.

4.6 Torque transverse to the drive shaft

Torque transverse to the drive shaft could cause stress on bearings or feedthroughs. Our initial studies indicate that there is a torque around x and y because of the fringe field of the C-model pole cap. In the C-magnet model without the solenoid magnet, I increased the size of the pole caps, and observed that the torques around x and y both reduced. So, the torque around x and y can be removed either by increasing the size of the pole cap or by shaping the edge of the pole cap [51].

When I introduce the solenoid magnetic field, there is no way of reducing the torque transverse to the drive shaft without having gaps between magnets and some changes of the field. In my final design shown in Fig. 4.15, the simulations give the torques in table 4.2.

TABLE 4.2: Torque from final design [Nm]

Direction	Torque [Nm]
X	13.063
Y	10.751
Z	20.416

As we know the definition of the torque is :

$$\vec{\tau} = \vec{r} \times \vec{F}, \tag{4.12}$$

which implies that

$$\tau_x = (F_z r_y - F_y r_z)\hat{i}. \tag{4.13}$$

The force is given by

$$\vec{F} = Q(\vec{E} + \vec{v} \times \vec{B}) = \vec{I} \times \vec{B}, \tag{4.14}$$

and

$$F_z = (B_y I_x - B_x I_y)\hat{k}. \tag{4.15}$$

In Fig. 4.20 I show a closer picture of the current flowing inside the target wheel.

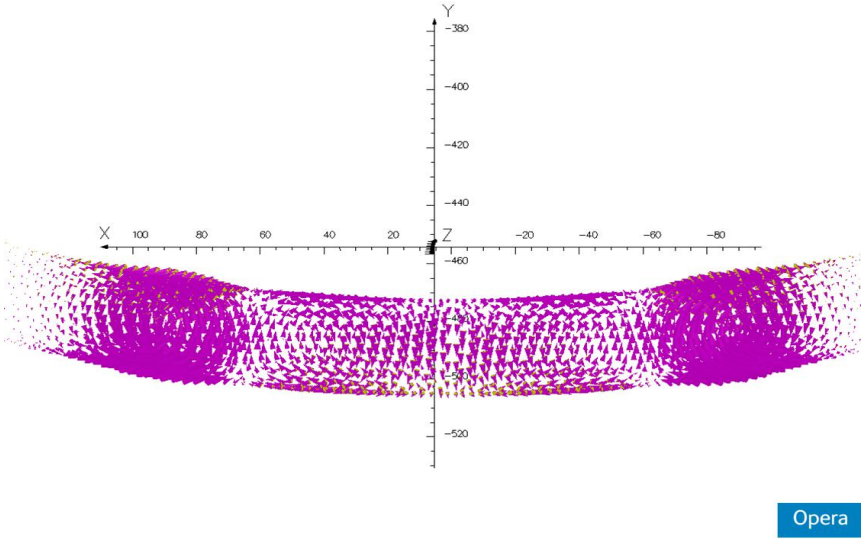

FIGURE 4.20: Direction of current flowing inside the target wheel. Explain what we seeing of torque

From Eq. (4.13) a torque in the x direction is due to a force in the z or the y directions. Because r_z is very small I ignore the second part in Eq. (4.13). Now, from the definition of the force acting in the z direction in Eq. (4.15), there must be either magnetic flux in the y direction and current in the x direction or magnetic flux in the x direction and current in the y direction.

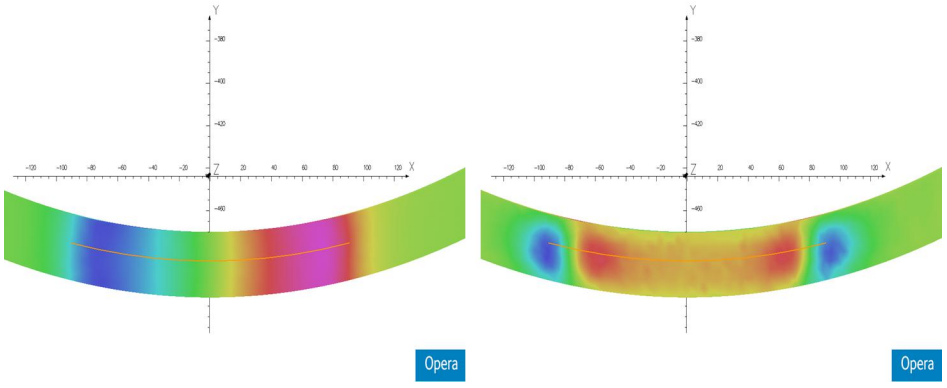

FIGURE 4.21: Magnetic flux in the x direction shown on the left, and current flux in the y direction shown on the right. Blue indicates the -ve sign, and purple indicates the +ve sign. The orange line shows where the magnetic flux and currents flux were measured as described below.

As can be seen from Fig. 4.21 there is a small area on the target rim where the magnetic flux and current flux are both large. I measured the strength of the magnetic field and current flowing in this small area by getting the average value along a line as shown in Fig. 4.21. The results are shown in Fig. 4.22.

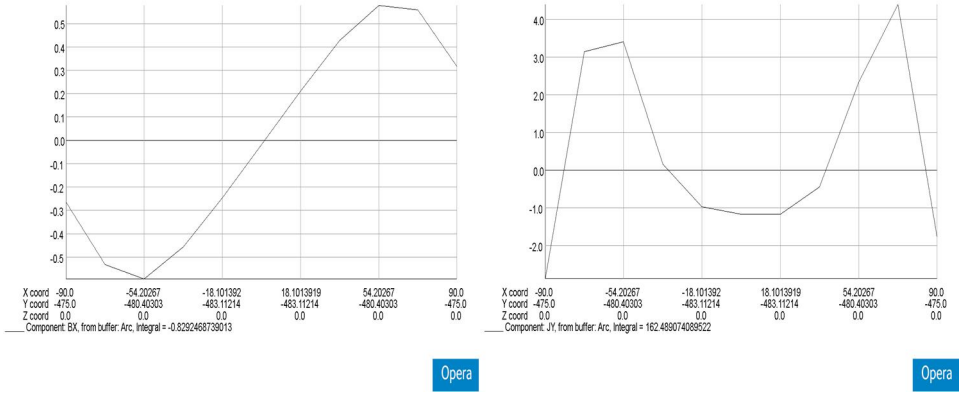

FIGURE 4.22: Magnetic flux strength in the x direction shown on the left, and current flux strength in the y direction shown on the right.

$$\tau_{x\otimes} = F_{z\otimes} r_y \approx 21.8 \times 0.5 \approx 10.9\,\text{Nm}$$

Do similar to $F_{z\odot}$ on the left we get:

$$\tau_{x\odot} = F_{z\odot} r_y \approx 22.6\,\text{Nm}$$

$\tau_x = 11.3\,\text{Nm}$, Which is close to the result from OPERA 3D (the difference between them is less than $\approx 5\%$).

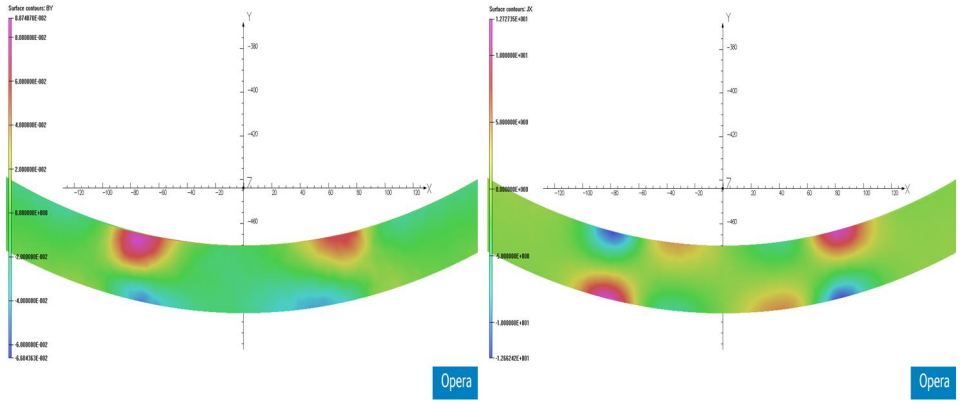

FIGURE 4.23: Magnetic flux in the y direction showing on the left, and current flux in the x direction showing on the right. Blue indicates the -ve sign, and the purple indicates the +ve sign.

$\tau_y = 11.67\,\text{Nm}$. Which is close to the result from OPERA 3D (the difference between them is less than $\approx 5\%$).

4.7 New proposed prototype

I produced a new design for the target wheel prototype using solidworks 3D software [44]. In this model, I am trying to show the final design for the positron target wheel with the C-magnet model in a realistic layout. It seems achievable and is not complicated. In this design, I haven't considered the infrastructure needed to support, power, and cool the magnets. Which, of course, need some participation from engineering groups. The proposed new prototype is shown in Fig. 4.24.

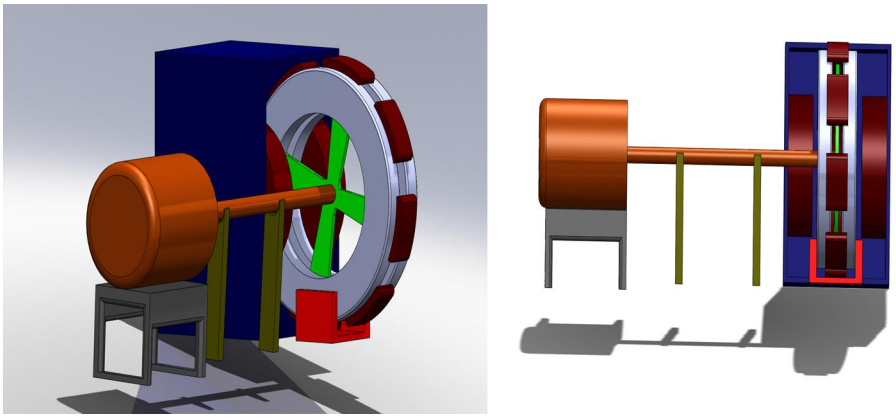

FIGURE 4.24: The proposed new prototype for the ILC positron target wheel. As shown in the picture, the light brown is the motor used to rotate the target wheel, the two big cylinders are solenoidal magnets (in dark red), the C magnets with coils (red) and a connected yoke (light grey) are shown surrounding the wheel (green).

4.8 Conclusion

The target wheel is on the critical path for producing a viable positron source for the ILC. As the positron flux needs to be high, this target needs to be rotated at a speed of 2000 rpm to reduce the thermal effects coming from the photon beam. Also, this target needs to be immersed in a strong magnetic field to focus

the produced positrons. Due to the movement of the target wheel in a strong magnetic field there are eddy currents providing a strong force against the wheel's movement. In this study I explored the torque effects in detail, and using OPERA 3D simulations I found an alternative arrangement of magnets to minimise the braking torque.

The torque in the previous prototype was approximately 500 Nm, when the wheel rotates at a speed of 2000 rpm, with rim radial width of 30 mm, and is partially immersed in a strong magnetic field with a peak of approximately 6 T. I introduced C-magnets around the target wheel to make the magnetic field more uniform. When the C-magnets were introduced around the wheel, the torque was approximately 20 Nm corresponding to a power loss of 4.19 kW. However, as mentioned earlier this is not the TDR design. The immersed high-field capture optics give an improved capture efficiency for the positrons, but the TDR design uses a lower field, with less immersion and a pulsed magnetic field.

Also, I studied the torque transverse to the draft shaft. I found that the torque around the x and y directions are caused by the fringe field of the solenoid magnet. The torque around x was 13 Nm, and around y was 10 Nm.

This is not a fully engineered design, but shows that this approach to reducing the eddy currents while increasing the positron capture is worth pursuing in the future.

Of course, in this design the C-magnets would need to be compact superconducting magnets. Also, I have not considered the infrastructure needed to support, power, and cool the magnets.

Chapter 5

Undulator Magnetic Field and Electron Trajectory

In section 2.3.3 the ideal magnetic field of the helical undulator was described theoretically. The trajectory of the electron beam inside the undulator determines the details of the gamma ray spectrum. Errors in the magnetic field cause the electron trajectory to be off-axis and could in an extreme case lead to beam loss. I developed a code using Mathematica [52] to generate a magnetic field map based on the Fourier power spectrum of any measured field map to investigate this effect.

In the ILC case to achieve the required gamma-ray flux from the ILC helical undulator, the electron beam needs to pass through a long helical undulator (approximately 147 m) successfully. This undulator contains 84 modules of length 1.7825 m. A dipole magnet can be used to correct the beam in between the modules to redirect the beam to the center of axis. Errors in the field can alter the flux, energy distribution and polarisation of the gamma rays.

5.1 ILC Helical Undulator

There are different design for the positron sources of future electron positron colliders [53]. As described in the introduction the undulator source has been chosen as the ILC baseline. The undulator baseline source will produce more positron flux than a conventional source. For example, the SLC positron flux is a factor of 60 less than the flux required in the ILC positron source, and the pulse intensity is a factor of 1500 less [31]. Moreover, in the conventional source there are limitations of thermal stress as explained in previous chapters. Another benefit of using the undulator baseline source is the possibility of producing polarised positrons.

In this section we will describe the helical undulator which is an important component of the ILC positron source baseline. The parameters of the ILC helical undulator from the ILC design report and constructed prototype are showing in 5.1 [3, 54].

TABLE 5.1: ILC helical undulator parameters [3, 54].

Parameters	Values
Undulator period	11.5 mm
Number of Periods	155
Magnetic field	0.88 T
Value of K	0.92
Average energy of photon	10.5 MeV
Total length	147 m
Photon beam power	131 kW
Electron beam energy	150 GeV
Electron current	9.0 mA

An electron beam with energy of 150 GeV will travel through the 147 m long helical undulator and has a period of 11.5 mm [3, 54]. The magnetic field strength of the undulator is $\approx$ 0.88 T on axis [54]. The beam of the electron will travel in a helical path along the undulator central axis. An intense gamma-ray beam will be

produced with $\approx 10\,\text{MeV}$ at the 1^{st} harmonic. The gamma-ray beam produced by the ILC helical undulator will have $\approx 131\,\text{kW}$ average power.

5.2 Helical Undulator Magnetic Field Map

In this section, I will investigate the magnetic field map of the helical undulator in three types of maps: ideal map, measured map, and simulated map.

5.2.1 Ideal magnetic field map

As stated in section 3.3.3, equations (5.1) and (5.2) describe the magnetic field inside an ideal helical undulator,

$$B_x = B_0 \sin \frac{2\pi z}{\lambda_u} \tag{5.1}$$

$$B_y = B_0 \cos \frac{2\pi z}{\lambda_u} \tag{5.2}$$

where B_0 is the field strength, z is the distance along the primary axis of the undulator, and λ_u is the period size. In HUSR/GSR software [55, 56] which will be discussed in more details in section 6.2, the electron is injected at an angle of $3.2 \times 10^{-6}\,\text{rad}$ in the y plane to ensure the electron exits the undulator on axis.

5.2.2 Measured magnetic field map

There were two field maps measured from the ILC prototype undulator modules using a Hall probe on-axis [54]. Imperfections in the magnet winding or deformation of the magnet 'former' lead to errors in the field. The measured field map

is tapered to ensure that the electron will stay on the centre of the undulator if injected along the centre.

5.2.3 Simulated magnetic field map

In order to produce a magnetic field map based on a measured field map. I introduced error in the magnetic field strength as well as in the period size over the length of the undulator along the z direction.

I added the errors shown in equations (5.3) and (5.4) to the value of the period size and well as to the field strength respectively in equations (5.1) and (5.2).

$$\sigma_\lambda(z) = \sum_{i=1}^{n} A_i \cos\frac{2\pi i z}{L} + \sum_{i=1}^{n} B_i \sin\frac{2\pi i z}{L}, \tag{5.3}$$

$$\sigma_B(z) = \sum_{i=1}^{n} C_i \cos\frac{2\pi i z}{L} + \sum_{i=1}^{n} D_i \sin\frac{2\pi i z}{L}. \tag{5.4}$$

I vary the n, which is the number of fourier component until we obtain good agreement with the measured data. A_i, B_i, C_i, and D_i are pseudo-random numbers, uniformly distributed between $(-ptop)$ where p is also varied to obtain a good agreement. The best agreement was found when $n = 200$, and $p = 7.14 \times 10^{-8}$. I used $\lambda_u + \sigma_\lambda(z)$ and $B_0 + \sigma_B(z)$ in equations (5.1) and (5.2) instead of λ_u and B_0 and we have new equations:

$$B_x = (B_0 + \sigma_B(z)) \sin\frac{2\pi z}{(\lambda_u + \sigma_\lambda(z))}, \tag{5.5}$$

$$B_y = (B_0 + \sigma_B(z)) \cos\frac{2\pi z}{(\lambda_u + \sigma_\lambda(z))}. \tag{5.6}$$

The model ensures the simulated map will not have a discontinuity. I compared the Discrete Fourier Transform of the x-projection of the magnetic field within the undulator for the measured data and simulated data to tune the model.

Fig. 5.1 shows a comparison between the Discrete Fourier Transform of the x-projection and y-projection of the measured field map and the simulated field map. The $\sigma_B(z)$ and $\sigma_\lambda(z)$ used in Eq. (5.5) are identical to the the $\sigma_B(z)$ and $\sigma_\lambda(z)$ used in Eq. (5.6) for both the x and y projections. From the peak which is around 155 periods, we can determine the period length to be 0.0115 m.

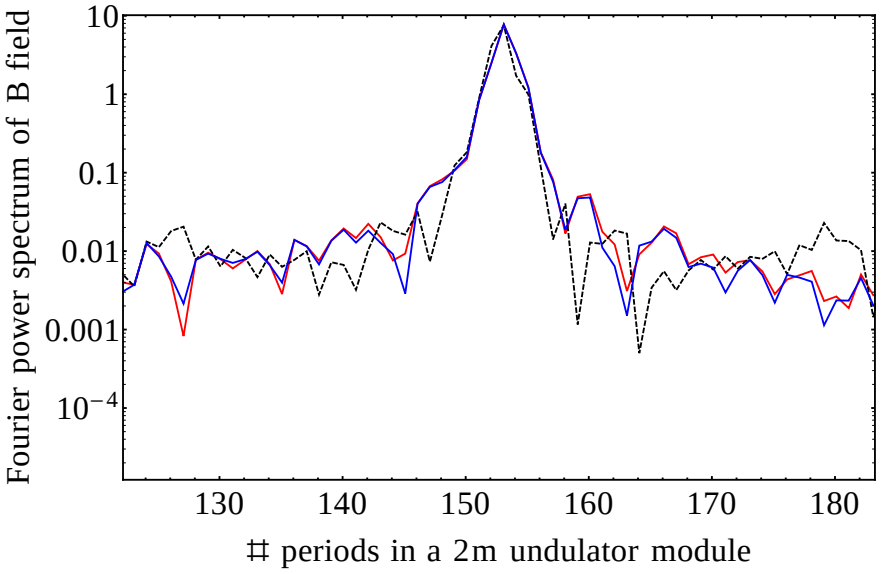

FIGURE 5.1: Discrete Fourier transform of the x-projection and y-projection of the magnetic field in the undulator. The measured map is shown by the red solid line for x-projection, blue solid line for y-projection, and the simulated field map is shown by the black dashed line.

5.3 Tracking the electron inside the Undulator

5.3.1 Ideal field map Tracking

In the ideal case, the electron will feel an average magnetic field strength of zero and will transported through the undulator with a total deflection of zero. For an electron injected on axis the movement of the electron will be helical according to Kincaid equation (2.49). Fig. 5.2 show the position of the electron on x and y axes. The average radius is 3.21907×10^{-6} m and the standard deviation is 8×10^{-12} m.

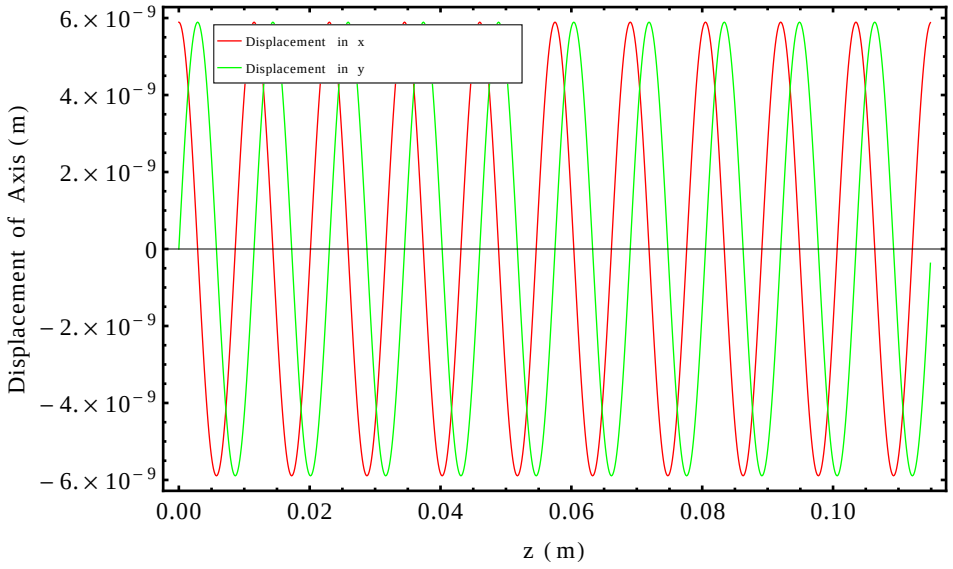

FIGURE 5.2: Displacement of a 150 GeV electron through 10 periods of the ILC Ideal helical undulator with a 0.88 T magnetic field strength.

5.3.2 Measured Field Map Tracking

In the measured field map case, the electron will be off axis due to the errors. Fig. 5.3 shows position of the electron in the x and y directions where the maximum deviation in x is -2.5×10^{-6} m and in y is -3.7×10^{-6} m. Fig. 5.4 shows the full three-dimensional trajectory of the electron inside the undulator.

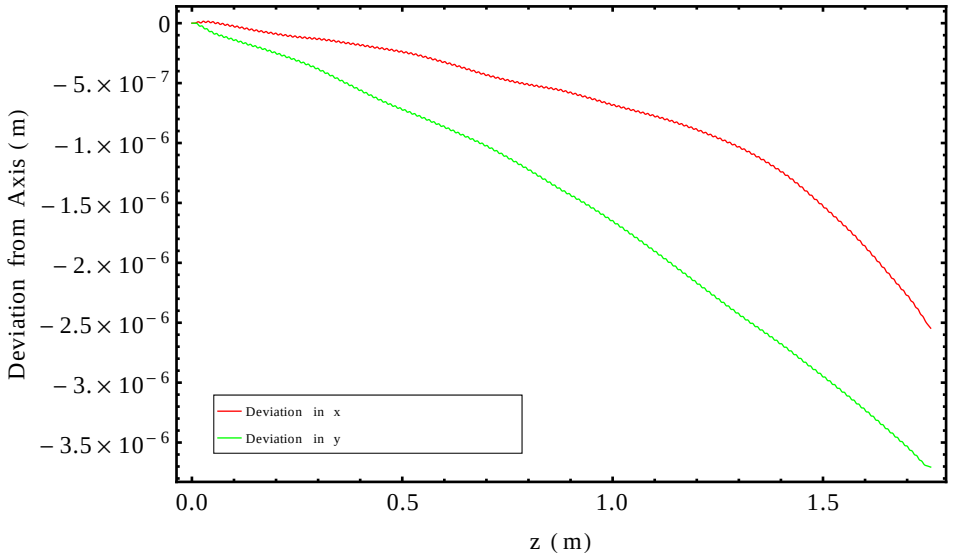

FIGURE 5.3: Deviation of a 150 GeV electron through a 1.7825 m long measured undulator and 0.88 T magnetic field strength. The electron is injected on axis and the measured field is manipulated to add tapering for the first 2 and last 2 periods.

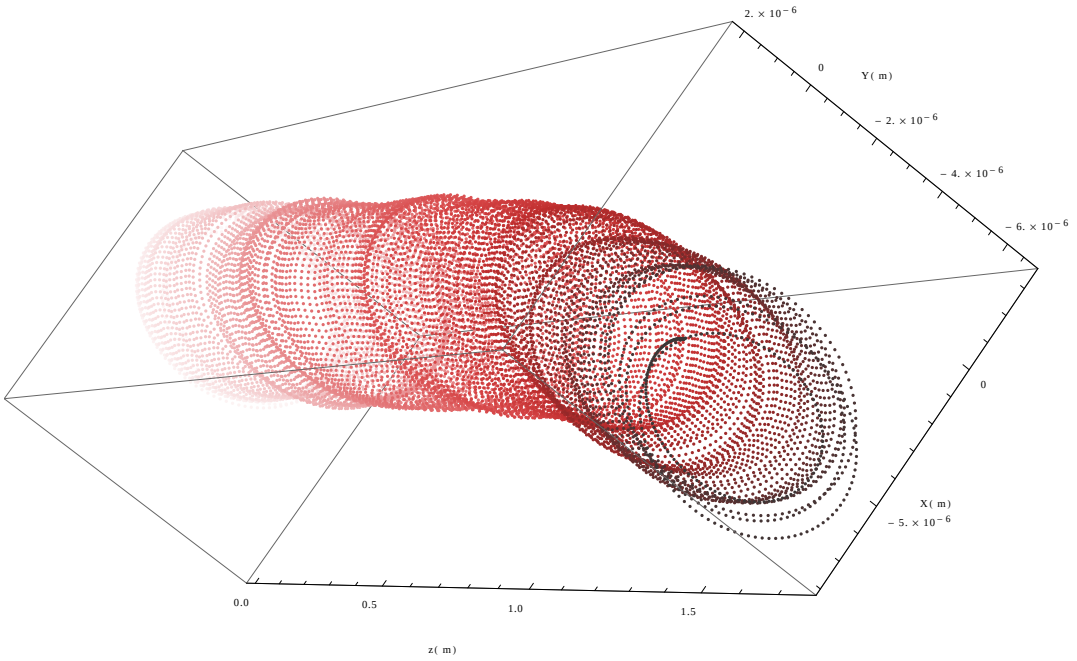

FIGURE 5.4: Trajectory of a 150 GeV electron through a 1.7825 m long measured undulator and 0.88 T magnetic field strength. The electron is injected on axis and the measured field is manipulated to add tapering for the first 2 and last 2 periods.

5.3.3 Simulated Field Map Tracking

In the simulated field map case, when we used equations (5.5) and (5.6) after introducing the optimized errors in magnetic strength and period the electron will experience similar errors to the types of error in the measured magnetic field map. Fig. 5.5 shows the position of the electron in the x and y directions where the maximum deviation in x is 7×10^{-7} m and in y is 1.9×10^{-6} m. Fig. 5.6 shows the full three-dimensional trajectory of the electron inside the undulator.

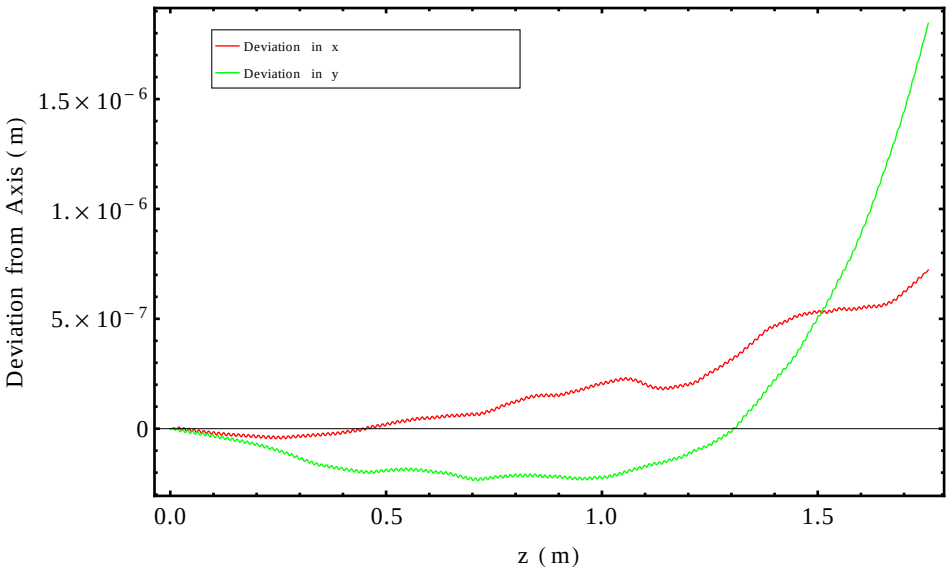

FIGURE 5.5: Deviation of a 150 GeV electron through a 1.7825 m long simulated undulator and 0.88 T magnetic field strength. The electron is injected on axis and the measured field is manipulated to add tapering for the first 2 and last 2 periods.

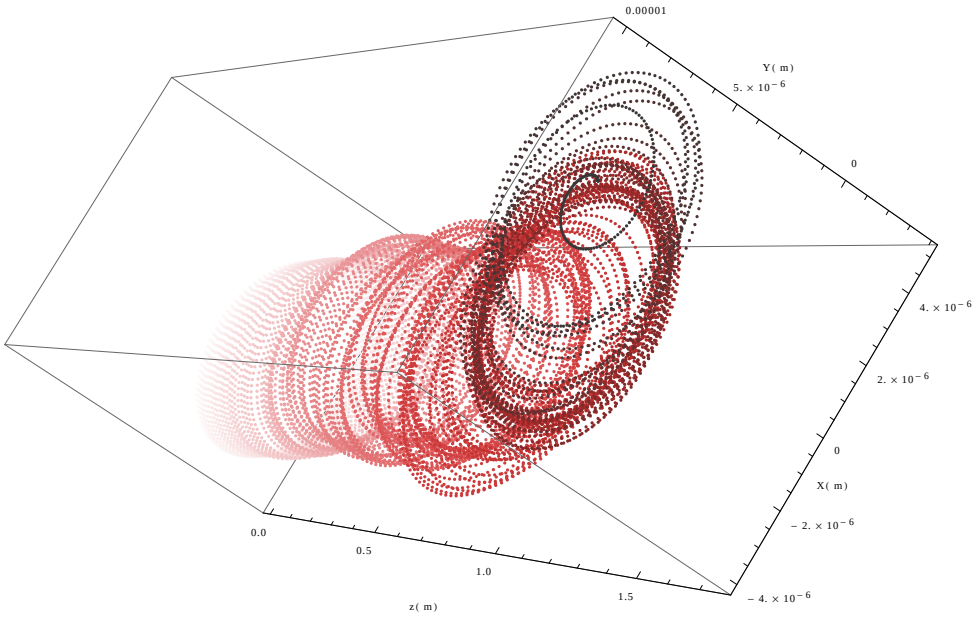

FIGURE 5.6: Trajectory of a 150 GeV electron through a 1.7825 m long simulated undulator and 0.88 T magnetic field strength. The electron is injected on axis and the measured field is manipulated to add tapering for the first 2 and last 2 periods.

To cover all possible trajectories of the electron inside the undulator, we simulated 20 different modules of undulator. The plot of all their position in the x direction is shown in Fig. 5.7, and Fig. 5.8 shows a band representing +/- 1 standard deviation in the x axis. Fig. 5.9 shows the position of all the 20 trajectories in the y direction and Fig. 5.10 shows the plot of a band representing +/- 1 standard deviation in y from the 20 trajectories.

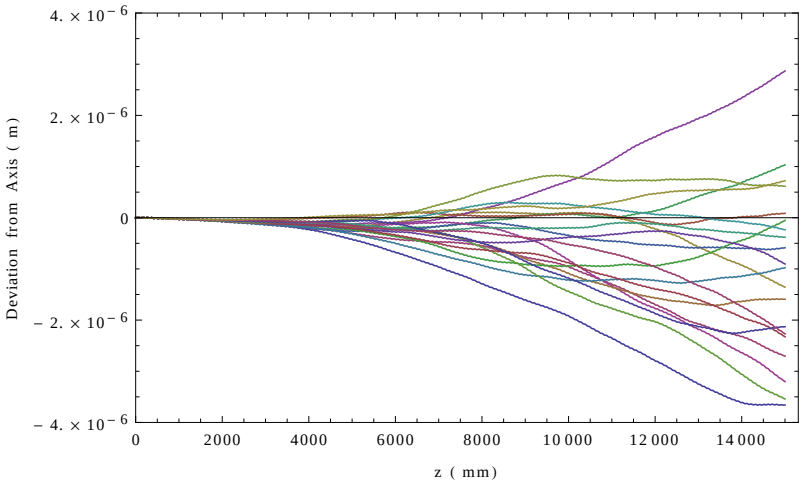

FIGURE 5.7: X trajectory of a 150 GeV electron through 20 different 1.7825 m long simulated undulators. Each color represents different random errors added to the simulated field map.

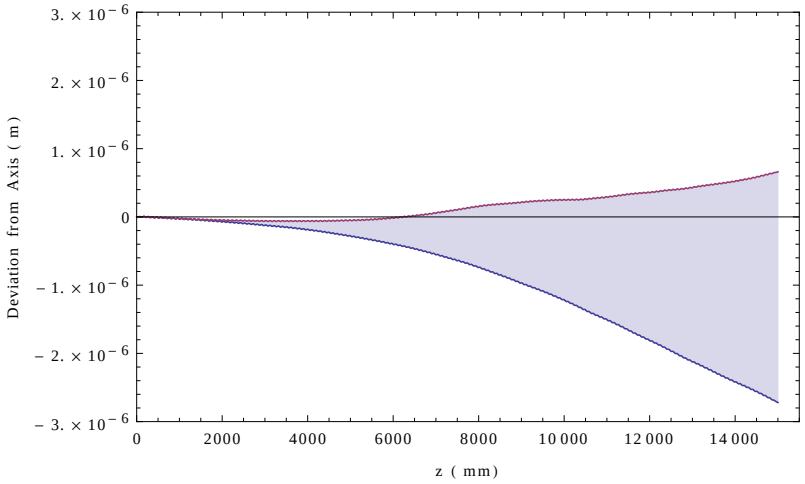

FIGURE 5.8: Figure showing the x trajectories of a 150 GeV electron travelling through a 1.7825 m long undulator module with a nominal magnetic field strength of 0.88 T. The band shows the average trajectory +/- 1 standard deviation as calculated from 20 simulated field maps.

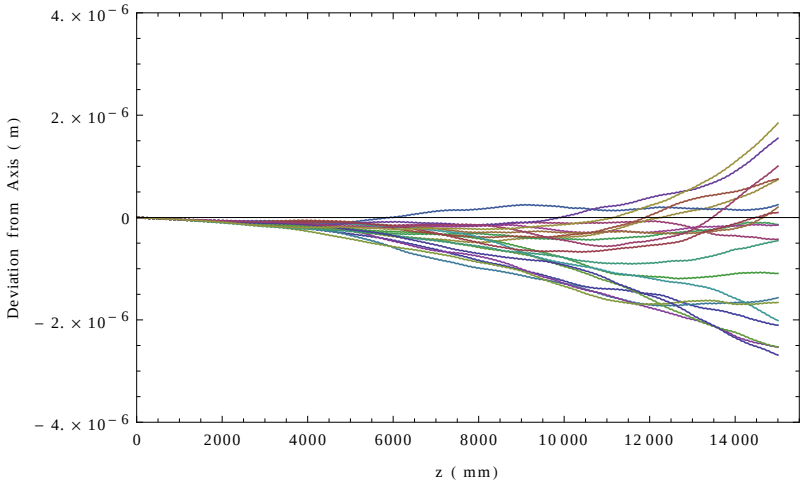

FIGURE 5.9: Y trajectory of a 150 GeV electron through 20 different 1.7825 m long simulated undulators. Each color represents different random errors added to the simulated field map.

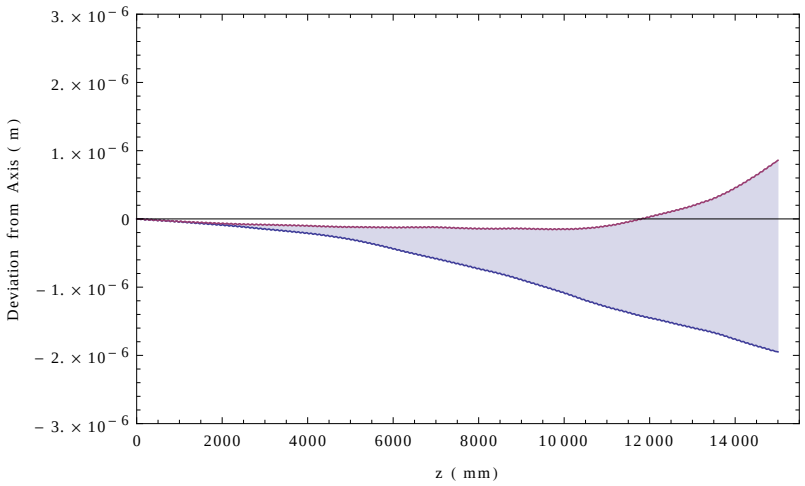

FIGURE 5.10: Figure showing the y trajectories of a 150 GeV electron travelling through a 1.7825 m long undulator module with a nominal magnetic field strength of 0.88 T. The band shows the average trajectory +/- 1 standard deviation as calculated from 20 simulated field maps.

The standard deviation in x at the end of a module is estimated to be 1.75×10^{-6} m. The standard deviation in y at the end of a module is estimated to be 1.5×10^{-6} m.

Next I introduced a new situation where $\sigma_B(z)$ and $\sigma_\lambda(z)$ used in Eq. (5.5) are not identical to the the $\sigma_B(z)$ and $\sigma_\lambda(z)$ used in Eq. (5.6) for both the x and y projections, which will be the worst scenario as the errors are not correlated. The modules have same values of $n = 200$, and $p = 7.14 \times 10^{-8}$ but different random number sequences. Fig. 5.11 shows a comparison between the Discrete Fourier Transform of the x-projection of the measured field map and the simulated field map. Fig. 5.12 shows a comparison between the Discrete Fourier Transform of the y-projection of the measured field map and the simulated field map.

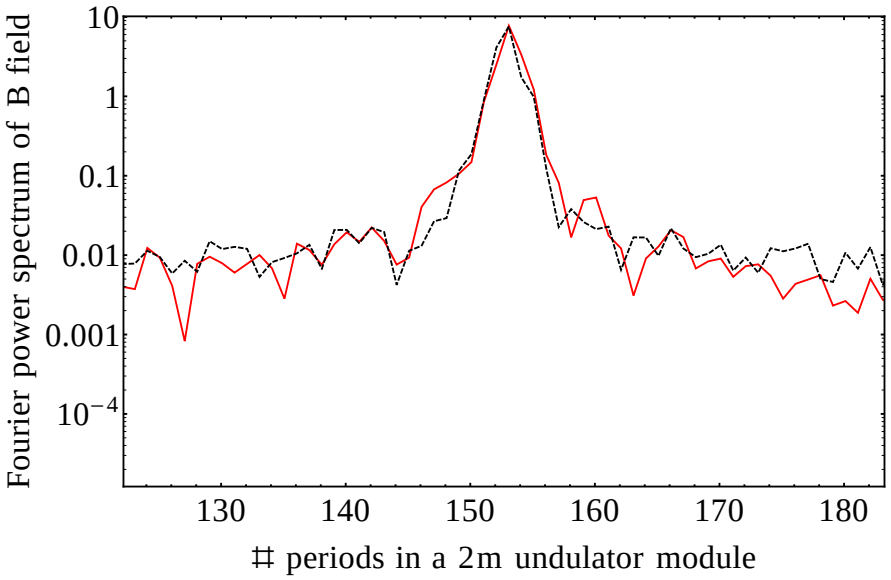

FIGURE 5.11: Discrete Fourier transform of the x-projection of the magnetic field in the undulator. The measured map is shown by the red solid line, and the simulated field map is shown by black dashed line.

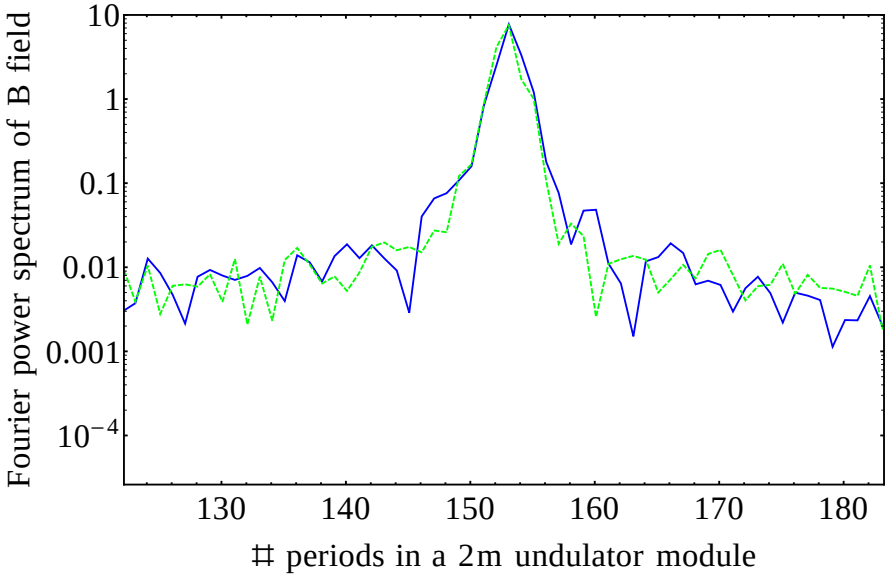

FIGURE 5.12: Discrete Fourier transform of the y-projection of the magnetic field in the undulator. The measured map is shown by the blue solid line, and the simulated field map is shown by green dashed line.

Fig. 5.13 show position of the electron in the x and y directions. Fig. 5.14 show the full three-dimensional trajectory of the electron inside the undulator.

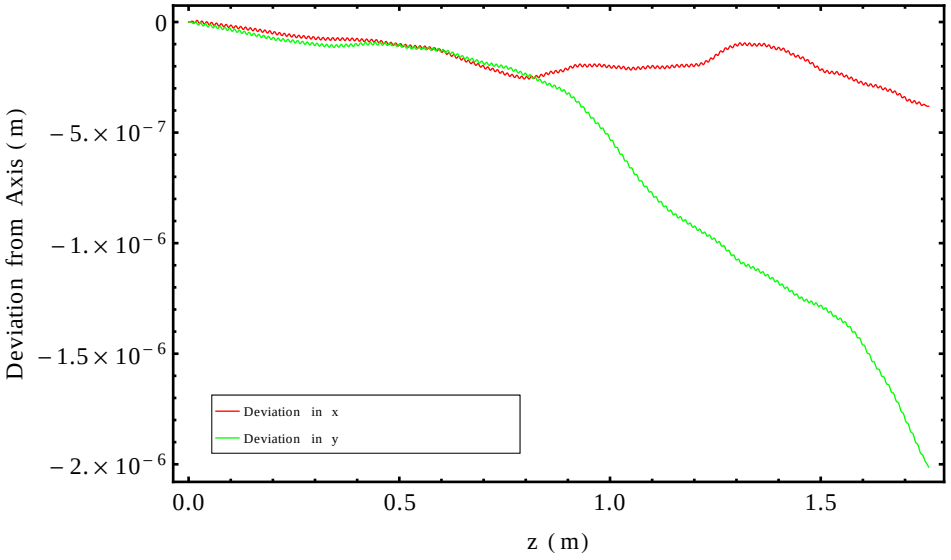

FIGURE 5.13: Deviation of a 150 GeV electron through a 1.7825 m long simulated undulator and 0.88 T magnetic field strength. The electron is injected on axis and the measured field is manipulated to add tapering for the first 2 and last 2 periods.

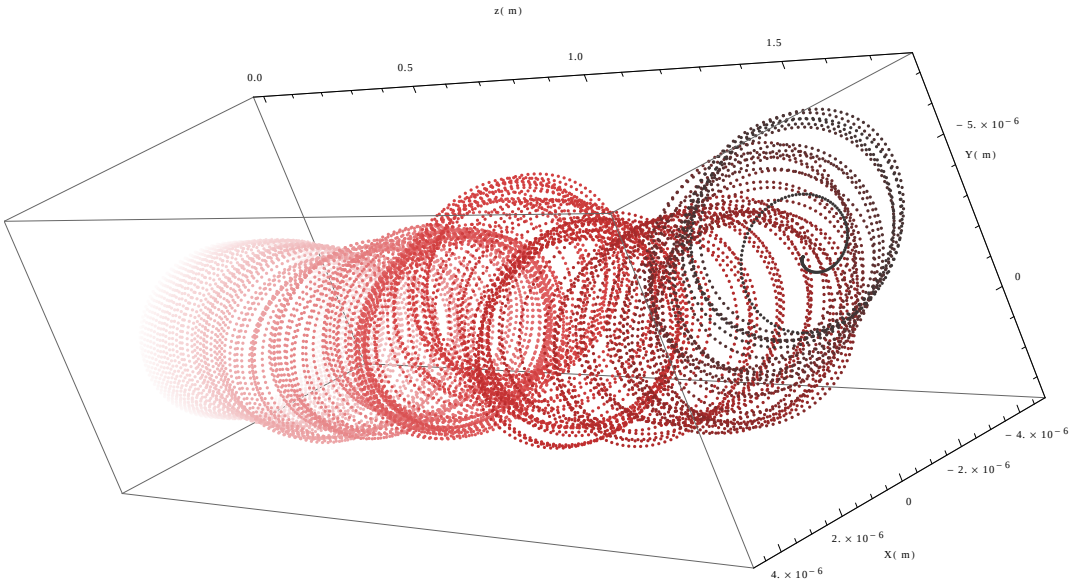

FIGURE 5.14: Trajectory of a 150 GeV electron through a 1.7825 m long simulated undulator and 0.88 T magnetic field strength. The electron is injected on axis and the measured field is manipulated to add tapering for the first 2 and last 2 periods.

In this case, where $\sigma_B(z)$ and $\sigma_\lambda(z)$ used in Eq. (5.5) are not identical to the the $\sigma_B(z)$ and $\sigma_\lambda(z)$ used in Eq. (5.6) for both the x and y projections, the deviation of the electron is still in the acceptable range and is consistent with the previous trajectories. Therefore, the effect can be neglected in these simulations.

5.3.4 Realistic Beam Spot Size and Divergence

In this section, I simulate tracking a beam with a realistic beam size. To simulate the beam spread I generated pseudo-random initial position and divergences in x and y using a Gaussian distribution with a standard deviation given by the values: $\sigma_x = 3.7 \times 10^{-5}$ m, $\sigma_y = 2.4 \times 10^{-6}$ m, $\sigma_{x'} = 0.9 \times 10^{-6}$ rad and $\sigma_{y'} = 0.06 \times 10^{-6}$ rad [57]. I used tapering in both, the ideal and measured field maps. I used 5 different sets of initial coordinates to get an indication of the size of this effect.

In the case of the ideal field map, the standard deviation due to including a realistic beam distribution in x at the end of a module is estimated to be 2.9×10^{-5} m and 2.8×10^{-6} m in y which is consistent with the starting beam spot size. In addition, the standard deviation in x at the end of a module is estimated to be 2.6×10^{-5} m and 3×10^{-6} m in y for the measured field map case which is consistent with the starting beam spot size.

5.4 Conclusion

In this chapter, I have discussed the possible types of undulator magnetic field as well as the trajectories of the electron beam inside them. Specifically, there are concerns about the errors in the magnetic field and how these can affect the transportation of an electron beam through the undulator. Errors in the magnetic field cause the electron trajectory to be off-axis and in an extreme case the beam could be lost.

To deal with these concerns, we simulated the trajectory of the electron beam inside the measured magnetic field of the ILC helical undulator prototype and developed a software tool using Mathematica to generate a magnetic field map based on the error from any measured field map.

Based on these simulations, the trajectory of the electron inside the measured field and simulated maps will have maximum deviations from axis of the order of tens of microns. Since the deflection of the beam size is less than the real beam spot size, this deflection should be controllable. There was a good agreement between the simulated field maps with errors and measured field map in terms of the calculated electron trajectory. The maximum spread in x at the end of the simulated modules is 6.7×10^{-6} m, and in y is 5×10^{-6} m. The standard deviation at the end of simulated modules is estimated to be 1.75×10^{-6} m in x and 1.5×10^{-6} m in y.

In addition, I investigated the worst-case scenario when the errors in the magnetic field in x and y are not correlated. I found that the trajectory did not change much and the effect is negligible. Moreover, I injected the particles randomly in different angles and positions using the real parameters of the beam size to study the effect on the trajectory of the beam. For the ideal field map case, the standard deviation in x at the end of a module is estimated to be 2.9×10^{-5} m and 2.8×10^{-6} m in y which is consistent with the starting beam spot size. In the case of the measured field map, the standard deviation in x at the end of a module is estimated to be 2.6×10^{-5} m and 3×10^{-6} m in y which is consistent with the starting beam spot size.

Carrying out prototype experiments to evaluate the trajectory of the electron and spectrum is very expensive. By evaluating the trajectory of the electron and spectrum using a numerical code with a high accuracy and realistic simulated data I hope to turn this initial study into a rigorous investigation [58]. The spectra from

ideal, measured, and simulated field maps will be presented in the next Chapter and will be discussed in more detail.

Chapter 6

Gamma-rays Studies at Future Intense Positron Sources

6.1 Introduction

Gamma rays sources such as HIγS [12] and ELI-NP [59] are used to investigate different research topics such as nuclear physics. The baseline design of the ILC positron source requires the production of an intense flux of gamma rays, but only 7% [28] or less of these gamma rays will be used to produce positrons, and the rest will pass to the photon beam dump.

Modern gamma ray facilities try to obtain a high photon flux with a narrow energy bandwidth, and the ILC baseline design already has a much higher flux of 7.8×10^{16} photon/s but the bandwidth is broad as the spectrum contains many harmonics. To match the dedicated gamma ray facilities in terms of bandwidth, I developed two techniques to optimize the bandwidth by designing a collimator aperture for a collimator that would appear downstream of the positron production target. Simulations for an idealised undulator show that the beam could exceed the current flux produced from HIγS (Duke University) [60, 61] by several orders

of magnitude reaching 10^{13} photon/second with a bandwidth of 5% where the bandwidth of HIγS is in a range of 4% to 10%.

Moreover, I used the HUSR/GSR [55, 56] described in section 6.2 to investigate the gamma-ray energy spectrum coming from simulated and measured helical undulator magnetic fields with errors as described in the previous chapter.

The study of the energy spectrum from the undulator is a very important characteristic in my case as I am trying to use this beam for additional applications, for example, nuclear physics applications. However, it is not critical for positron production as only the flux is needed for the positron production. Therefore, I can make some changes to the spectrum whose effects are fairly small as shown from previous studies where the number of captured positrons does depend on high energy gamma rays in the higher harmonics [62, 63].

6.2 HUSR/GSR Software

The HUSR/GSR software packages were originally developed at the Cockcroft Institute of accelerator science and technology by David Newton [55, 56] to calculate the synchrotron radiation output from a helical undulator as included in the ILC baseline design but GSR can be applied to a much wider range of magnets. The code tracks particles trajectories inside the undulator system using Lie maps, which are produced by numerically integrating the Hamiltonian of an electron in the magnetic field [64, 56]. Each Lie map represents a small step in the undulator period i.e. a Lie map is a transfer map where each map will give the new coordinates of a particle in phase space. In this thesis each Lie map used 10^6 integration steps. This allows us to track particles inside any magnet system with high accuracy. In HUSR/GSR software after tracking the electron(s), we set observation points at the end of the undulator. HUSR/GSR calculates the retarded

potential from the electron(s). Then, from the retarded potential it calculates the electric field at each observation point as a function of time. Finally, the frequency spectrum of the observed radiation is obtained by Fourier transforming the field.

The HUSR/GSR software gives us the ability of including errors in the undulator magnetic field as well as tapering as shown in Fig. 6.1. Tapering the field is important to ensure that the electron beam will be injected in the centre of the undulator. The accuracy of HUSR/GSR software has been tested by comparing the results of the energy spectra of HUSR/GSR to the energy spectra of the Kincaid equation (2.49) [42], and the result is shown in Fig. 6.2 where they agree at the level of 1%. Simulations of the ideal helical undulator were calculated using 100 equal sampling steps along the trajectory using the Lie map, and the radiation spectrum was calculated in 1000 energy bins of equal size over the range 0.2 MeV to 200 MeV. The beam was injected on axis at an angle which ensured that the beam exits the undulator on axis and there is no tapering in the ideal field map in this case. However, both ways are equivalent and ensure that the beam will travel along the central axis of the undulator.

In the ideal case, the Lie map for one period was generated and then used 155 times to give the total length of the undulator. In the realistic case, which will be used in my investigations later in this chapter, I increased the steps in the Lie Map to 15000 steps to obtain higher accuracy, as well as increasing the observation points. The increase in sampling points and observation points was needed because in a real undulator each period is different than the other in terms of the magnetic strength and the length.

Fig. 6.3 shows the accuracy for tracking of the electron through the ideal helical undulator using 10, 100, and 1000 steps along the trajectory.

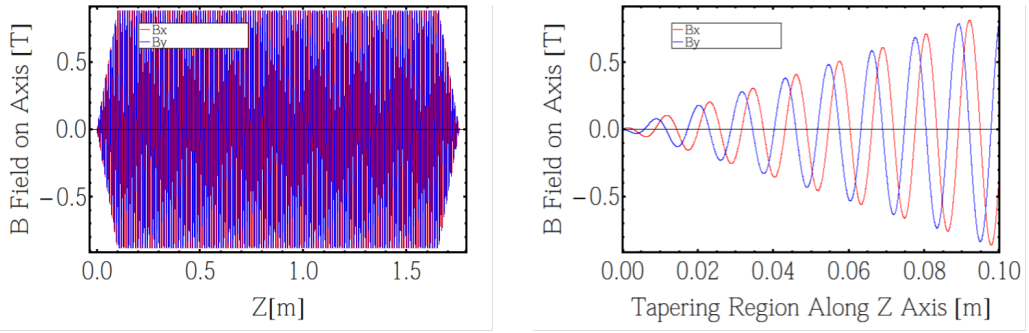

FIGURE 6.1: Ideal magnetic field of the helical undulator for the ILC baseline parameters, left shows the whole undulator field, and right shows the tapering region at the start of the undulator.

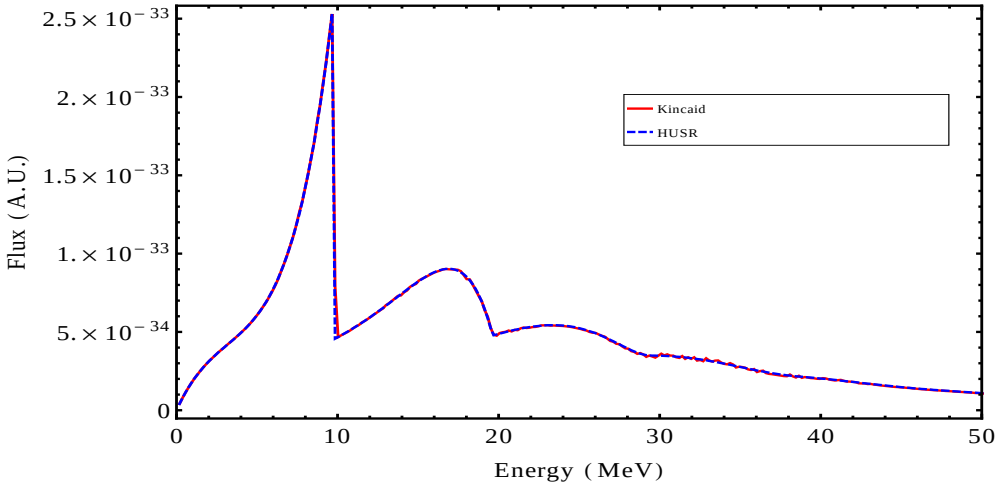

FIGURE 6.2: Bench marking HUSR/GSR energy spectra with Kincaid energy spectra.

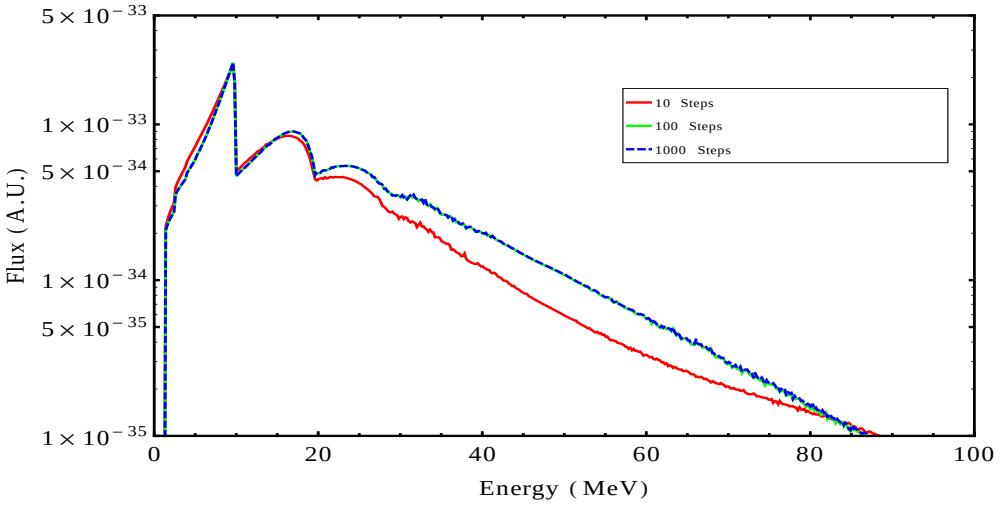

FIGURE 6.3: Calculated energy spectrum from tracking a single electron through an ideal helical undulator for three cases, tracking the electron at 10 (red), 100 (green) and 1000 (dashed blue) steps along the trajectory. When only 10 steps are used along the trajectory the energy spectrum is clearly inaccurate after the first harmonic peak.

6.2.1 HUSR/GSR Observation Points

The default positions of HUSR/GSR software observation points are shown in Fig. 6.4 for low resolution. It possible to increase the points to have a higher resolution. The black points are the actual points at which the electric field is calculated, when HUSR/GSR calculates the total flux. Each point represents a ring of equal area as shown in the diagram. This technique is accurate as long as the photon flux is produced azimuthally symmetrically.

I tested the accuracy of this method to obtain the highest accuracy for the ideal case. Fig. 6.5 show the total flux as a function of the number of observation points. We can see that the calculated flux saturates after 3000 points and the total flux was 1.285×10^{-31} photon/s. Also, I tested the code for a full square aperture where each sampling point represents square on a square grid, and increased the points

until the calculated flux saturates after 9000 points and the total flux was 1.291×10^{-31} photon/s. Both of these analyses were done for the ideal case, and there is a small difference in the total flux between the two methods $\approx 0.006 \times 10^{-31}$, which is probably due to the extra area which is covered by the square aperture.

However, the assumption of azimuthal symmetry does not hold when I use the realistic magnetic field. The result of simulating the spectrum from a realistic (measured) magnetic field is shown in Fig. 6.7. From Fig. 6.7, we can see clearly, that the photon distribution is not symmetric, therefore, I have used the the full square aperture with 10000 points for all the remaining simulations presented in this chapter.

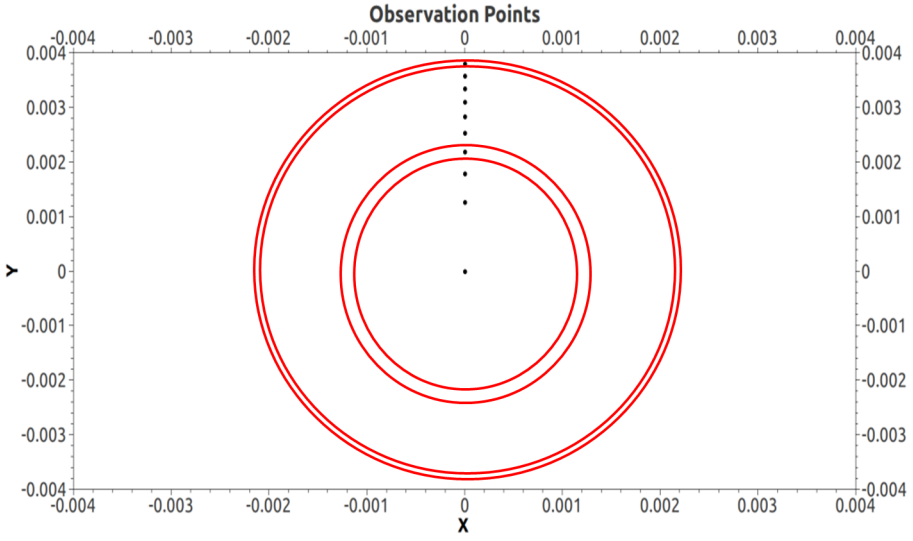

FIGURE 6.4: The deflate positions of the HUSR/GSR software set up for the observation points (low resolution).

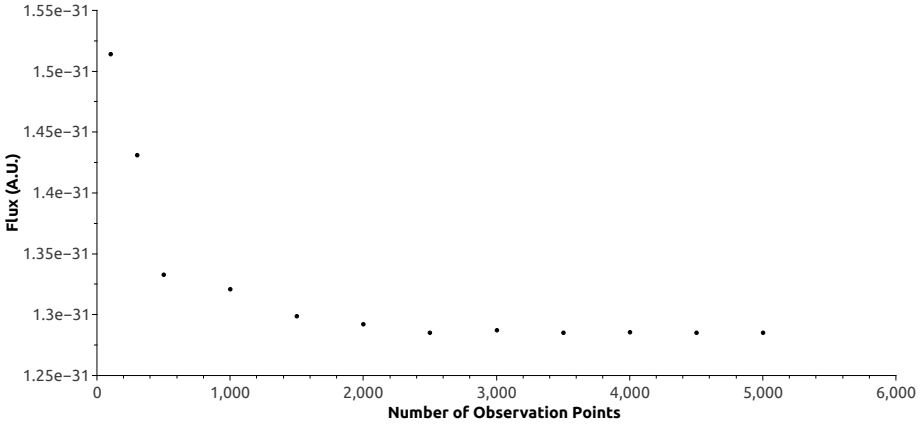

FIGURE 6.5: The total number of photons per second as a function of the number of observation points for the default observation set-up of HUSR/GSR software.

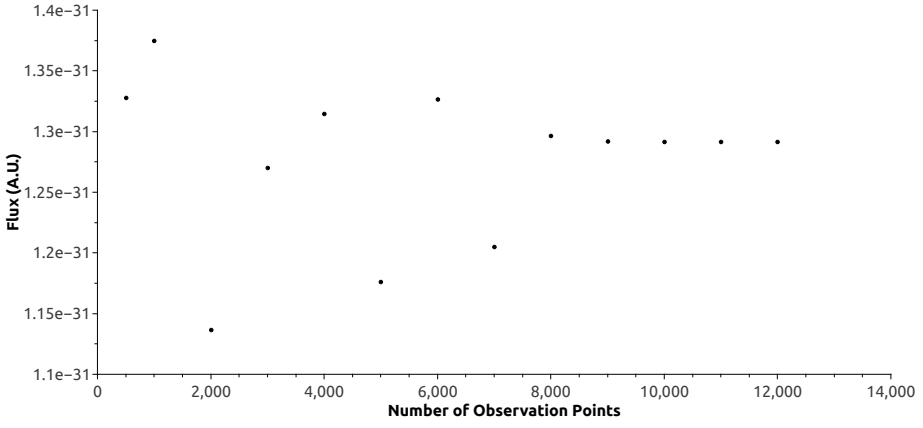

FIGURE 6.6: The total number of photon per second as a function of the number of observation points for the full square aperture arrangement of observation points from HUSR/GSR.

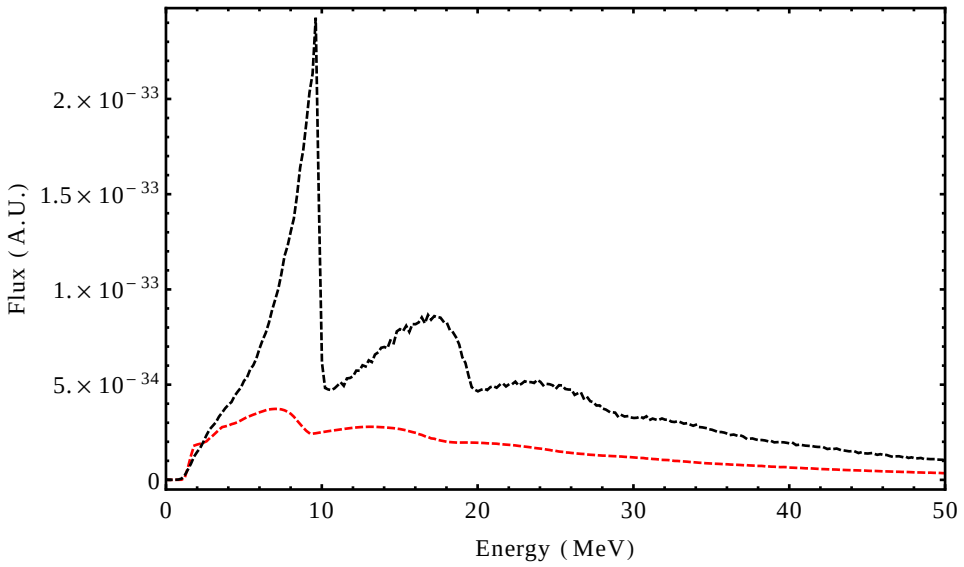

FIGURE 6.7: The calculated energy spectra from a realistic magnetic field map, in dashed red when using the default HUSR/GSR observation point positions, and in black dashed line when using the full square aperture.

6.2.2 Additional Features to HUSR/GSR Observation Points

Following on from previous work [63] I have extended the observation point algorithm as shown in Fig. 6.8. For this new feature each point represents a segment. This segmented pattern will give more accurate results from photon distributions which are not azimuthally symmetric. The number of points in the radial and azimuthal directions can be configured.

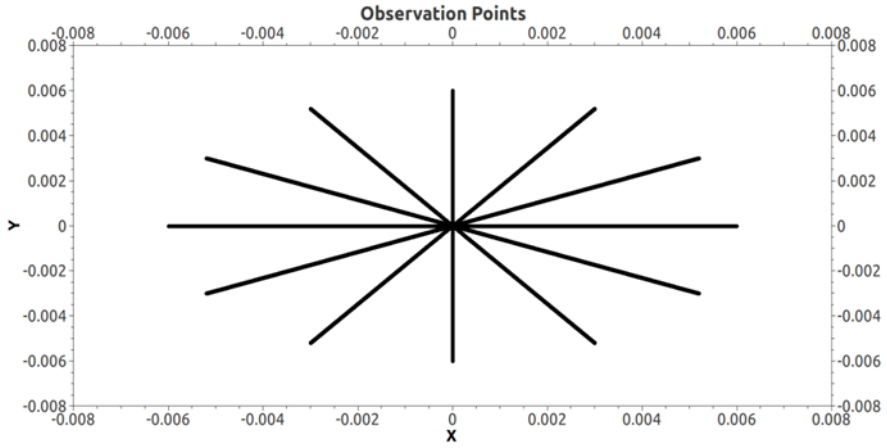

FIGURE 6.8: The new feature included to HUSR/GSR for setting up observation points and each point represent a segment.

In addition it is possible to simulate an annular aperture using the same idea as above but excluding a central circular region.

6.3 Spectra from Measured and Simulated Magnetic Field Map

In this section, we will calculate the energy spectrum from the three types of undulators, which were discussed in more detail in chapter 5. Fig. 6.9 shows the output of the energy spectrum from an ideal undulator system and the measured undulator system as previously described in chapter 5. Table 6.1 show a summary of the important differences between the energy spectrum from the ideal field map and the energy spectrum from the measured field map. I have used the parameters of the magnet system shown in table 5.1 to evaluate the spectra. These parameters were used in my calculations for the simulated model as well.

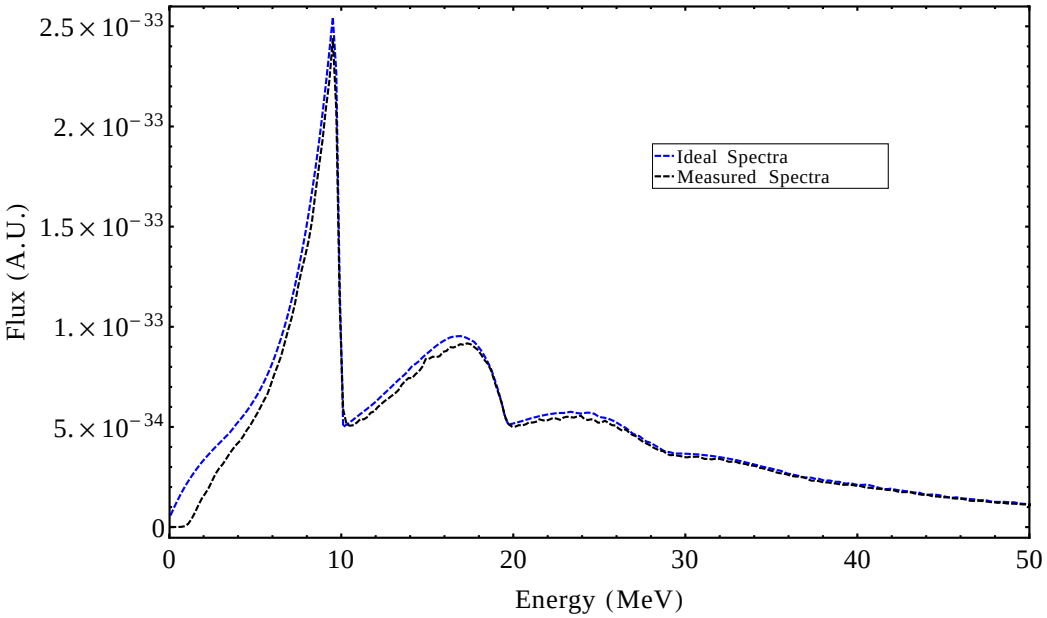

FIGURE 6.9: Calculated energy spectrum from tracking a single electron through a 1.7825 m long undulator with a circular aperture with a radius of 0.0045 m at a distance of 500 m from the end of the undulator. The blue dashed line shows the result from an ideal map, and the black dashed line shows the result from the measured map.

TABLE 6.1: Summarized table of important difference between the measured and ideal energy spectrum

Parameters	**Average peak height** ($1^{st} harmonic$) (A.U.)	**Average total flux**
Ideal (no beam spot)	2.532×10^{-33}	$7.775 \times 10^{16}\,\gamma/s$
Measured (no beam spot)	2.486×10^{-33}	$7.011 \times 10^{16}\,\gamma/s$

From table 6.1, we can clearly see that the total flux has reduced by $\approx 9\%$ overall but only by $\approx 2\%$ on the first harmonic. These reductions are due to the errors in the measured field map.

I used the simulated field map in the HUSR/GSR software to investigate the output spectra and compare the results to the results from the measured field

map. Fig. 6.10 shows the photon energy spectra from the measured model and the energy spectra from one representative example of the 20 simulated field map.

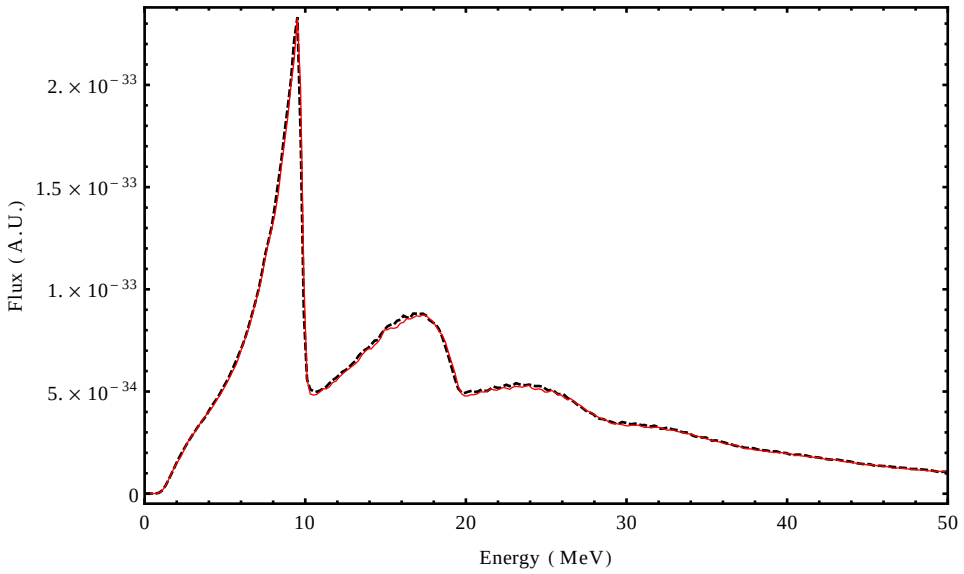

FIGURE 6.10: Energy spectrum calculated from the undulator magnet field map. The energy spectrum from a simulated map is shown by the red solid line, and the energy spectrum from the measured field map is shown by the black dashed line.

As we can see there is a very good agreement between the two spectra at a level of 2%. Based on this result, I simulated 20 models to produce a range of 'realistic' spectra. Fig. 6.11 shows the average photon energy spectra with a band representing +/- 1 standard deviation obtained from the 20 models from our simulated field maps. This gives an estimate of the range of the deviation of the spectra which is at a level of 3% compared to the ideal spectrum.

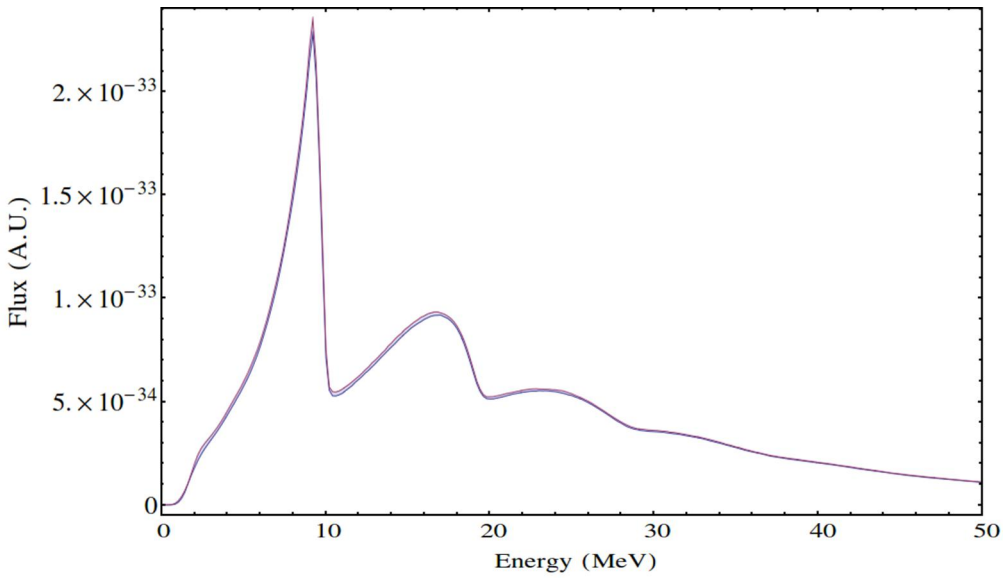

FIGURE 6.11: Energy spectrum calculated from the magnet field map. The red line represents the maximum deviation and the blue line represents the minimum deviation.

As in chapter 5, I consider the case where the errors in x and y in the simulated model are uncorrelated. Fig. 6.12 shows a comparison between the the spectrum from the measured field map and spectrum from the simulated field map.

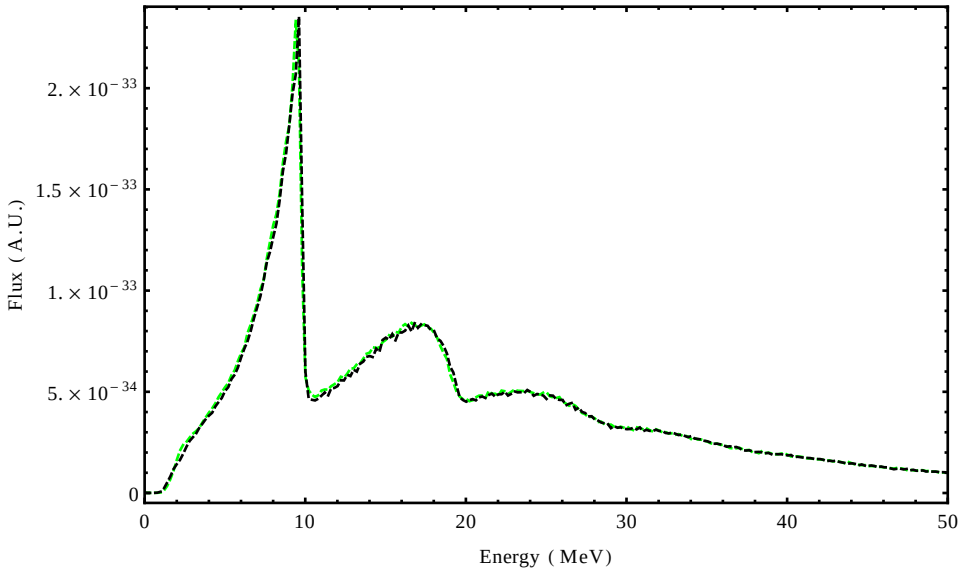

FIGURE 6.12: Energy spectrum calculated from the magnet field map. The energy spectrum from the simulated map is shown by the green solid line, and the energy spectrum from the measured field map is shown by the black dashed line.

6.3.1 Realistic Beam Spot Size and Divergence

Here I calculated the spectrum from injection of the particles with realistic beam spot size and divergence. For the ideal map, Fig. 6.13 shows a band representing +/- 1 standard deviation of the spectrum from 5 particles injected at random positions in phase space into the ideal field map.

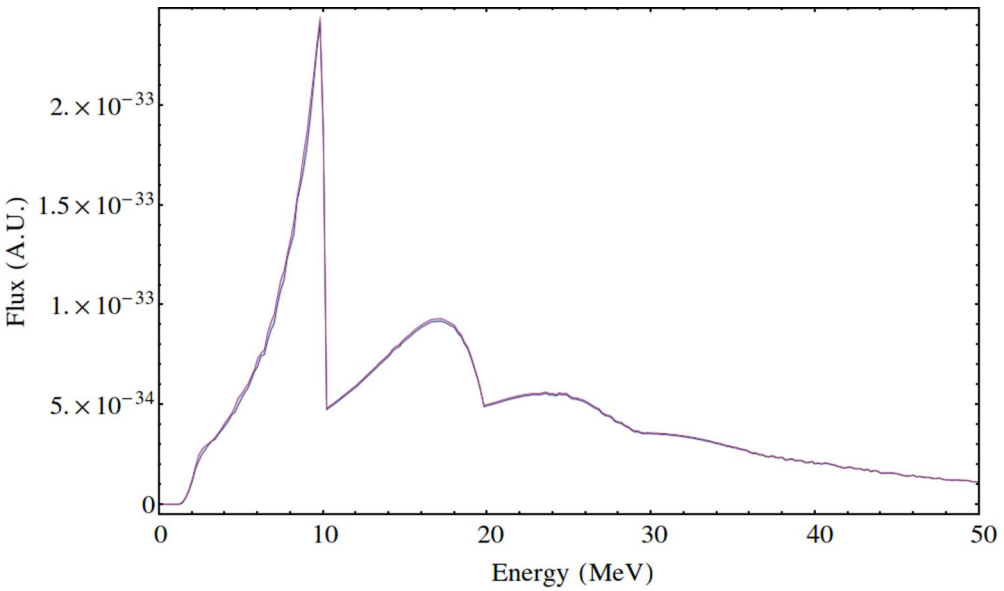

FIGURE 6.13: Energy spectrum calculated from the ideal field map. The red line represents the maximum deviation and the blue line represents the minimum deviation.

For the measured map, Fig. 6.14 shows a band representing +/- 1 standard deviation of the spectrum from 5 particles injected at random positions in phase space into the measured field map.

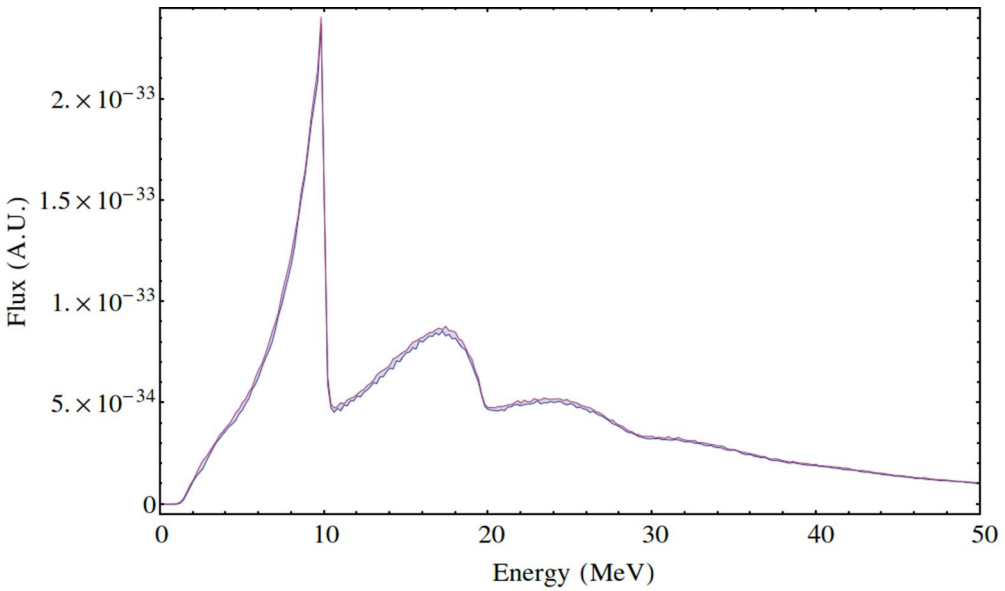

FIGURE 6.14: Energy spectrum calculated from the measured field map. The red line represents the maximum deviation and the blue line represents the minimum deviation.

Table 6.2 show a summary of the important differences between the energy spectrum from the ideal field map using a realistic beam spot size shown in Fig. 6.13 and the energy spectrum from the 20 simulated field maps injected on axis shown in Fig. 6.11.

TABLE 6.2: Summarized table of important difference between the ideal energy spectrum using a realistic beam spot size and the energy spectrum from the 20 simulated field maps injected on axis.

Parameters	**Average peak height** ($1^{st} harmonic$) (A.U.)	**Average total flux**
Ideal (with beam spot)	2.426×10^{-33}	$7.281 \times 10^{16}\,\gamma/s$
Simulated (no beam spot)	2.317×10^{-33}	$7.085 \times 10^{16}\,\gamma/s$

By comparing these values to the ideal spectrum with no beam spot, I found a reduction by $\approx 4\%$ of the peak height on the first harmonic and by $\approx 6\%$ for the total flux in the case of the ideal field map. By comparison there is a reduction

by ≈ 8% of the peak height on the first harmonic and by ≈ 9% for the total flux in the case of the simulated field map.

Table 6.3 show a summary of the important differences between the energy spectrum from the ideal field map shown in Fig. 6.13 and the energy spectrum from the measured field map shown in Fig. 6.14 using a realistic beam spot size in both cases.

TABLE 6.3: Summarized table of important difference between the measured and ideal energy spectrum using a realistic beam spot size.

Parameters	**Average peak height** ($1^{st} harmonic$) (A.U.)	**Average total flux**
Ideal (with beam spot)	2.426×10^{-33}	$7.281 \times 10^{16}\,\gamma/s$
Measured (with beam spot)	2.381×10^{-33}	$6.929 \times 10^{16}\,\gamma/s$

By comparing these values to the ideal spectrum with no beam spot as before, I found a reduction by ≈ 4% of the average peak height on the first harmonic and by ≈ 6% for the average total flux in the case of the ideal field map. By comparison there is a reduction by ≈ 6% of the average peak height on the first harmonic and by ≈ 11% for the average total flux in the case of the measured field map. Overall, the injection of the particles with realistic beam spot size has smaller effects than the errors in the magnetic field on the energy spectrum and the total flux.

Previous studies of earlier designs of the ILC undulator [62, 63] showed that the number of positrons captured and injected into the positron damping ring strongly varies depending upon which harmonic of the undulator spectrum is being considered. For example, the first harmonic contributes only 7% of the total positron yield, whereas the second, third and fourth each contribute around 18%. Using this data along with the modified energy spectra from this work suggests a drop in positron yield of ∼ 7% compared to the ideal case.

6.4 Possible Use of the ILC Gamma-ray In Additional Applications

As mentioned earlier in this chapter, only 7% or less of the gamma rays beam for the ILC positron source will be used to produce the positrons. Therefore, we could consider introducing a small secondary facility as shown in Fig. 6.15. This small facility can be placed in the region of the photon beam dump of the current baseline design for the ILC positron source to utilise the otherwise wasted photons for additional applications, e.g nuclear physics or a facility for testing particle detectors using gamma ray.

To utilize this beam, there are different applications for the high intensity gamma-ray beam from different scientific fields such as nuclear physics or industrial applications [65]. One of the most important fields is nuclear physics and they required narrow bandwidth energy spectrum to carry out their experiment such as Nuclear Resonance Fluorescence (NRF) technique [66]. However, even if the spectrum at the ILC cannot be made to be very narrow by collimation the gamma-ray beam could still be an important facility to be used for additional applications rather than the production of positrons only; as there are different useful gamma-ray facilities around the world which still have a very large bandwidth such as the bremsstrahlung spectrum of the Stuttgart Dynamitron [67]. Fig. 6.16 shows the high-energy gamma-ray beam sources ($\approx$ 10 MeV) around the world with the improvement of their energy bandwidth over the years [68]. As a result of this investigation two general techniques were developed to obtain a useful energy spectrum from the ILC spectrum by defining a collimator aperture. More details of these two techniques will follow in the next section.

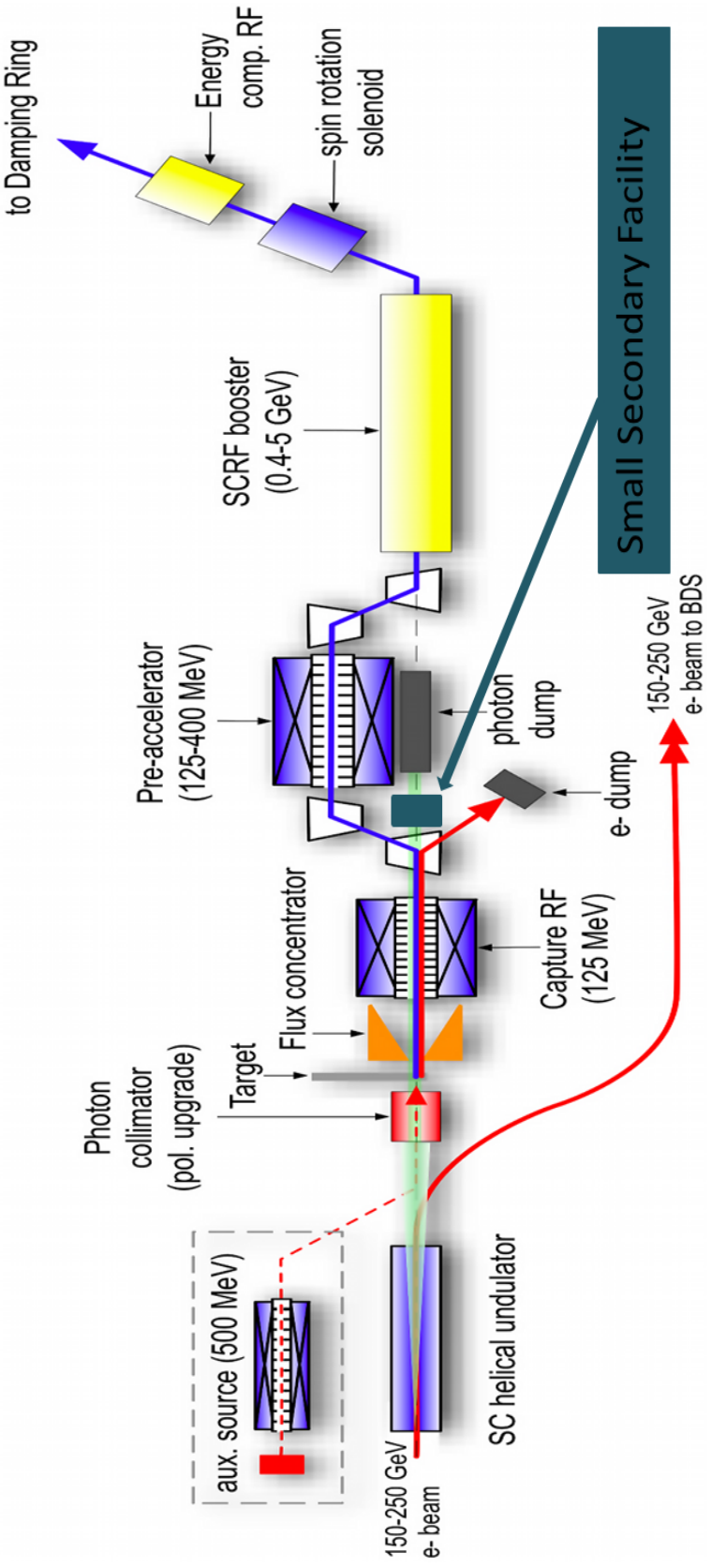

FIGURE 6.15: Planned design for ILC positron source with the secondary experiment facility.

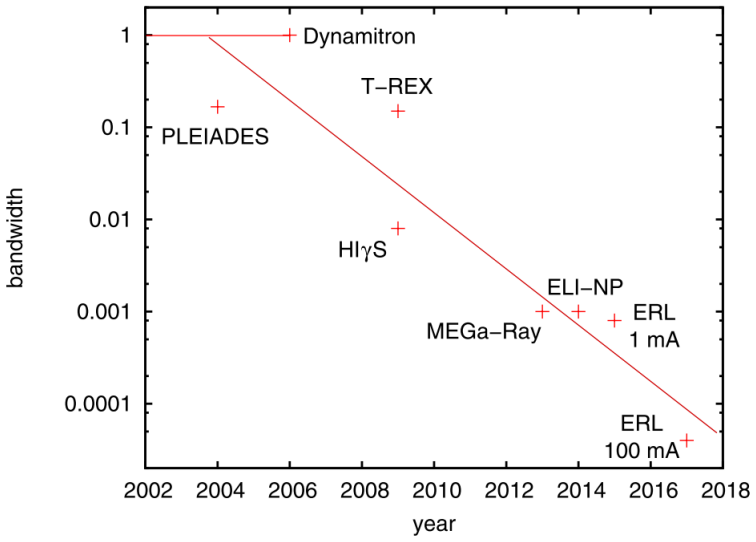

FIGURE 6.16: High-energy gamma-ray beam source (≈ 10 MeV) around the world with the improvement of their energy bandwidth over the years. This figure was reproduced from [68].

Possible additional applications for the ILC gamma-ray beam could include:

Industrial Applications Using the ILC gamma-ray in industrial applications such as to treat and manage nuclear waste [69].

Instrumentation A gamma-ray beam with this high flux can be used as a testing facility to test detectors, dosimeters, gamma-ray lenses, etc [65].

Nuclear Physics Photon induced particle emission at high energy can provide important details of the collective Giant Dipole Resonance (GDR) structure and damping [65].

Medical Isotopes Production Gamma-ray can be used to produce radioisotopes for nuclear medical applications through e.g photonuclear reactions or photoexcitation reactions. The beam does not need to be narrow to produce useful isotopes [70], but a beam with a high flux and narrow energy bandwidth could open the door to produce new isotopes [71].

Second Production Target A recent study showed that in principle this beam could be used to produce more positrons to increase the total positrons flux [72]. I could propose using this gamma-ray beam to strike on additional target to produce positrons for different applications e.g positron-positron colliders.

6.5 Obtaining the Required Energy Spectra From the Undulator System

In this section I discuss two techniques to help to automatically detect the positions of the observation points which give spectra in accordance with the user's requirements. The adapted HUSR/GSR software produces the location, shape, and size of the collimator aperture which will give spectra close to the required spectra. We can produce the required spectra from any field map. In this study, the ILC electron beam with 150 GeV travelling through the measured field map of the ILC helical undulator is used as an example to evaluate these new techniques and see the possibility of having a narrow beam from the ILC gamma-ray beam. There is no guarantee that the resulting collimator aperture can be physically constructed.

6.5.1 First Technique

I have used the measured field map in calculations to find a narrow bandwidth spectrum. The method of this technique is explained in the following steps:

1. Design the required spectra (from user).

2. Select those observation points which have a spectra which lies fully underneath the design spectra or is exactly equal to the designed spectra in every energy bin.

3. Based on the selected observation points a collimator aperture can be defined, which gives the spectrum which is close as possible to the required spectra.

Fig. 6.17 shows the comparison between a narrow design spectrum peaked at the first harmonic energy and the resulting spectrum.

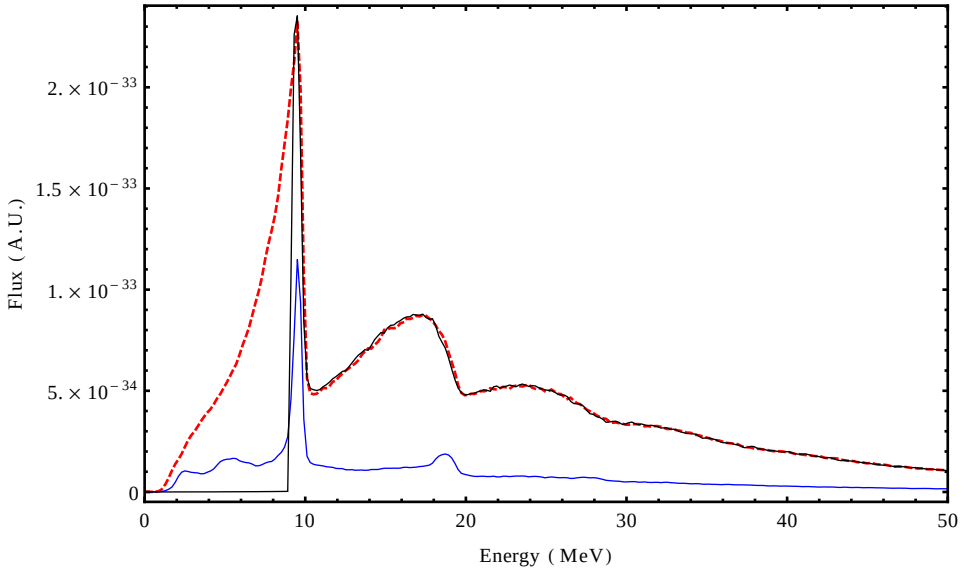

FIGURE 6.17: The comparison between the design spectra and the result spectra, full spectra showing in red dashed line, and designed spectra in black, and the result spectra in blue.

Fig. 6.18 shows the shape of the aperture which will best match our required energy spectra obtained from the measured field map.

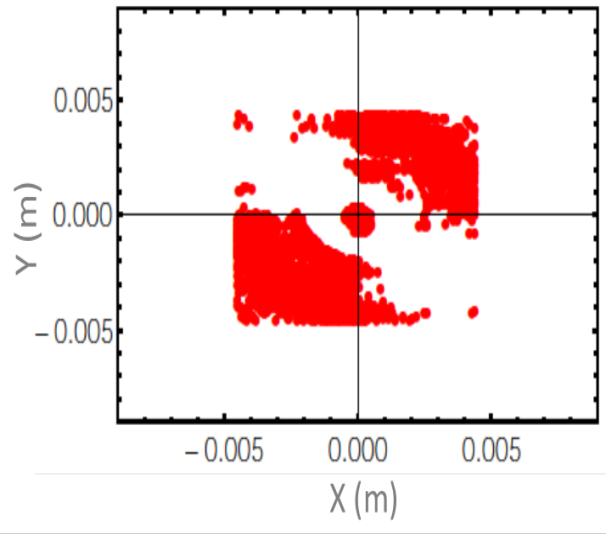

FIGURE 6.18: Shape of the square aperture obtained from the collimator algorithm based on an initial square mesh of observation points. Red shows the points where we can have a narrow bandwidth spectra from the simulated map (i.e each red point represent a hole in a collimator).

6.5.2 Second Technique

The following steps were used in this technique:

1. Design the required spectra from user's requirements.
2. Calculate the chi-squared for each individual observation point spectra compared to the required spectra using Eq 6.1:

$$\chi^2 = \sum \frac{(O_S \times A - R_S)^2}{R_S} \tag{6.1}$$

where, O_S is the observed spectra, R_S is the required spectra, and A is the normalization (the total flux of the required spectrum divided by the total flux of the observed spectrum).

3. From chi-squared one can tune the selections of points and control the bandwidth e.g choosing the points which have small chi-squared is useful, because the difference between the required spectra and the produced spectra is very small, but choosing the points with large chi-squared will increase the bandwidth of the energy spectrum.

4. Based on the selected observation points a collimator aperture can be defined, which gives the spectrum which is close as possible to the required spectra.

Fig. 6.19 shows the comparison between the design spectrum and the result spectrum. Fig. 6.20 show the distributions of the observations points based on the chi square results, where closer to zero is better. I varied the value of chi-squared till I found good match with the design spectrum. I selected the values of chi-squared which is less than 0.15. I can choose smaller chi-squared which will result to a narrower bandwidth.

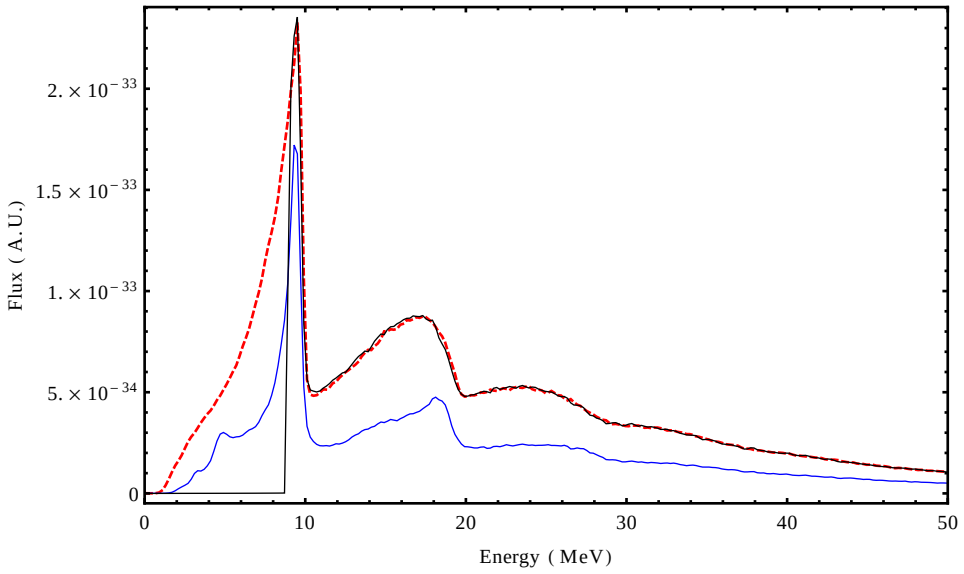

FIGURE 6.19: The comparison between the design spectrum and the result spectrum. The full spectrum is shown in red dashed line, and the design spectrum in black, and the result spectrum in blue.

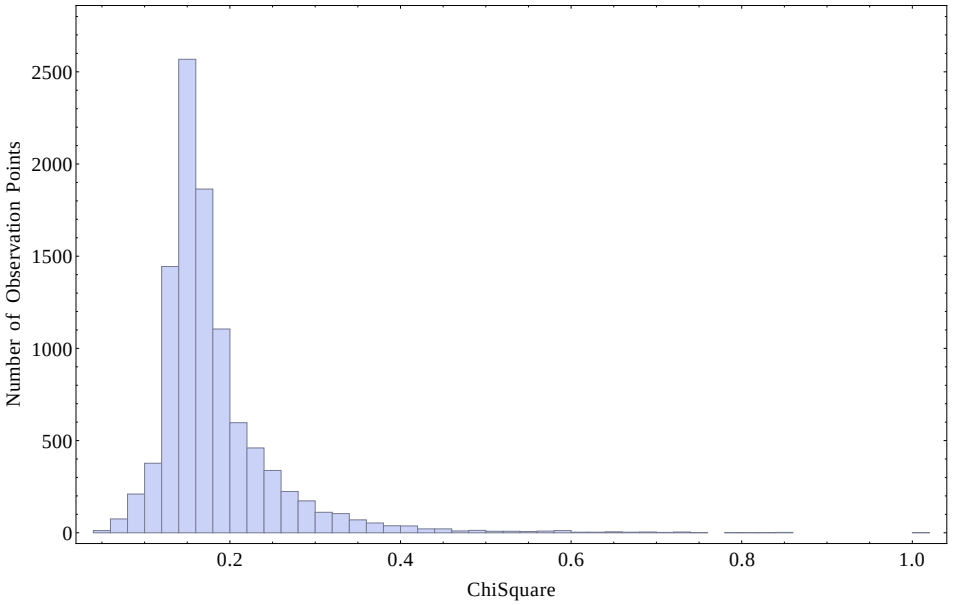

FIGURE 6.20: The distributions of the observations points based on the chi-squared.

Fig. 6.21 shows the shape of the aperture which will best match our required energy spectrum obtained from measured field map.

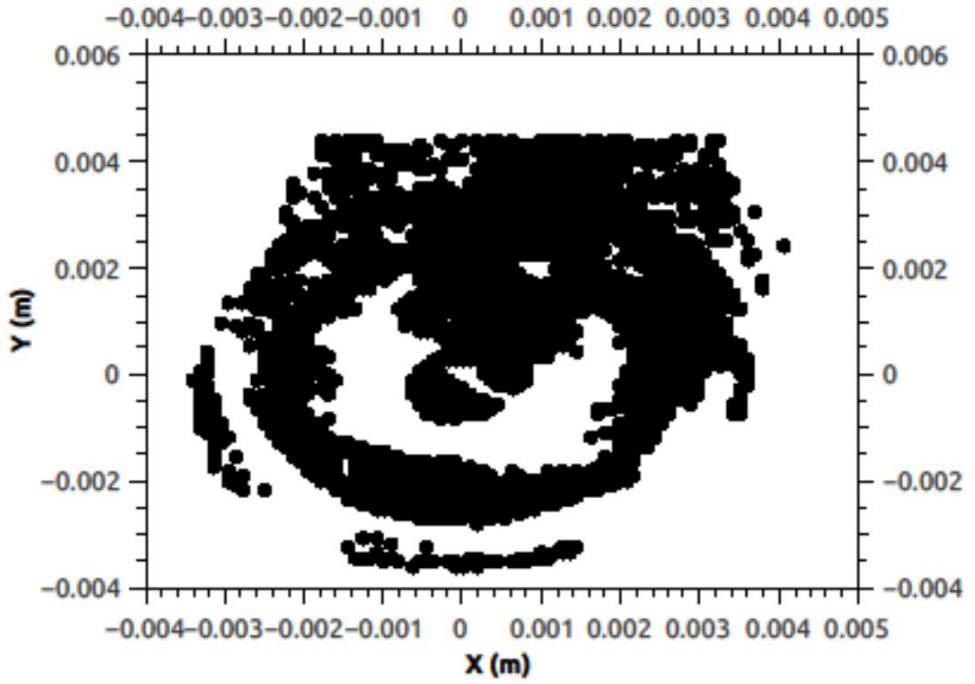

FIGURE 6.21: Shape of the square aperture obtained from the collimator algorithm based on an initial square mesh of observation points. Black shows the points where we can have a narrow bandwidth spectra from the simulated map (i.e each black point represent a hole in a collimator).

6.5.3 Comparison between these two techniques

A comparison between the two collimated energy spectrums is shown in Fig. 6.22. As we can see the first technique has a narrow bandwidth $\approx 5\%$ which is better than the second technique $\approx 7\%$. But the flux peak height from the second technique is $\approx 1.9 \times 10^{-33}$ photon/s which is better than the first technique $\approx 1.35 \times 10^{-33}$ photon/s. The possibility of designing the collimator will be discussed in section 6.6. The possibility of construction the required collimator will be discussed in section 6.7.

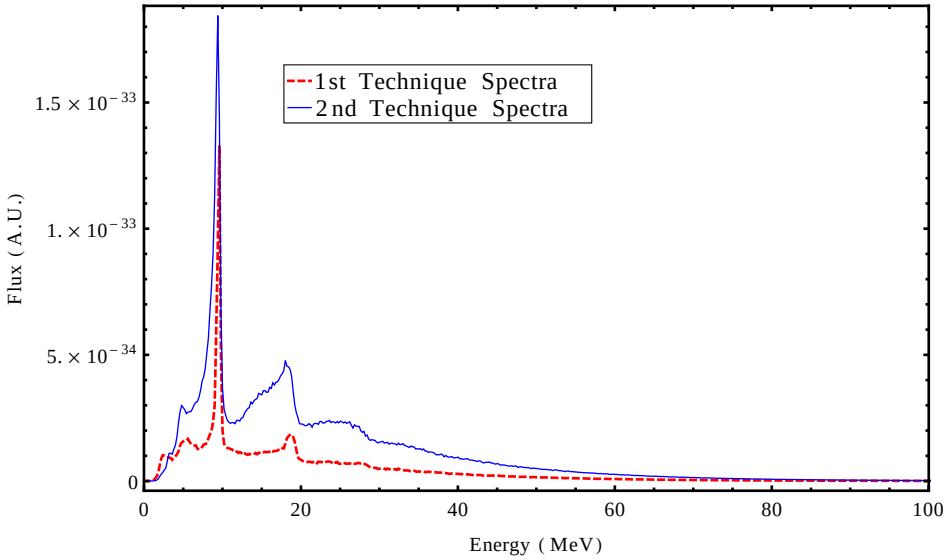

FIGURE 6.22: Comparison between the two collimated energy spectrums. Collimated energy spectra from 1st technique in dashed red. Collimated energy spectra from 2nd technique in blue solid line.

6.6 Obtaining a Narrow Bandwidth From The ILC Gamma-ray Beam

In this section, by using the two techniques which are described earlier, I investigate the possibility of obtaining a narrow bandwidth spectrum from the high intensity gamma-ray beam which is required for the positron source production. In the previous section one module of the helical undulator was used. As described earlier, 84 modules will be used for the ILC helical undulator. Therefore, each module will have a different spectrum due to the error in the magnetic field. These techniques will produce different collimator shapes for each module, so designing a single collimator which is optimal for every module is not possible.

In order to investigate this in systematic way, I used 20 simulated magnetic field maps of the helical undulator which has the required parameters of the ILC. I

simulated the output from an electron beam with a 150 GeV energy travelling inside each of these 20 maps. The two techniques described in section 6.5 were used to obtain the required collimator shape for the narrow bandwidth spectrum. The description of the method will be described in the next steps:

1. Produced 20 different collimator apertures which will fulfil and give the required spectrum.

2. Each aperture is described by a list of observation points. I used 0 to indicate an observation point selected as a hole in the collimator and 1 to indicate that it will be solid material.

3. I sum over all the 20 apertures for each observation point. For example for a specific observation point if the sum is zero that means this is a hole for all the 20 simulated models.

4. I plot a histogram of the results showing the number of times each observation point fails the condition.

A histogram of the results from the first technique showing the number of times each observation point fails the condition in is shown Fig. 6.23. Selected observation points which fail the criteria less than fifteen times are shown in Fig. 6.24. Fig. 6.25 shows the collimated narrow bandwidth spectra which is obtained.

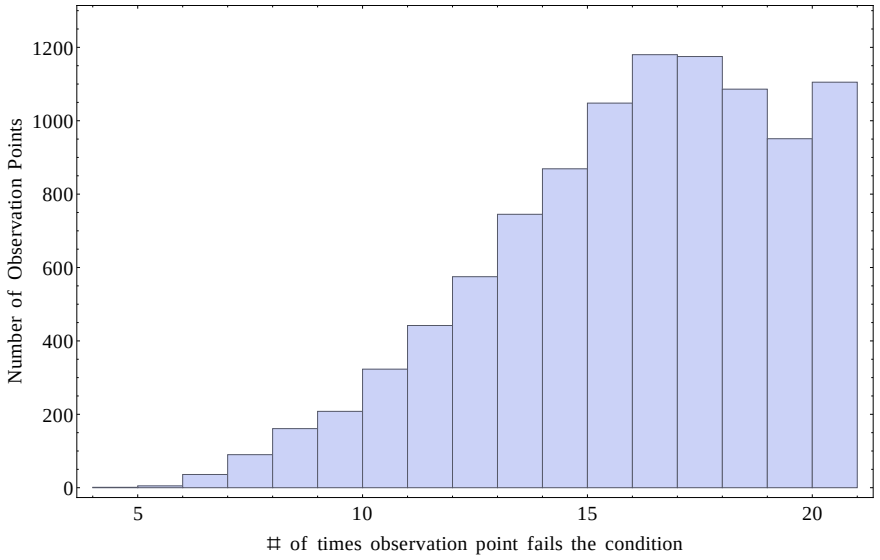

FIGURE 6.23: Histogram of the results from the first technique is showing the number of times observation point fails the condition described in the main text.

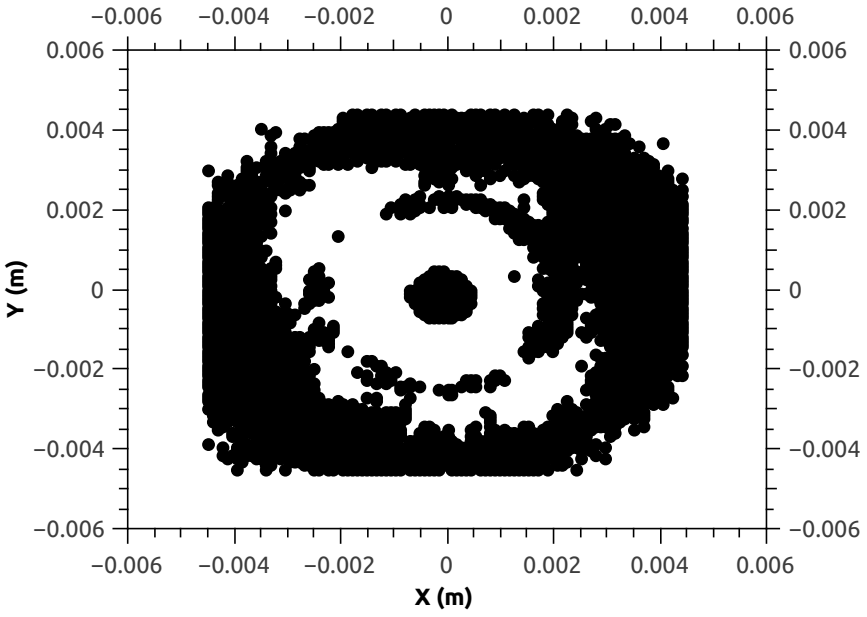

FIGURE 6.24: Selected observation points which failed the condition less than 15 times out of the 20 simulated helical undulator modules (Each black point represent a hole in a collimator).

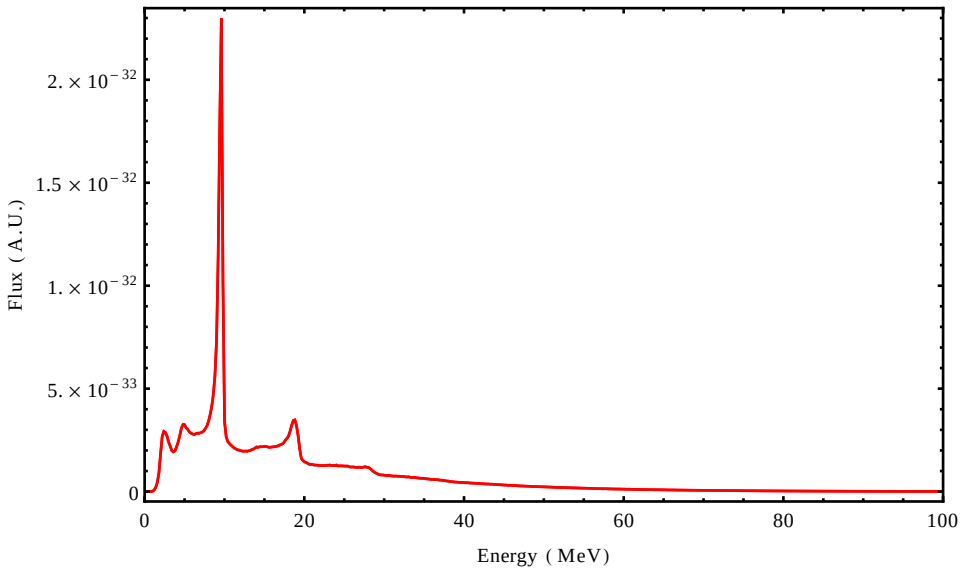

FIGURE 6.25: The collimated energy spectrum showing a bandwidth of ≈ 0.5 MeV.

In the second technique I followed these steps to select the aperture shape:

1. Produced 20 different collimator shape which will fulfil and give the required spectra individually for each of the 20 simulated undulator modules.

2. For each module, each observation point is assigned a value between 0 to 1 of chi-squared as described earlier. In our case, smaller values meet the condition and larger values near to 1 indicate not meeting the condition.

3. I sum over all the conditions status, for example a specific observation point if the sum is small or close to zero that's mean this is a common area for all the 20 simulated modules or most of them.

4. I plot a histogram of the results showing the number of times each observation point fails the condition.

The histogram of the results from the second technique is shown in Fig. 6.26. Selected observation points which have a value less than 5 are shown in Fig. 6.27.

I varied the value of chi-squared till I found good match with the design spectrum. I selected the values of chi-squared which is less than 5. One can choose smaller values which will result in a narrower bandwidth. Fig. 6.28 shows the collimated narrow bandwidth spectrum corresponding to the observation points shown in Fig. 6.27.

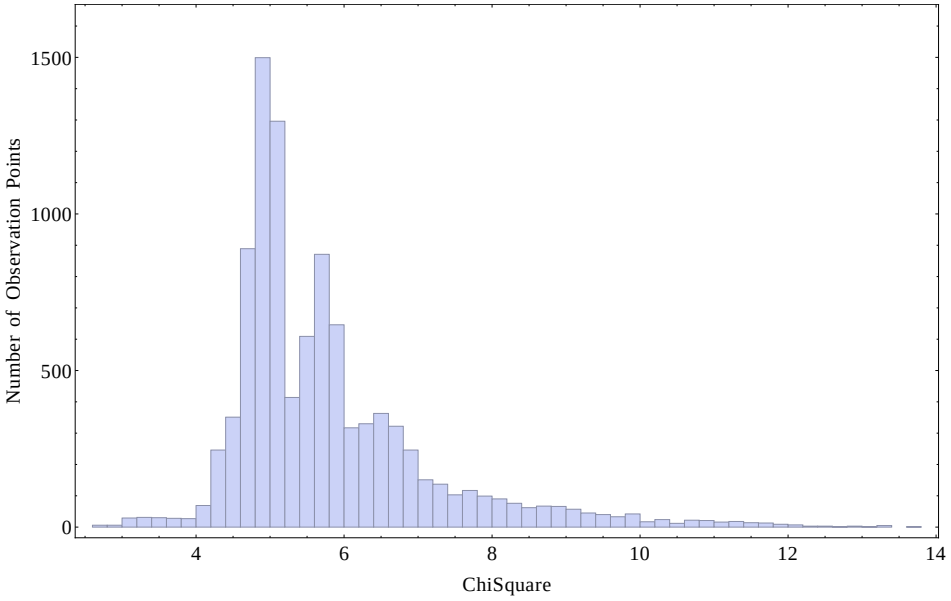

FIGURE 6.26: Histogram of the results from the second technique is showing the number of times observation point based on the chi-squared condition described in the main text.

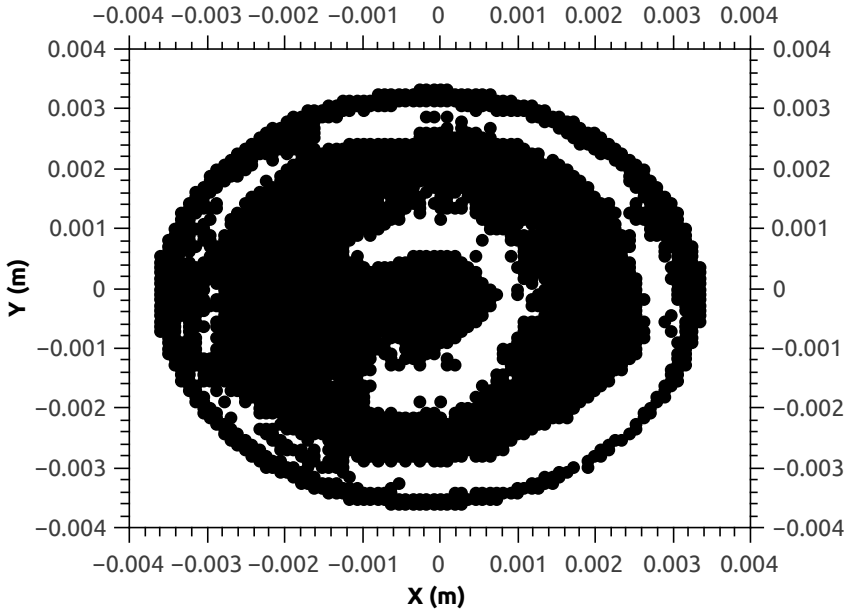

FIGURE 6.27: Selected observation points which have a chi-squared less than 5 out of the 20 simulated helical undulator modules (Each black point represent a hole in a collimator).

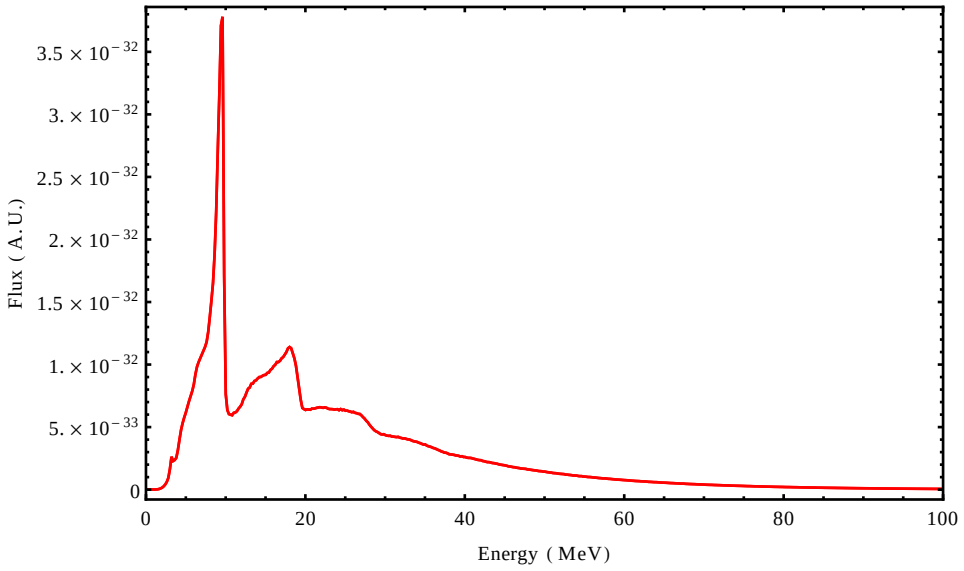

FIGURE 6.28: The collimated energy spectrum showing a bandwidth of $\approx$ 0.7 MeV.

Fig. 6.29 showing a comparison between the collimated energy spectrum produced from 20 simulated modules as obtained from the second technique as described in the main text.

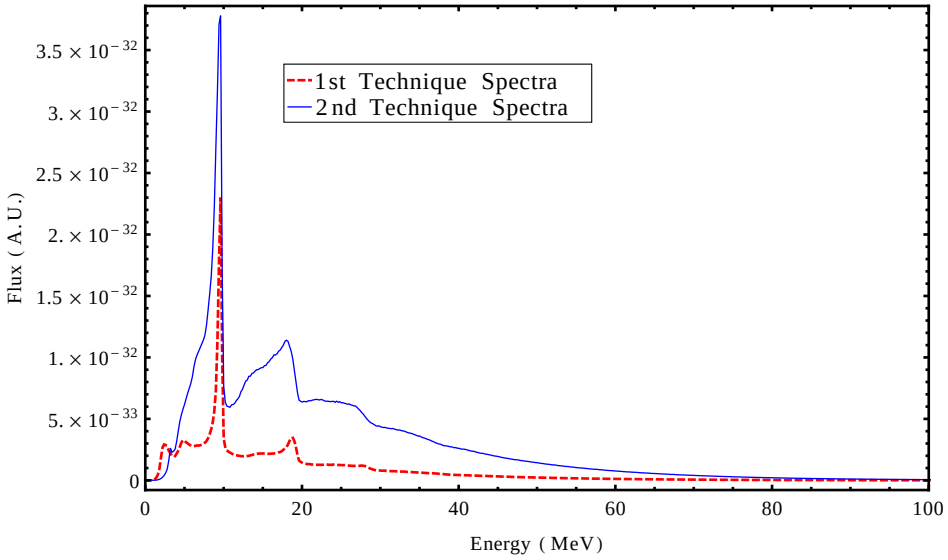

FIGURE 6.29: Comparison between the collimated energy spectrum produced from 20 simulated models. Red dashed line show the results from the first technique and solid blue line shows the results from second technique.

From comparison we can see the second technique has more flux than the first one while the first technique has a narrower energy bandwidth. From the comparison between these two techniques we can see there is a common area in both of them.

Using these two techniques, I have been able to determine the an idealised collimator shape corresponding to the required spectrum. The possibility of designing a similar shape in a real experiment is of course very challenging. The code gives us the ability to choose any required energy bandwidth, but the values chosen in this initial study are comparable with other nuclear/gamma-ray facilities.

6.7 Possibility of Constructing The Required Collimator

From the parameters of the ILC, the helical undulator magnetic field is 0.88 T. A high energy photon with an average energy of 10 MeV will be produced for the first harmonic from the electron beam which passes through this helical undulator. This electron beam will have 5 pulses per a second and each pulse will have 2625 bunches. There will be approximately 2×10^{10} electrons in each bunch. 7.8×10^{16} photons per second will be produced when this electron beam travels through the 84 modules of the undulator, where each module is 1.7825 m long. Therefore, the ILC helical undulator will produce an average photon beam power of approximately 131 kW.

The average power which will be deposited in the collimator produced from the first technique is about 108 kW, and in the collimator produced from the second technique is about 69 kW. The current ILC collimator design showing that the power deposition in the collimator is in a range of 70 KW to 90 KW [73]. The current ILC collimator made from pyrolytic graphite, titanium, iron and tungsten and has an aperture of 1.4 mm radius with a length of 190 cm [73]. Therefore, the power which deposited in the second collimator is reasonable compared to the power which is deposited in the photon collimator which is in the current ILC design and sits before the positron-production target in order to protect the target station and control the polarisation of the positrons [73]. One could consider designing a collimator with contain different stages, for example, at the first stage the outer beam could be collimated then the collimator could be narrowed in the second stage to select a narrower beam, and so on. In this way we could spread the power of the beam and minimize the effect on the collimator. The radius of the proposed collimators is in a range of 0.8 mm to 1.2 mm which is a challenging and would required more investigations.

6.8 Conclusion

In this chapter, I have explained the HUSR/GSR software and discussed the new features which I added to it. I investigated the energy spectrum produced from three types of helical undulator magnetic field: ideal, measured, and simulated. The photon flux produced from the measured map is less than that produced from the ideal map by $\approx 9\%$, which is due to the errors in the magnetic field. There was good agreement between the spectrum produced from the measured field map and the spectrum produced from the simulated field map at a level of 2%. Also, I studied the energy spectrum produced from 20 simulated maps and the deviation was at a level of 3%.

Moreover, I studied the deviation of the energy spectrum produced from injecting the particles randomly in different angles and positions according to the expected spread of the beam in the undulator, where I found that in the ideal field map case, the average peak height on the first harmonic reduced by $\approx 4\%$ and by $\approx 6\%$ for the average total flux. In the measured field map case, the average peak height on the first harmonic reduced by $\approx 6\%$ and by $\approx 11\%$ for the average total flux. Therefore, the effects of using the realistic beam spot size is fairly small compare to the errors in the magnetic field map. The expected reduction in flux from considering the effects of finite beam size and realistic errors in the undulator magnetic field could be compensated for by optimising the beam trajectory through the undulator or if required increasing the undulator length to approximately 160 m.

In addition, I have discussed the possible additional applications of the ILC gamma ray source to use the otherwise-wasted beam. Two general techniques were developed to produce the collimator shape which fulfills the required spectra from users. Although, it is still not clear where it is possible to build such collimator and further investigations are required.

Based on these results, I believe there is a good chance that the spent ILC gamma-ray beam could be put to good use. ILC gamma-ray beam produces a flux which could exceed the best current flux produced from HIγS (Duke University) [60, 61] by several orders of magnitude reaching 10^{13} photon/second with a bandwidth of 5%.

Chapter 7

Conclusion and Further Study

The ILC positron source requires a high-intensity gamma ray beam in order to produce the required positron flux. The target will need to rotate to spread out the heat coming from the beam. The torque generated by eddy currents affects the movement of the target due to the AMD optic which is a major challenge for the ILC current baseline design. To overcome this problem, experiment and simulations using the OPERA 3D software were performed to validate the OPERA 3D software, investigate this problem and to test a proof-of-principle magnet design. I obtained good agreement between the results from the eddy current experiment and the OPERA 3D software at the level of 3%.

A novel magnet design was designed to reduce the torque acting on the target movement. A solution for the torque was performed experimentally and by simulations. This new magnet design is a big improvement and has shown a significant reduction of the torque. If this novel magnet design is to be built in the future, further study is required towards the infrastructure including, powering, and cooling the magnets.

The trajectory of the electron beam inside a perfect ILC helical undulator was well understood and studied in more detail. In order to understand the effects of the errors inside the ILC helical undulator, a general semi-analytical model was used

to generate a realistic magnetic field and to evaluate the electron trajectory inside the ILC helical undulator as well as the energy spectrum. After investigating more than 20 simulated helical undulator field maps, the deviation of the electron is predicted to be of the order of ten microns 4.0×10^{-6} m, and has $\approx 10\%$ of effects overall the energy spectrum. Therefore, this is reasonable and in acceptable range.

The ILC photon beam has a flux of 7×10^{16} m. Most of this beam will not be absorbed by the target. Therefore there is a demand to utilize the otherwise wasted beam. In order to investigate the possibility of using this beam, I presented possible additional applications for this beam, which will not require any addition modifications towards the beam. Moreover, I included an investigation which resulted in the development of two general techniques to calculate a collimator aperture from the user requirements. For example, a narrow bandwidth energy beam might be required. There is good output from those techniques regarding producing the required energy bandwidth of 5%, but further investigations to study the possibility of building such collimators are required.

Investigating the track of many particles through the undulator by injecting the particles using the realistic beam spot and size to estimate the effect of the energy spectrum would be an open field for future research. Also, the errors in the magnetic field caused a spread in the electron beam trajectory, therefore the polarizations of the beam will also be affected and could be investigated.

Appendix A

Simulations for the ILC conventional source

As mentioned earlier in the introduction, there is a recent study which makes the conventional positron source feasible for the ILC by changing the pulse time structure of the electron beam striking on the target and induces an advanced cooling system for the target [21]. Here I present a simulation to study the effect of the torque on the target due to immersing the target partially while rotating at the proposed speed of 250 rpm.

The slowly rotating target consists of a 30 mm rim of tungsten and a 170 mm radius disc of copper. The thickness of the target is 14 mm. I used a solenoidal magnetic field with a peak field on the target of approximately 0.55 T. Due to the difficulties of simulating the two parts of the target with different conductivities in the OPERA 3D software, I simulated each part separately. To arrive at an estimate I simulated:

- A W rim with 30 mm width
- A solid W disc with a radius of 170 mm
- A solid W disc with a radius of 200 mm

I then simulated the same 3 scenarios for Cu. Table A.1 shows the results:

Based on these numbers I estimate the torque acting on the W-Cu target to be in the range 10.8 Nm to 18.8 Nm (calculated from firstly a 200 mm solid disc of W

TABLE A.1: Summary of the torque acting on each part

Materials	Torque N.m
W rim 30 mm	0.18
W Solid disc 170 mm	2.20
W Solid dis 200 mm	5.80
Cu rim 30 mm	0.62
Cu Solid disc 170 mm	7.20
Cu Solid disc 200 mm	19.3

170 mm solid disc of W + 170 mm solid disc of Cu and secondly from a 200 mm solid disc of Cu Cu rim + W rim respectively) equating to a power between 0.28 kW and 0.49 kW.

I have checked the results of the torque in the two rim simulations against the simplified semi-analytical model Equation 4.10, and the results agree at the level of 10%.

Fig. A.1, A.2, and A.3 show the simulated models of the slowly-rotating target of the ILC conventional source.

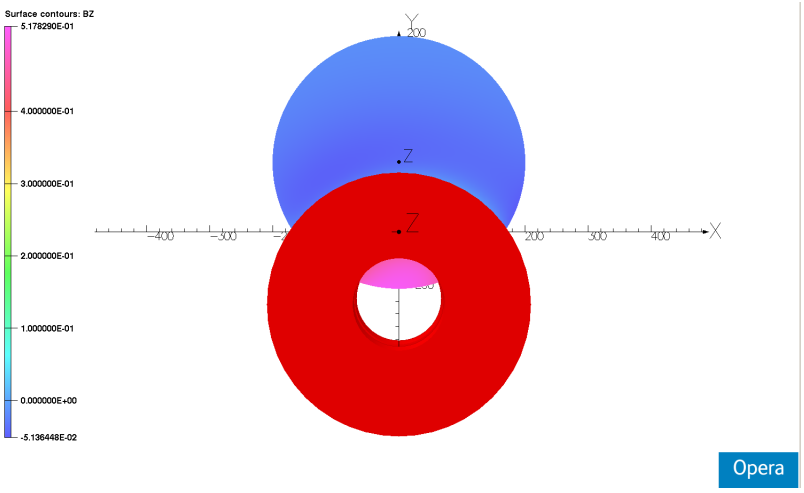

FIGURE A.1: Simulated model of the slowly-rotating target of the ILC conventional source, including the solenoid magnet.

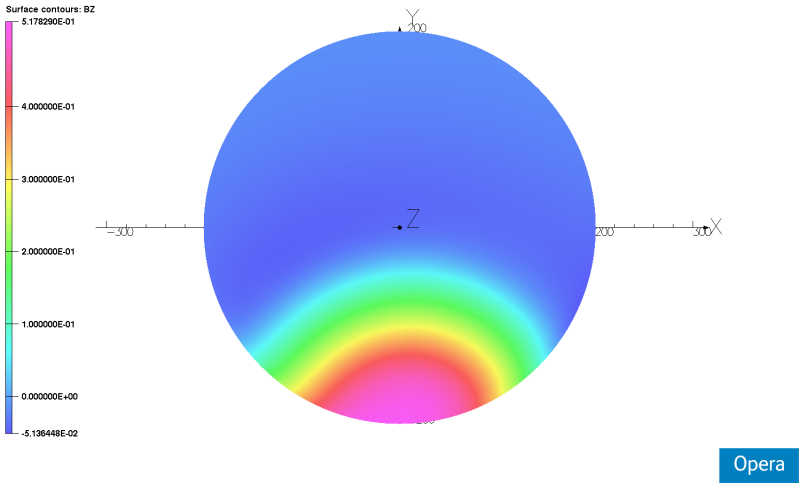

FIGURE A.2: The magnetic flux with a peak of ≈0.5 T acting on the solid disc.

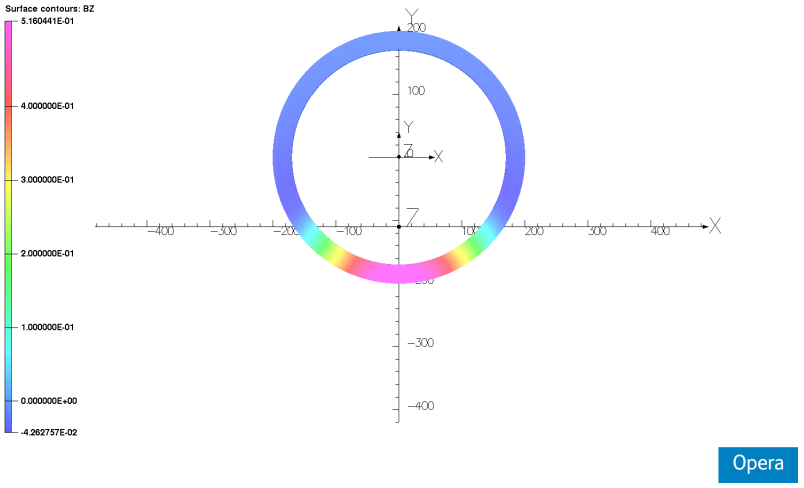

FIGURE A.3: The magnetic flux with a peak of ≈0.5 T acting on the rim.

Appendix B

Gamma-ray Flux and Energy Distributions on Target

In this section, I present the flux distribution and the average energy distribution on the target from three types of helical undulator magnetic field: ideal, measured, and simulated realistic field, which was explained in chapter 5. It is very useful to know how flux and the energy distribute on the target. This will help to know how much energy will be deposited in the target or the collimator and the locations of this energy.

Fig. B.1 shows the flux distribution from the ideal helical undulator magnetic field, and Fig. B.2 show the average energy distribution on target from the ideal helical undulator magnetic field. Fig. B.3 show the flux distribution contour plot from the ideal helical undulator magnetic field.

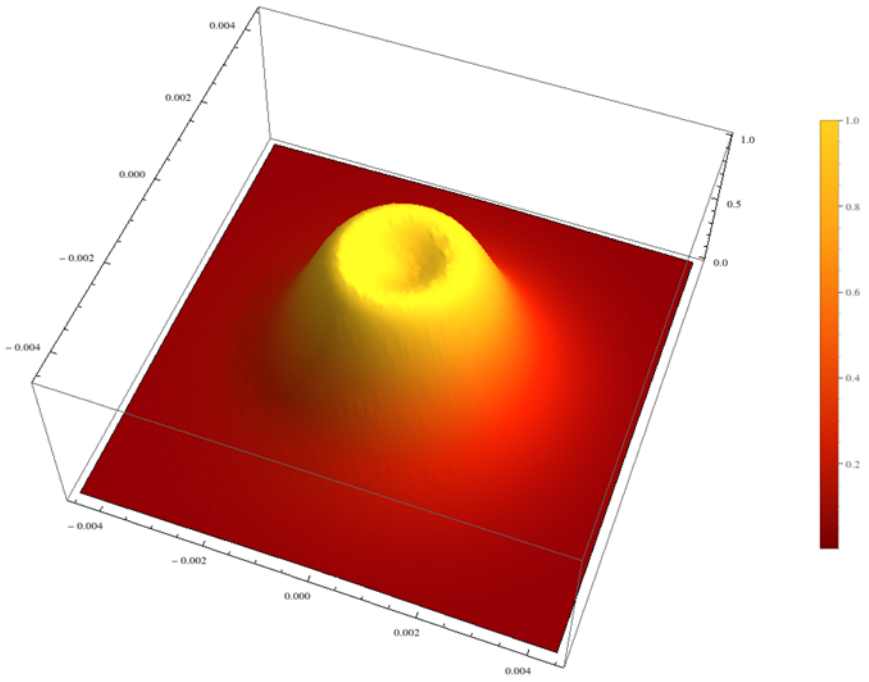

FIGURE B.1: Flux distribution from the ideal helical undulator magnetic field. I have normalised the flux by divided all numbers by the maximum number where 1 means highest value.

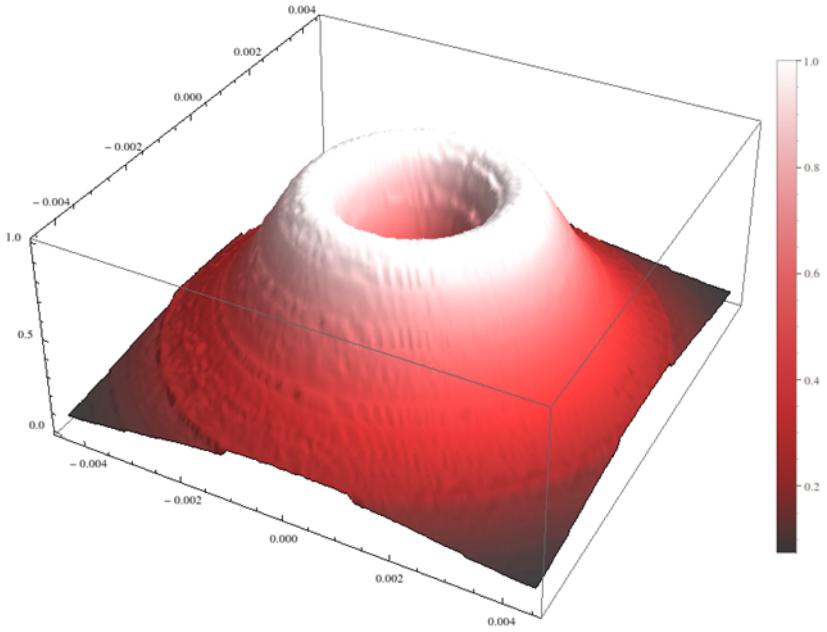

FIGURE B.2: Average energy distribution on target from the ideal helical undulator magnetic field. I have normalised the flux by divided all numbers by the maximum number where 1 means highest value.

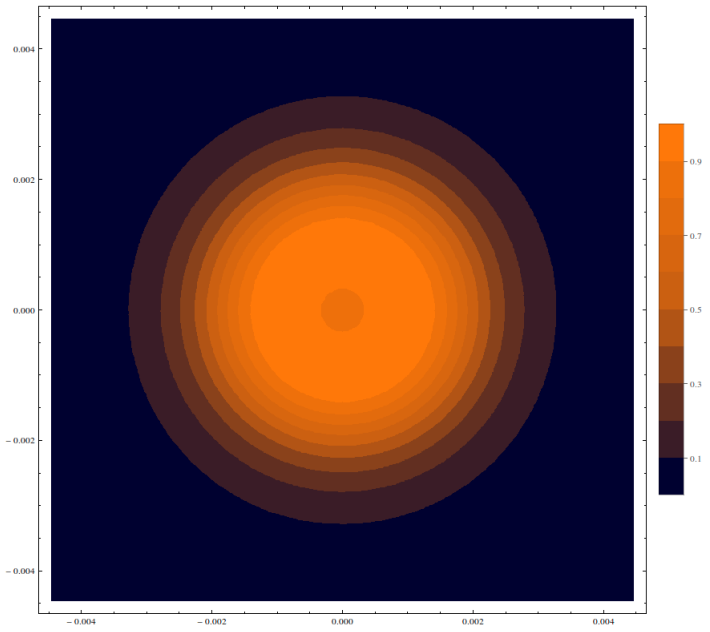

FIGURE B.3: Flux distribution contour plot from the ideal helical undulator magnetic field. I have normalised the flux by divided all numbers by the maximum number where 1 means highest value.

Fig. B.4 shows the flux distribution from the measured helical undulator magnetic field, and Fig. B.5 show the average energy distribution on target from the measured helical undulator magnetic field. Fig. B.6 show the flux distribution contour plot from the measured helical undulator magnetic field.

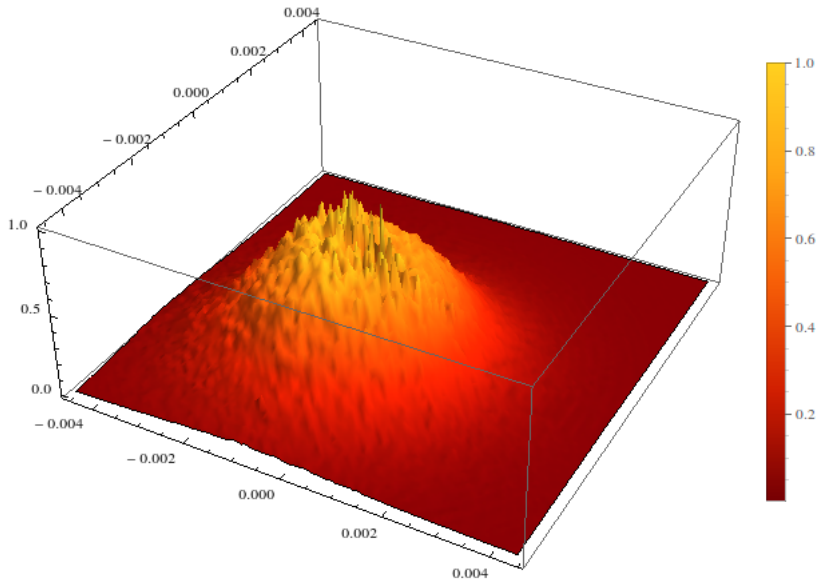

FIGURE B.4: Flux distribution from the measured helical undulator magnetic field. I have normalised the flux by divided all numbers by the maximum number where 1 means highest value.

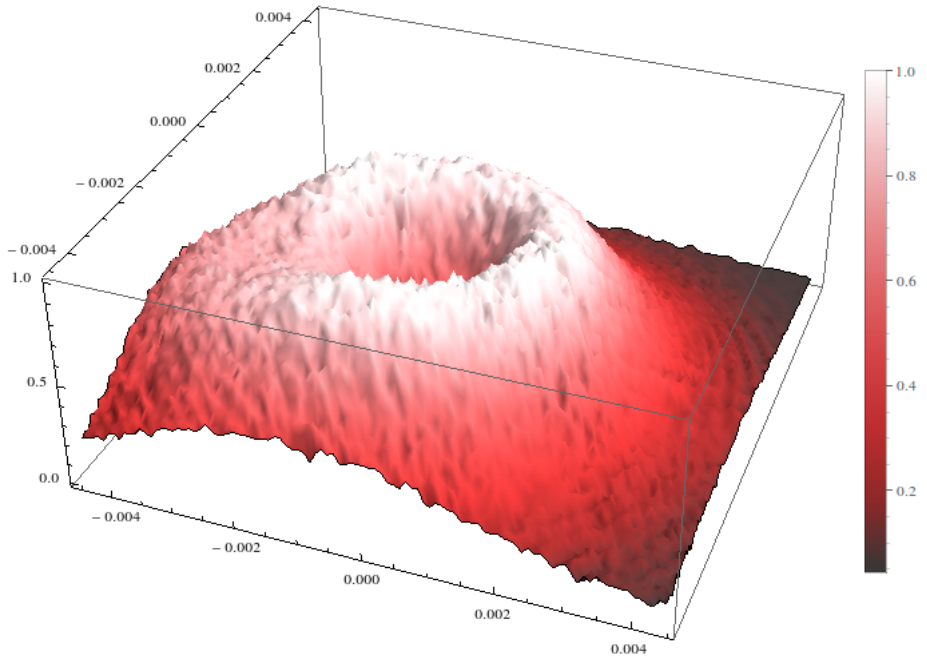

FIGURE B.5: Average energy distribution on target from the measured helical undulator magnetic field. I have normalised the flux by divided all numbers by the maximum number where 1 means highest value.

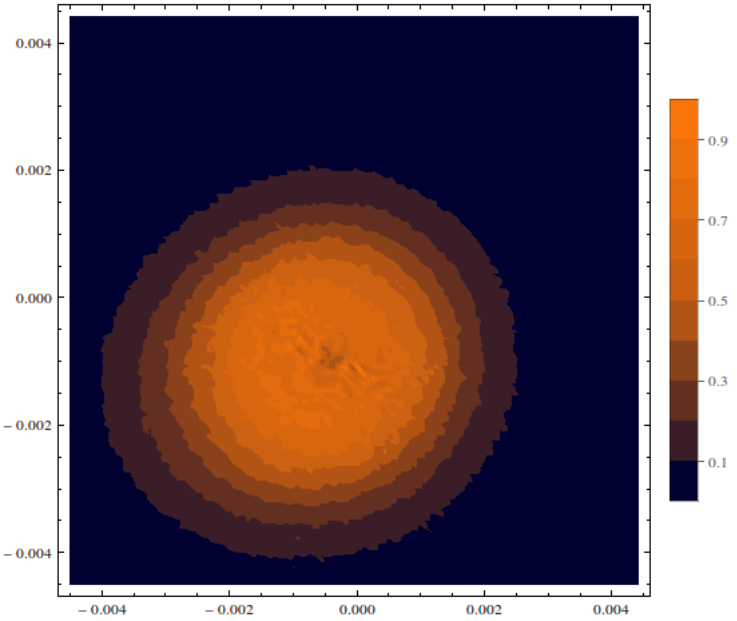

FIGURE B.6: Flux distribution contour plot from the measured helical undulator magnetic field. I have normalised the flux by divided all numbers by the maximum number where 1 means highest value.

Fig. B.7 shows the flux distribution from the simulated helical undulator magnetic field , and Fig. B.8 shows the average energy distribution on target from the simulated helical undulator magnetic field. Fig. B.9 shows the flux distribution contour plot from the simulated helical undulator magnetic field. This is one representative example of the 20 simulated field map.

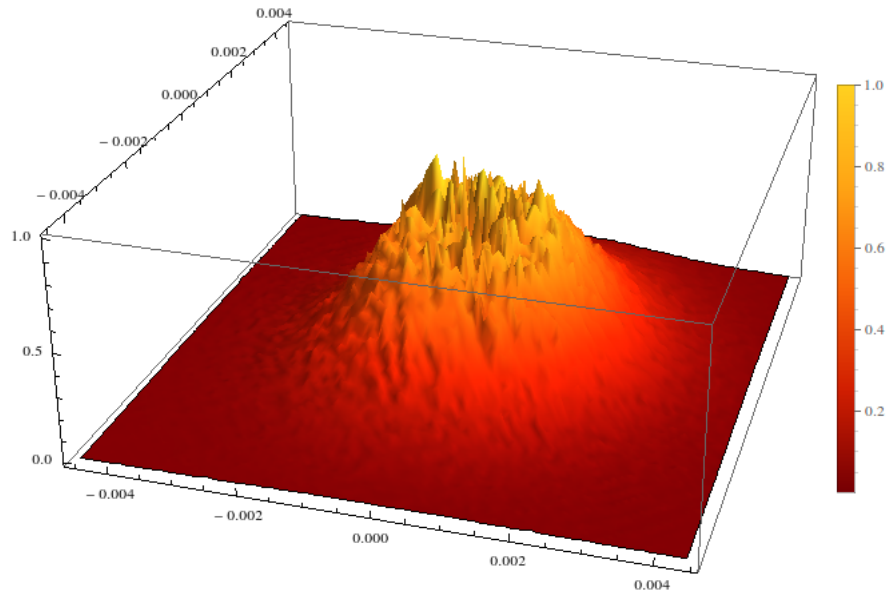

FIGURE B.7: Flux distribution from the simulated helical undulator magnetic field. I have normalised the flux by divided all numbers by the maximum number where 1 means highest value.

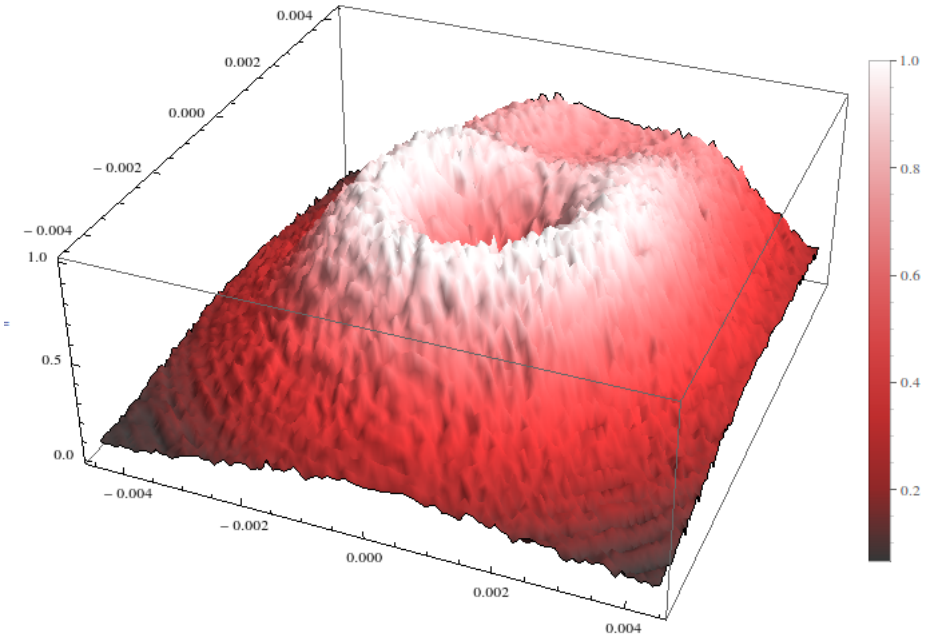

FIGURE B.8: Average energy distribution on target from the simulated helical undulator magnetic field. I have normalised the flux by divided all numbers by the maximum number where 1 means highest value.

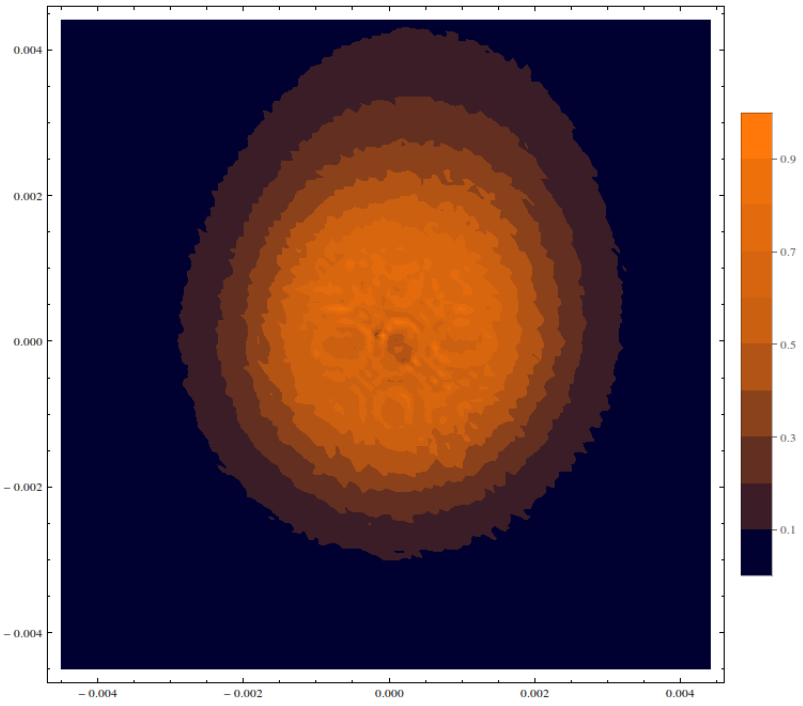

FIGURE B.9: Flux distribution contour plot from the simulated helical undulator magnetic field. I have normalised the flux by divided all numbers by the maximum number where 1 means highest value.

TABLE B.1: Summarized table of important difference between the ideal, measured, and simulated energy spectrum

Parameters	Ideal	Measured	Simulated
Average Energy	15.944 MeV	13.856 MeV	15.009 MeV
St.Dev of Energy	9.1269 MeV	8.0768 MeV	7.4802 MeV
Total flux	$1.291 \times 10^{-31}\,\gamma/s$	$1.197 \times 10^{-31}\,\gamma/s$	$1.120 \times 10^{-31}\,\gamma/s$

From table B.1, we can clearly see that the total flux for both measured and simulated field maps have reduced by $\approx 10\%$ overall. In addition, the average energy has reduced by $\approx 10\%$ in the case of the measured field map and by $\approx 6\%$ in the case of the simulated field map. These reductions are due to the errors in the measured and simulated field maps.

Bibliography

[1] ILC website. 2012 May 21;Available from: http://www.linearcollider.org/.

[2] Bruning O, Burkhardt H, Myers S. The large hadron collider. Progress in Particle and Nuclear Physics. 2012;67(3):705 – 734. Available from: http://www.sciencedirect.com/science/article/pii/S0146641012000695.

[3] Phinney N, Toge N, Walker N. ILC Reference Design Report Volume 3 - Accelerator; 2007. arXiv:0712.2361. Comments: A version with high resolution pictures can be found at http://www.linearcollider.org/cms/?pid=1000437 The full authorlist is inside the report.

[4] Gerward L. Paul Villard and his discovery of gamma rays. Physics in Perspective (PIP). 1999;1(4):367–383.

[5] Chesworth A, Clarke J, Dobbing G, Holder D, Owen H, Poole M, et al. DIAMOND: a UK national light source project. In: Particle Accelerator Conference, 1999. Proceedings of the 1999. vol. 4. IEEE; 1999. p. 2433–2435.

[6] Krause W, Korol AV, Solov'yov AV, Greiner W. Photon emission by ultra-relativistic positrons in crystalline undulators: the high-energy regime. Nuclear Instruments and Methods in Physics Research Section A: Accelerators, Spectrometers, Detectors and Associated Equipment. 2002;483(1):455–460.

[7] Ohkuma H, Mochihashi A, Oishi M, Suzuki S, Tamura K, Takashi Nakano R, et al. Production of quasi-monochromatic GeV photons by compton scattering using undulator x-ray radiation at SPring-8;.

[8] Weller HR, Ahmed MW. The HIγS facility: a free-electron laser generated gamma-ray beam for research in nuclear physics. Modern Physics Letters A. 2003;18(23):1569–1590.

[9] Compton AH. A quantum theory of the scattering of X-rays by light elements. Physical Review. 1923;21(5):483.

[10] Milburn R. Electron Scattering by an Intense Polarized Photon Field. Phys Rev Lett. 1963 Feb;10:75–77. Available from: http://link.aps.org/doi/10.1103/PhysRevLett.10.75.

[11] Kulikov O, Telnov YY, Filippov E, Yakimenko M. Compton effect on moving electrons. Physics Letters. 1964;13(4):344–346.

[12] Weller HR, Ahmed MW, Gao H, Tornow W, Wu YK, Gai M, et al. Research opportunities at the upgraded HIγS facility. Progress in Particle and Nuclear Physics. 2009;62(1):257–303.

[13] Adriani O, Albergo S, Alesini D, Anania M, Angal-Kalinin D, Antici P, et al. Technical Design Report EuroGammaS proposal for the ELI-NP Gamma beam System. arXiv preprint arXiv:14073669. 2014;.

[14] Adriani O, Barbarino G, Bazilevskaya G, Bellotti R, Boezio M, Bogomolov E, et al. An anomalous positron abundance in cosmic rays with energies 1.5–100 GeV. Nature. 2009;458(7238):607–609.

[15] Moskalenko IV, Strong A. Production and propagation of cosmic-ray positrons and electrons. The Astrophysical Journal. 1998;493(2):694.

[16] Grieder PKF. Cosmic rays at earth: researcher's reference manual and data book. Amsterdam: North-Holland; 2001.

[17] Dirac PAM. The Quantum Theory of the Electron. Proceedings of the Royal Society of London A: Mathematical, Physical and Engineering Sciences. 1928;117(778):610–624.

[18] Bethe H, Heitler W. On the Stopping of Fast Particles and on the Creation of Positive Electrons. Proceedings of the Royal Society of London A: Mathematical, Physical and Engineering Sciences. 1934;146(856):83–112.

[19] Olive KA, et al. Review of Particle Physics. ChinPhys. 2014;C38:090001.

[20] Bharadwaj VK, Batygin YK, Sheppard JC, Schultz DC, Bodenstein S, Gallegos J, et al. Analysis of Beam-Induced Damage to the SLC Positron Production Target. In: Particle Accelerator Conference, 2001. PAC 2001. Proceedings of the 2001. vol. 3. IEEE; 2001. p. 2123–2125.

[21] Omori T, Takahashi T, Riemann S, Gai W, Gao J, Kawada Si, et al. A conventional positron source for international linear collider. Nuclear Instruments and Methods in Physics Research Section A: Accelerators, Spectrometers, Detectors and Associated Equipment. 2012;672:52–56.

[22] Omori T, Fukuda M, Hirose T, Kurihara Y, Kuroda R, Nomura M, et al. Efficient propagation of polarization from laser photons to positrons through compton scattering and electron-positron pair creation. Physical review letters. 2006;96(11):114801.

[23] Clarke JA. The science and technology of undulators and wigglers. Oxford series on synchrotron radiation. Oxford: Oxford Univ. Press; 2004.

[24] Kincaid BM. A short-period helical wiggler as an improved source of synchrotron radiation. Journal of Applied Physics. 1977;48(7):2684–2691.

[25] V E Balakin AAM. The Conversion System for Obtaining highly polarized Electrons and Positrons. INP, Novosibirsk. 1779;p. INP–Preprint 79–85.

[26] Aguilar-Saavedra J, et al. TESLA technical design report part III: Physics at an e+e- linear collider. arXiv preprint hep-ph/0106315. 2001;12.

[27] Glantz R. A feasibility study of high intensity positron sources for the S-band and TESLA linear colliders. 1997;.

[28] Scott DJ. An Investigation into the Design of the Helical Undulator for the International Linear Collider Positron Source. University of Liverpool; 2008.

[29] Alexander G, Barley J, Batygin Y, Berridge S, Bharadwaj V, Bower G, et al. Undulator-based production of polarized positrons. Nuclear Instruments and Methods in Physics Research Section A: Accelerators, Spectrometers, Detectors and Associated Equipment. 2009;610(2):451–487.

[30] Kulikov AV, Ecklund SD, Reuter EM. SLC positron source pulsed flux concentrator. In: Particle Accelerator Conference, 1991. Accelerator Science and Technology., Conference Record of the 1991 IEEE; 1991. p. 2005–2007 vol.3. Available from: http://www.slac.stanford.edu/cgi-wrap/getdoc/slac-pub-5473.pdf.

[31] Bharadwaj V, Batygin Y, Pitthan R, Sheppard J, Vincke H, Wang JW, et al. Design Issues for the ILC Positron Source. In: Particle Accelerator Conference, 2005. PAC 2005. Proceedings of the; 2005. p. 3230–3232. Available from: http://slac.stanford.edu/pubs/slacpubs/11500/slac-pub-11690.pdf.

[32] Hesselbach S, Bailey I, Fernandez-Hernando J, Jenner L, Moortgat-Pick G, Riemann S, et al. Positron source target survivability studies.; 2009. Available from: http://accelconf.web.cern.ch/accelconf/PAC2009/papers/mo6rfp061.pdf.

[33] Clarke J, Bailey I, Baynham E, Bharadwaj V, Bradshaw T, Brummit A, et al. The design of the positron source for the international linear collider.; 2008. p. 1915–1917. Available from: http://accelconf.web.cern.ch/AccelConf/e08/papers/weobg03.pdf.

[34] Jackson JD. Classical electrodynamics. 3rd ed. New York, NY: Wiley; 1999. Available from: http://cdsweb.cern.ch/record/490457.

[35] Griffiths DJ. Introduction to Electrodynamics (3rd Edition). Pearson; 1998.

[36] Smythe WR. On Eddy Currents in a Rotating Disk. American Institute of Electrical Engineers, Transactions of the. 1942;61(9):681–684. Available from: http://ieeexplore.ieee.org/stamp/stamp.jsp?tp=&arnumber=5058590.

[37] Ming Q. Sliding mode controller design for ABS system. Virginia Polytechnic Institute and State University; 1997.

[38] Landau LD, Lifshitz EM. The Classical Theory of Fields. 4th ed. Butterworth-Heinemann; 1980.

[39] Hideo Onuki PE. Undulators, Wigglers and Their Applications. 1st ed. CRC Press; 2002.

[40] Hofmann A. The Physics of Synchrotron Radiation. Cambridge Monographs on Particle Physics, Nuclear Physics and Cosmology. Cambridge University Press; 2004.

[41] Riley KF, Bence SJ, Hobson MP. Mathematical methods for physics and engineering: a comprehensive guide. Cambridge: Cambridge Univ. Press; 1997.

[42] Kincaid BM. A short-period helical wiggler as an improved source of synchrotron radiation. Journal of Applied Physics. 1977;48(7):2684–2691.

[43] Vector Fields Software; Accessed: May 21, 2012. Available from: http://www.vectorfields.com/.

[44] Solidworks Software; Accessed: May 21, 2012. Available from: http://www.solidworks.co.uk/.

[45] Schieber D. Braking torque on rotating sheet in stationary magnetic field. Electrical Engineers, Proceedings of the Institution of. 1974 February;121(2):117–122.

[46] Zang, Lei. Study and optimisation of undulator-based polarised positron sources for linear colliders. Doctoral thesis, University of Liverpool. 2010;Available from: http://research-archive.liv.ac.uk/1445/2/ZangLei_Sept2010_1445.pdf.

[47] Bailey IR, Bailey IR, Clarke DG, Clarke JA, Davies KP, Gallagher A, et al. A Prototype Target Wheel for the ILC Positron Source. 2008;p. 3 p. Available from: https://cds.cern.ch/record/1182171.

[48] Bailey IR, Dainton JB, Scott DJ, Bharadwaj V, Sheppard J, et al. Development of a positron production target for the ILC positron source. ConfProc. 2006;C060626:2484–2486. Available from: http://www.slac.stanford.edu/cgi-wrap/getdoc/slac-pub-12659.pdf.

[49] Bailey I, Clarke J, Scott D, Bailey I, Brown C, et al. Eddy Current Studies From the Undulator-based Positron Source Target Wheel Prototype. ConfProc. 2010;C100523:THPEC033. Available from: http://accelconf.web.cern.ch/accelconf/IPAC10/papers/thpec033.pdf.

[50] Abramov AD. Eddy-current loss in a rotating magnetic field. Soviet Physics Journal. 1971;14(1):25–28. Available from: http://dx.doi.org/10.1007/BF00819855.

[51] Marks N. Conventional Magnets for Accelerators; Accessed: May 21, 2012. Available from: http://www.cockcroft.ac.uk/education/Basic_course_Final.ppt.

[52] Wolfram Research I. Mathematica; 2012.

[53] Bailey I, Barber D, Buttimore N, Chattopadhyay S, Court G, Steffens E. Future Sources of Polarised Positrons. In: Aip Conference Proceedings. vol. 1008; 2008. p. 117.

[54] Clarke J, Bailey I, Baynham E, Bradshaw T, Brummitt A, Bungau A, et al. Construction of a full scale superconducting undulator module for the International Linear Collider Positron Source. In: The eleventh European Particle Accelerator Conference, EPAC. vol. 8; 2008. p. 709–711.

[55] Newton D, et al. Modeling synchrotron radiation from realistic and ideal long undulator systems. Proceedings of IPAC2010, Kyoto, Japan. 2010;.

[56] Newton D, et al. The rapid calculation of synchrotron radiation output from long undulator systems. Proceedings of IPAC2010,Kyoto, Japan (2010);.

[57] Liu W, Gai W, Borland M, Xiao A, Kim KJ, Sheppard J, et al. Emittance Evolution of the Drive Electron beam in a Helical Undulator for the ILC Positron Source;.

[58] Alrashdi A, Bailey I, Newton D. Possible uses of gamma-rays at future intense positron sources. Proceedings of IPAC2014, Dresden, Germany. 2014;.

[59] Zamfir N. Extreme Light Infrastructure–Nuclear Physics (ELI-NP) European Research Centre. In: EPJ Web of Conferences. vol. 66. EDP Sciences; 2014. p. 11043.

[60] Wu Y, Busch M, Emamian M, Faircloth J, Hartman S, Howell C, et al. Performance and Capabilities of Upgraded High Intensity Gamma-ray Source at Duke University. PAC2009. 2009;p. 3181–3183.

[61] Wu Y, et al. Accelerator Physics Research and Light Source Development at Duke University. Proceedings of IPAC2010, Kyoto, Japan. 2010;87.

[62] Liu W, Gai W, Kim KJ. Systematic study of the undulator based ilc positron Source: Production and capture. In: Particle Accelerator Conference, 2007. PAC. IEEE. IEEE; 2007. p. 2918–2920.

[63] Jenkins M. Novel Designs For Undulator Based Positron Source. Lancaster University; 2014.

[64] Venturini M, Dragt AJ. Accurate computation of transfer maps from magnetic field data. Nuclear Instruments and Methods in Physics Research Section A: Accelerators, Spectrometers, Detectors and Associated Equipment. 1999;427(1):387–392.

[65] Tain J. A gamma-ray beam line for nuclear physics and applications at the spanish synchrotron alba. Shielding Aspects of Accelerators, Targets and Irradiation Facilities–SATIF 7;p. 39.

[66] Warren G, Caggiano J. FY08 Annual Report for Nuclear Resonance Fluorescence Imaging. Pacific Northwest National Laboratory, Richland, WA. 2009;PNNL-18147. Available from: http://www.pnl.gov/publications/abstracts.asp?report=252666.

[67] Hammer JW, Fischer B, Hollick H, Trautvetter HP, Kettner KU, Rolfs C, et al. Beam properties of the 4 MV dynamitron accelerator at Stuttgart. Nuclear Instruments and Methods. 1979;161(2):189 – 198. Available from: http://www.sciencedirect.com/science/article/pii/0029554X79903847.

[68] ELI-NP White Book;Available from: http://www.eli-np.ro/documents/ELI-NP-WhiteBook.pdf.

[69] Hajima R, Hayakawa T, Kikuzawa N, Minehara E. Proposal of nondestructive radionuclide assay using a high-flux gamma-ray source and nuclear resonance fluorescence. Journal of Nuclear Science and Technology. 2008;45(5):441–451.

[70] Danon Y, Block R, Testa R, Moore H. Medical isotope production using a 60 MeV linear electron accelerator. TRANSACTIONS-AMERICAN NUCLEAR SOCIETY. 2008;98:894.

[71] Habs D, Kster U. Production of medical radioisotopes with high specific activity inphotonuclear reactions with -beams of high intensity andlarge brilliance. Applied Physics B. 2011;103(2):501–519. Available from: http://dx.doi.org/10.1007/s00340-010-4278-1.

[72] Jenkins M, Bailey I. Novel designs for undulator based positron sources. Proceedings of IPAC2012, New Orleans , USA. 2012;.

[73] Staufenbiel F, Adeyemi O, Kovalenko V, Moortgat-Pick G, Malysheva L, Riemann S, et al. Heat Load and Stress Studies for an Design of the Photon Collimator for the ILC Positron Source. arXiv preprint arXiv:12025987. 2012;.